UNIVERSITY OF STRATHCLYDE

DEPARTMENT OF CIVIL ENGINEERING

Modelling Fault Zone Evolution: The effect of heterogeneity

by

Heather Moir

A thesis presented
in fulfilment of the requirements
for the degree of Doctor of Philosophy

2010

This thesis is the result of the author's original research. It has been composed by the author and has not been previously submitted for examination which has led to the award of a degree.

The copyright of this thesis belongs to the author under the terms of the United Kingdom Copyright Acts as qualified by University of Strathclyde Regulation 3.50. Due acknowledgement must always be made of the use of any material contained in, or derived from, this thesis.

Signed:
Date :

Abstract

One of the major uncertainties in flow simulations models is in predicting the permeability of faults, principally in the detailed structure of fault zones. The research presented in this thesis expands our understanding of the temporal and spatial evolution of fault zones and the different geometries which can evolve.

This research, through the development and application of a finite element model MOPEDZ (Modelling Of Permeability Evolution in the Damage Zone), investigates the temporal and spatial evolution of fault zones from pre-existing structures. Initially the major influences on the geometry of the predicted fault zones formed from the linkage of many pre-existing structures within a single homogeneous rock type was explored. This was followed by investigations into how the predicted geometry was affected by introducing host-rock heterogeneity. Results from the simulations are validated using outcrop data.

The research presents a significant step forward in scientific understanding and validation of current conceptual theories of fault zone development.

Dedication

To James

Acknowledgements

I would like to thank my supervisor Becky Lunn for all encouragement and stimulating conversations we have had over endless cups of coffee. I don’t know where you get your patience from, it was a pleasure working with you.

Thanks also to Zoe Shipton who has provided invaluable advice, ideas and networking skills.

Zoe and Becky formed and head a very dynamic multidisciplinary research group, Faults and Fluid Flow (FAFF), which have regular meetings and field trips. I want to thank all the members of FAFF, past and present, I have always found our meetings stimulating and appreciate all the constructive criticism and ideas that was generated.

I want to thank Prof Nigel Mottram for his help with Matlab and COMSOL at the start of this research.

I want to thank the Civil Engineering department for funding my scholarship.

Finally I owe a huge thank you to my husband, James, for all of his love, support and patience, I could never have undertaken this challenge without you.

Contents

Figure List

1 Introduction

Flow simulation models are of major interest to many industries including hydrocarbon, nuclear waste, sequestering of carbon dioxide, mining and in the exploitation of hydrothermal fluids and steam [*Brogli*, 2008]. One of the major uncertainties in these models is in predicting the permeability of faults, principally in the detailed structure of the fault zone.

Studying the detailed structure of a fault zone is difficult because of the inaccessible nature of sub-surface faults and also because of their highly complex nature; fault zones show a high degree of spatial and temporal heterogeneity [*Aydin*, 2000; *Caine et al.*, 1996], i.e. the properties of the fault change as you move along the fault and they also change with time.

It is well understood that faults influence fluid flow characteristics [*Bergbauer and Martel*, 1999], they may act as a conduit or a barrier or even as both, by blocking flow across the fault while promoting flow along it [*Aydin*, 2000; *Uehara and Shimamoto*, 2004]. Within brittle rocks, such as granite, fracture networks are limited but provide the dominant pathway for flow within this rock type [*Aydin*, 2000]. Research at the EU's Soultz-sous-Forệt Hot Dry Rock test site [*Evans et al.*, 2005] shows that 95% of flow at the test site occurs within a single fault zone, at 3490m. Though other factors such as cementation and stress rate affect flow [*Aydin*, 2000], understanding the detailed structure of a fault zone is essential as certain structures within a zone will encourage flow while others can block it.

Current methods of examining faults include seismic surveys which do not give detailed internal structure, often miss small faults and give no information on permeability. Boreholes can provide three types of data relating to fault permeability; borehole cores, borehole logging, and pumping tests. A cored borehole can provide information on rock type, mineral content, fracture density and orientation and the sample can be tested for permeability. However, boreholes are expensive to drill, and even more expensive to core, so only a small quantity of such data are available. Furthermore, most borehole data are usually generated by the hydrocarbon industry who deliberately avoid drilling through faults: drilling through a fault can be hazardous due to the possibility of it acting as a barrier to flow and hence holding a high pressure gradient across it. Even if a borehole does pass through a fault, this can only be used to characterise the permeability of the fault at one location, i.e. a 1D transect through a 3D structure. Estimates of the permeability of a fault as a whole can theoretically be obtained from data produced by pumping tests and hydrocarbon extraction; however monitoring wells for interpretation of pump test data are rarely available. One solution to this lack of fault permeability data is to generate a model which can predict the likely permeability and location of fluid flow within the whole fault zone.

The first step in producing one such model was carried out by *Willson, et al.*, [2007]. These authors produced a computer code MOPEDZ (Modelling Of Permeability Evolution in the Damage Zone surrounding faults) which successfully simulated simple linkage of small scale fractures in a homogeneous rock. The code utilises finite element modelling for the numerical simulation of rock fractures and will be described in detail within Chapter 3.

The aim of the research presented in this thesis is to increase our understanding of fault zone development by expanding MOPEDZ and testing the results of modelling experiments against mapped exposures. In particular:-

1) What are the major influences on the geometry of fault zones formed from the linkage of many pre-existing structures?
2) How is this geometry affected by host-rock heterogeneity?

The path of the research undertaken is illustrated in Figure 1.1, and consisted of 3 phases. Phase 1 required an expansion of my knowledge and skills base in this highly interdisciplinary research. Phase 2 involved expanding and developing the code to simulate larger, more complex scenarios. The final phase involved investigating the effect of heterogeneity on the simulations.

Within this thesis Chapter 2 describes the geology of fault zones summarising the literature relating to fault zone structure, evolution and permeability. Chapter 3 describes the modelling technique used and details the early development of MOPEDZ and describes how this code was expanded during my research. Chapter 4 illustrates the expanded MOPEDZ code and gives results of the evolution of simple fault zones from a large network of pre-existing joints. Chapter 5 investigates the effect of increasing the heterogeneity of the host rock. This was conducted on a small scale by simulating faulting in ignimbrite and on a large scale by simulating fault evolution and linkage across different lithologies. Chapter 6 summarises the findings of this research and Chapter 7 discusses possible future work which may be undertaken.

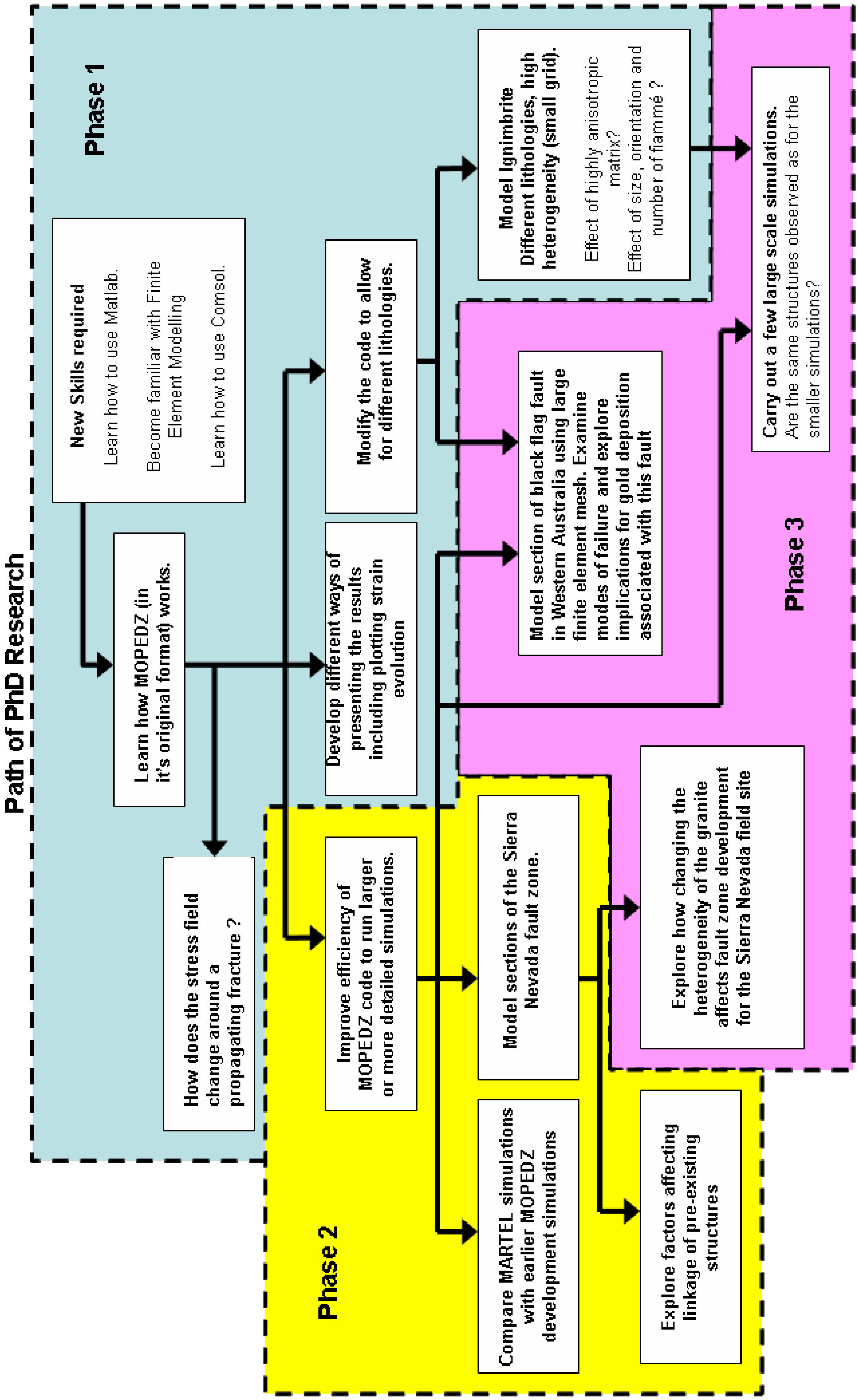

Figure 1.1 - Outlining the path of the research carried out during my PhD.

2 Geological Faults and Fault Zones

In this chapter of the thesis I will describe what faults and fault zones are, I will review different conceptual models of fault evolution which have been presented in the literature. I will also consider the different factors that may affect that evolution. As indicated in the introduction it is the intention that ultimately this research will be incorporated into flow simulation models, hence, this chapter will also discuss current theories relating faults and fluid flow.

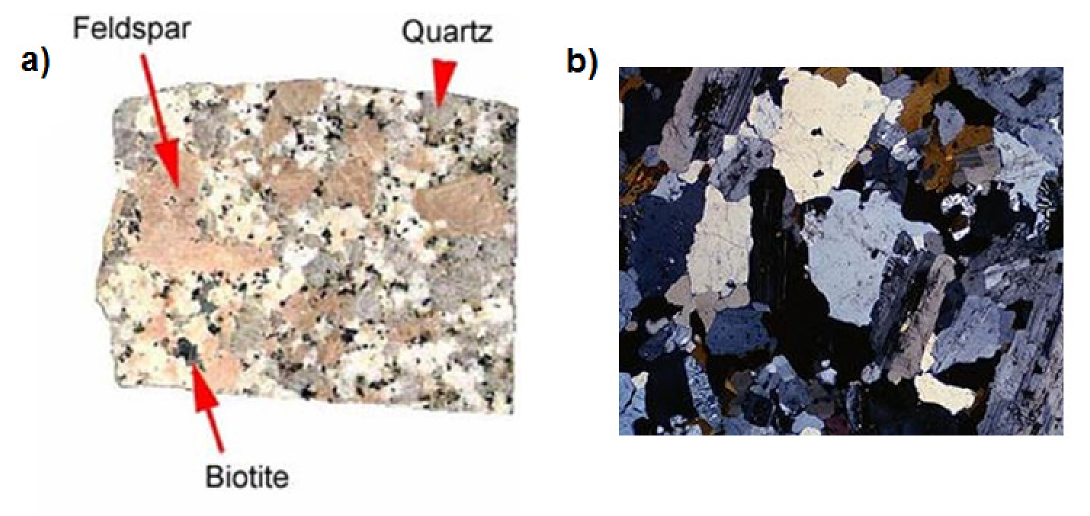

Figure 2.1 - Example of granite, a crystalline rock: a) A hand sample with typical minerals identified. b) A thin section of granite viewed under the microscope illustrating the interlocking crystals.

Within this thesis the term ‘brittle rock’ refers to any rock which fails in a brittle (as apposed to ductile) fashion. This not only includes crystalline igneous rocks such as granite (Figure 2.1) which are comprised of interlocking crystals with a random orientation or crystalline metamorphic rocks which are comprised of interlocking crystals with a preferred orientation but also includes sedimentary rocks such as sandstone (Figure 2.2) and limestone.

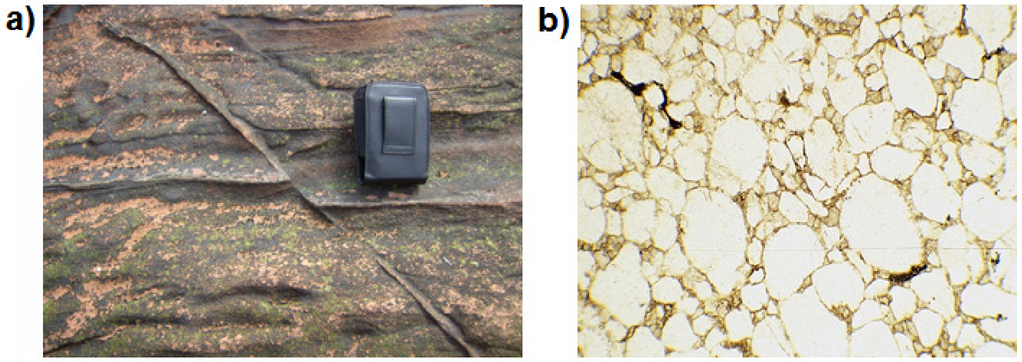

Figure 2.2 - An example of sandstone, a sedimentary rock: a) Small fault in sandstone on Arran. b) Thin section of sandstone illustrating that sandstone is comprised of individual grains held together by cement rather than the interlocking crystals observed in igneous or metamorphic rocks.

Faulting in brittle rocks has been explored by different researchers by examining and mapping field exposures, by laboratory testing and by microscopic examination of failed samples. Different brittle materials which have been explored include:-

- Granite [*Pollard and Segall*, 1987; *Martel*, 1990; *Lockner et al.,* 1991; *Haimson and Chang*, 2000; *Pachell and Evans*, 2002; *Pachell et al.*, 2003; *Hamiel et al.,* 2006; *Heap and Faulkner*, 2008]
- Carbonates [*Willemse et al.*, 1997; *Billi et al.*, 2003; *Al-Shayea*, 2005; *Micarelli et al.*, 2006; *Ganne et al.* 2007]
- Sandstone [*Shipton and Cowie*, 2003; *Joussineau and Aydin,* 2007]
- Marble [*Li et al.,* 2005; *Yang et al.*, 2008]

- Gypsum [*Bobet*, 2000]
- Gabbro [*Xu et al.*, 2005]
- Ice [*Nixon*, 1996; *Kattenhorn and Marshall*, 2006]

2.1 What are Faults ?

Faults are fractures in the Earth's crust which have an appreciable displacement, parallel to the fracture surface, of one side of the fault relative to the other. Fractures without an appreciable relative displacement are termed joints.

Faults vary in size from a few millimetres [*Lockner et al.*,1991; *Granne et al.*, 2007] to several kilometres [*Pachell and Evans*, 2002; *Pachell et al.,* 2003]. They are common throughout the Earth's crust though most are not exposed at the surface. As mentioned in the introduction current methods of investigating these 'hidden' faults, seismic profiles and borehole data, are limited in their usefulness.

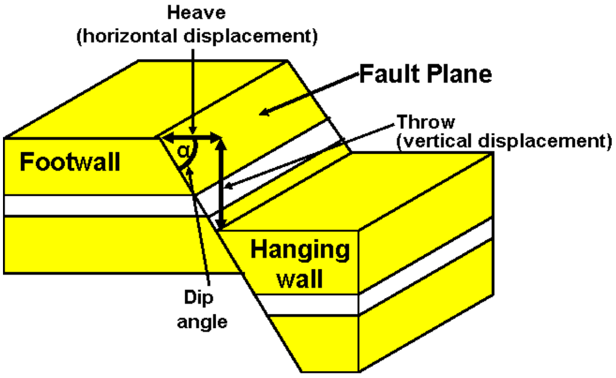

Figure 2.3 – Idealised normal fault where the hanging wall has moved down relative to the footwall accommodating extension in the crust.

An idealised fault and the terms associated with it are shown in Figure 2.3, this is an example of a normal fault. There are 4 types of fault (Figure 2.4) which are classified according to their relative movement:-

- a fault with vertical movement where hanging wall moves down relative to the footwall is a normal fault (Figures 2.3 and 2.4a)

- a fault with vertical movement where hanging wall moves up relative to the foot wall is a reverse fault (Figure 2.4b) (if a reverse fault is at a very low angle it is usually termed a thrust fault)

- a fault with significant vertical and horizontal movement is an oblique fault (Figure 2.4c)

- a fault with horizontal movement is a strike-slip fault
    - if the movement of one side of the fault relative to the other is to the left it is a sinistral strike-slip (Figure 2.4d)
    - if the movement of one side of the fault relative to the other is to the right it is a dextral strike-slip (Figure 2.4e).

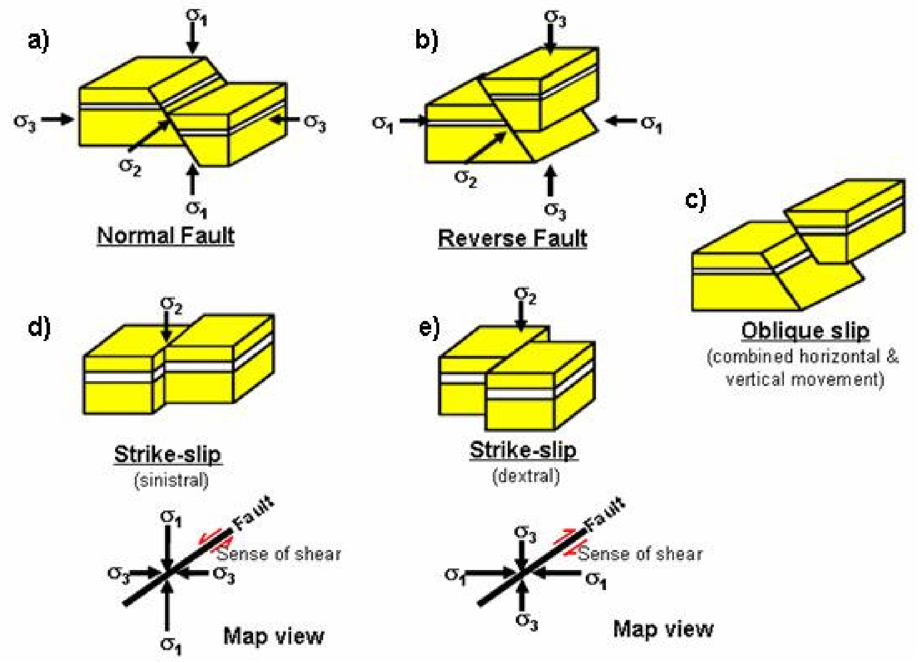

Figure 2.4 – **Schematic showing common types of fault and the orientation of the principal stresses associated with each.**

Faulting is a brittle mechanism for achieving shear displacement due to changing stress conditions in the Earth's crust. On a large regional scale, stress changes are usually due to plate tectonics but can also be influenced by other processes such as; rebound or subsidence of the crust due to glacial activity, intrusion of large igneous bodies or caldera collapse.

Stress is the force exerted on a plane divided by the area of that plane and can be either compressive or tensile. Within geological research compressive stress is considered to be positive, this is the opposite to the convention taken by engineers who consider tensional stress to be positive. As this research is dominated by geological considerations compressive stress will always be taken as positive. The calculation of stress will be examined in more detail in Chapter 3 where the development of the MOPEDZ code will be described. At this stage it is sufficient to point out that the type of fault which will occur (normal, reverse, strike-slip or oblique) is determined by the stress field acting on the fault. The stress field can be resolved into three mutually orthogonal principal stresses σ_1, σ_2 and σ_3, where σ_1 is the greatest principal compressive stress, and σ_3 is the smallest principal compressive stress. These principal axes for normal, reverse and strike slip faults are indicated in Figure 2.4.

Though faults are often idealised to simple planar features (as shown above) close observations show that most contain segments and often have an irregular fracture trace [*Martel* 1990; *Renshaw and Pollard*, 1994; *Martel,* 1999; *Pachell and Evans*, 2002]. Probably the most famous irregularity is the "big bend" in the San Andreas Fault, Figure 2.5. These irregularities occur at all scales from kilometres [*Pachell and Evans*, 2002] to millimeters [*Li et al.,* 2003].

Figure 2.5 – Section of the San Andreas Fault (after http://www.cliffshade.com/colorado/images/san_andreas_map)

As well as exhibiting irregularities faults differ from the idealised single discrete planar feature in that they frequently occur as a network of parallel and sub parallel interconnecting closely spaced fault surfaces, the structure and composition of which differ from the unaltered surrounding host rock. These networks are termed fault zones.

2.2 Architecture of a Fault Zone

Fault zones are composed of 3 distinct components: a fault core, a damage zone and host rock (protolith) [*Chester et al.,* 1993; *Caine et al.*, 1996], Figure 2.6. By definition any damage or structures present in the protolith are due to regional tectonic processes and are not due to the activity of the fault.

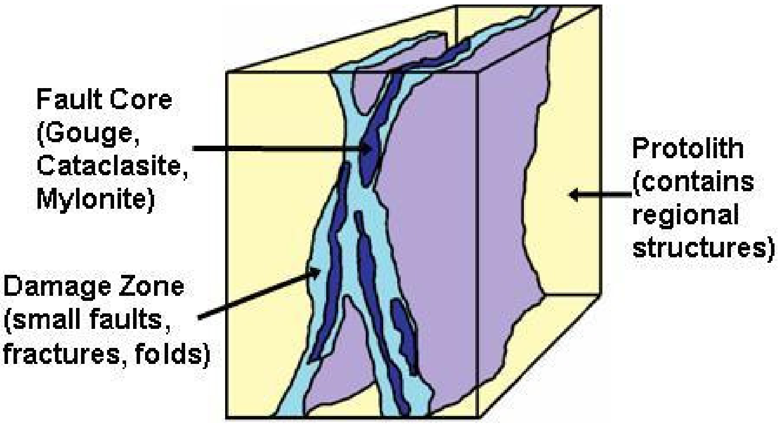

Figure 2.6 – Fault zone architecture, from *Caine et al.*, [1996].

2.2.1 Damage Zone

The damage zone is the area surrounding a fault that contains features that have been caused by the fault. There may also be features in the damage zone which are similar to those in the protolith and are related to regional tectonic processes. A common property of damage zones, which allows them to be distinguished from the protolith, is the increase in fracture density as the fault core is approached [*Chester et al.*, 1993; *Gudmundsson*, 2004] , Figure 2.7. Experimental results have shown a change in material properties of the rock within the damage zone as the fault core is approached [*Faulkner et al.* 2006].

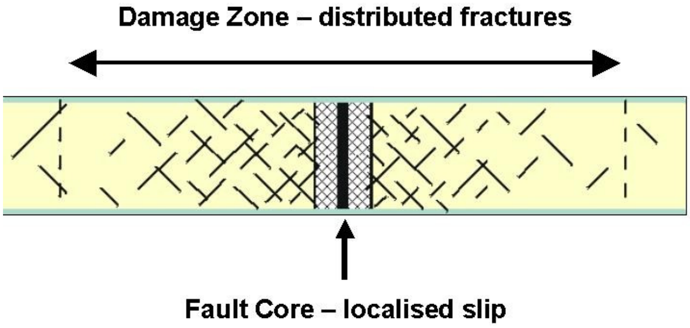

Figure 2.7 – A conceptual model of a fault zone, after *Chester et al.* [1993], fracture density increases towards the fault core.

Many different features can be associated with fault damage zones including; fractures, deformation bands (particularly in sandstones), and smaller faults [*Caine et al.,* 1996]. If fluid flow has occurred within the damage zones some or all of the fractures and small faults within the damage zone may become sealed with mineral precipitates forming veins.

The small faults or fractures in the damage zone may occur in a similar orientation and have the same sense of slip as the main fault (synthetic) or they may develop roughly perpendicular and have the opposite sense of slip to the main fault (antithetic). Antithetic faults or fractures often evolve from the synthetic features, Figure 2.8. The fractures which develop only evolve into faults if there is movement of one side of the feature relative to the other.

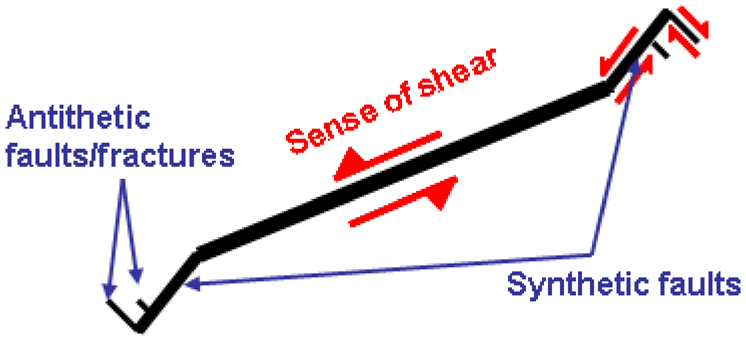

Figure 2.8 - Illustration of synthetic and antithetic features which develop within a damage zone.

The damage zone, due to the fracturing within it, may be more permeable than either the surrounding host rock or the fault core [*Caine et al.,* 1996; *Aydin,* 2000]. The width of the damage zone is not constant. *Kim et al*., [2004] divide the damage zone into three parts, fault tip, wall and linkage. *Joussineau and Aydin* [2007] also show that the damage zone is widest around the centre of a fault segment and at the tips, where as *Segall and Pollard* [1983] suggest that it is widest at the linkage structure between two different segments of the fault, Figure 2.9.

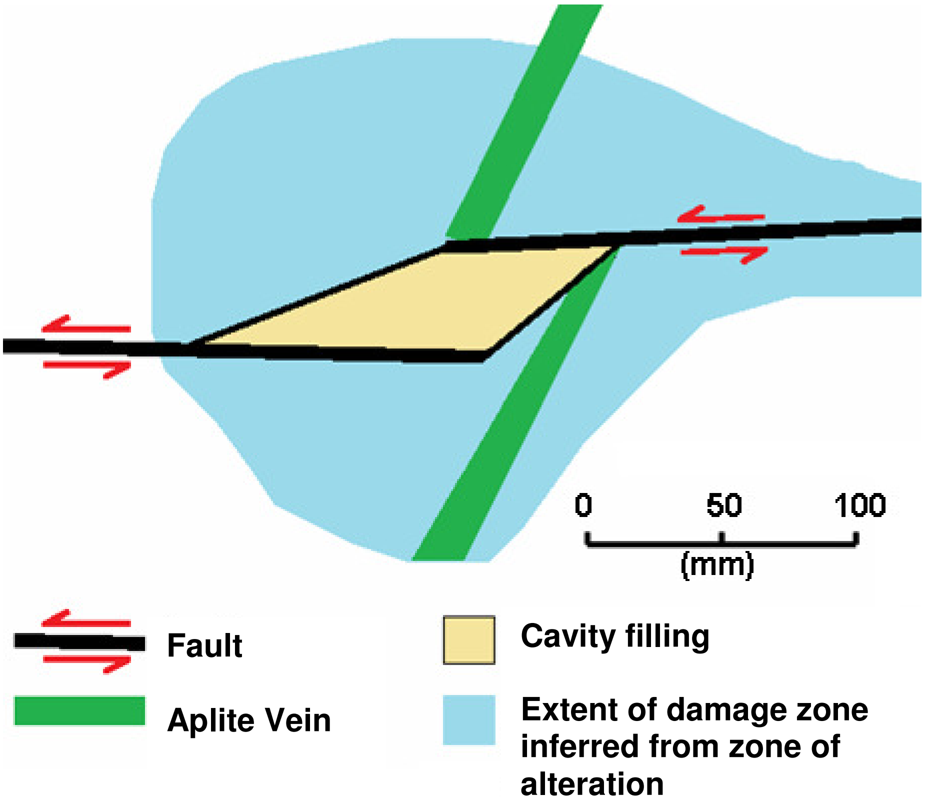

Figure 2.9 – Damage zone widest around linkage structure. After *Segall and Pollard,* [1983] their Figure 8.

2.2.2 Fault Core

The fault core is where the majority of the displacement on a fault occurs [*Caine et al.* 1996]. Fault cores vary in complexity from single slip surfaces to highly heterogeneous structures with multiple slip surfaces and many different fault rocks.

A slip surface is a roughly planar structure where the two sides of the fault have slid past each other. Slip surfaces are often characterized by polished surfaces called slickensides, Figure 2.10, sometimes showing striations that are known as slickenlines. The rocks on a slip surface have been crushed and compacted and as result may have low porosity.

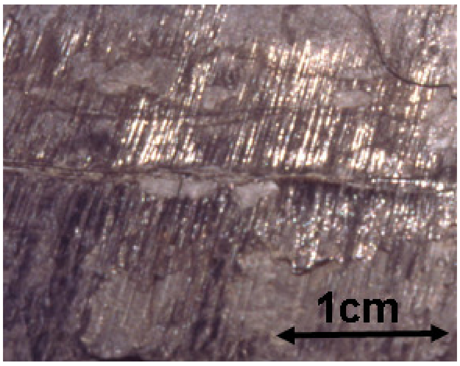

Figure 2.10 - Example of small scale slickensides (It should be noted that this feature can occur at many scales).

A large fault may have a highly complex and heterogeneous fault core, Figure 2.11, which may consist of many slip surfaces and different rock types. The different rock types which can be associated with a fault core include: cataclasite, mylonite and pseudotachylyte. Cataclasites are any material which as been mechanically broken down by the movement of the fault and range from breccia (large angular fragments) to gouge (fine grained). Unlike slip surfaces which are typically roughly planar features, cataclasites usually outcrop as three dimensional lenses or bands, Figure 2.11. Mylonites are hard, coherent rocks which have experienced a reduction in grain size through mechanical deformation, they often exhibit low porosity. Pseudotachylite is a fault rock that has the appearance of the basaltic glass, tachylite. It is generally found either along fault surfaces, often as the matrix to a breccia, or as veins injected into the walls of the fault. They are thought to be formed by frictional melting of the wall rocks during rapid fault movement associated with a seismic event and are often cited as fossil evidence of earthquakes.

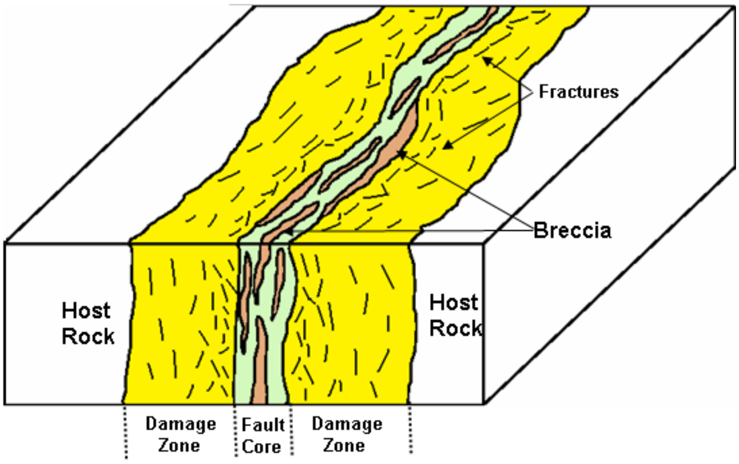

Figure 2.11 – Sketch of fault zone illustrating highly heterogeneous fault core, after *Gudmundsson* [2004]

The fault zone architecture described above has been observed in different rock types. *Billi et al.*, [2003] examined the structure of the fault zone in carbonates showing the marked difference in permeability between the core and damage zone. Fault cores in limestone may develop ultracataclastic zones [*Chambon et al.*, 2006]. *Micarelli et al* ., [2006] examined the hydraulic properties of a fault in limestone and showed that the core was acting as a seal, however analysis of meteoric water on either side of the fault shows that there is some flow across the fault, this appears to be occurring at the step over structure where two segments of the fault are linked.

2.3 Fault Zone Evolution

Several authors have developed conceptual models of how faults develop in brittle rocks. Two models dominate. The first model suggests that faults grow by linking pre-existing structures [*Segall and Pollard*, 1983; *Martel*, 1990; *Bergbauer and Martel*, 1999; *Pachell et al.*, 2003]. The second model suggests that shear fractures propagate by the development of a process zone; microfractures form near the fault tip and then coalesce into a through going fault [*Lockner et al.,*1991; *Reches & Lockner* 1994; *Moore and Lockner, 1995; Vermilye and Scholz,* 1998].

2.3.1 Fault evolution by linking pre-existing structures.

Faults are often observed to nucleate from pre-existing structures [*Crider and Peacock,* 2004]. A pre-existing structure is any structure which formed under an earlier stress regime and is not caused by the later fault evolution. The pre-existing structures from which faults nucleate are commonly joints [*Segall and Pollard*, 1983; *Martel,* 1990; *Bergbauer and Martel*, 1999; *Pachell et al.,* 2003] in which subsequent mineralisation may have occurred. In granite, faults have been mapped which nucleate from pre-existing dykes [*d'Alessio and Martel*, 2004]. As dykes may be several kilometres in length they could provide the nucleation mechanism for very long faults. Other pre-existing features from which faults appear to have nucleated include :-

- Other small faults [*Kim et al.,* 2004].
- Solution seams (typically associated with limestone) [*Willemse et al.*, 1997], Figure 2.12a.
- Deformation bands [*Davatzes et al.,* 2003], Figure 2.12b.

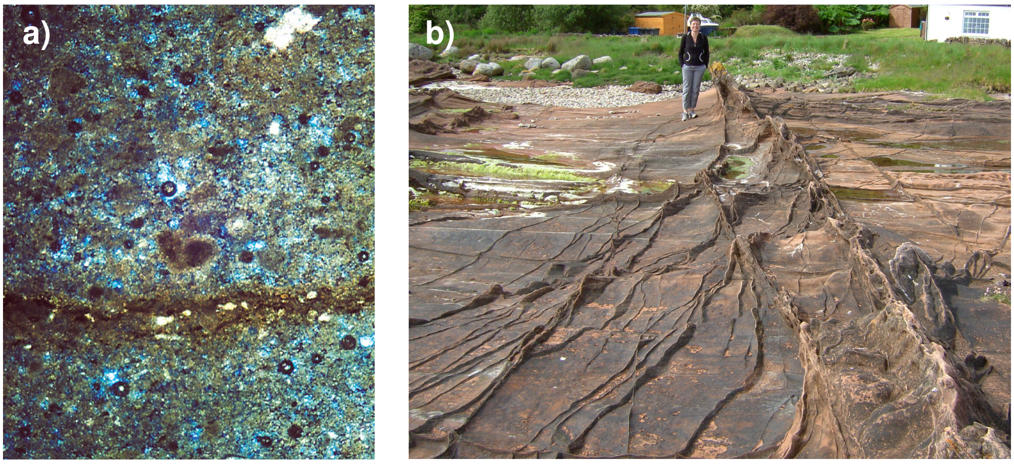

Figure 2.12 – **Examples of possible pre-existing structures a) solution seam in carbonate rock [*Brister and Ulmer-Scholle*, 2004]. b) Deformation bands on Arran, Scotland (photo taken by author).**

When pre-existing features experience compressive loading, stress concentrations (both in tension and compression) develop around the tip of the feature (Figure 2.13). Shearing of these features often results in the formation of secondary fractures at (or near) the tip of the feature, (Figure 2.14). These secondary fractures have been given several different names including; tail cracks/fractures [*Willemse et al.*, 1997; *Cruikshank and Aydin*, 1994], splay fractures [*Pachell and Evans*,

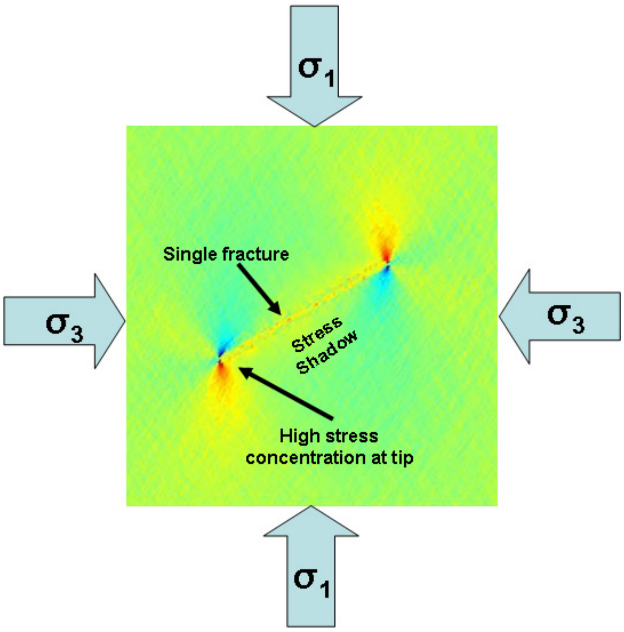

Figure 2.13 – Illustration of the stress concentration at the tips of a fault/fracture. (Red is in compression, blue is in tension)

2002; *Myers and Aydin* , 2004], horsetail fractures [*Granier*, 1985] and wing cracks [*Crider and Peacock*, 2003]. Some authors [*Granier*, 1985; *Crider and Peacock*, 2003] have made a distinction between wing cracks and tail (or horsetail) cracks suggesting that wing cracks are typically 'wing shaped' and at a high angle to the original feature, where as tail cracks are typically curved and at a low angle to the original feature. In this thesis all fractures associated with faulting at (or near) the tip of pre-existing feature will be termed wing cracks.

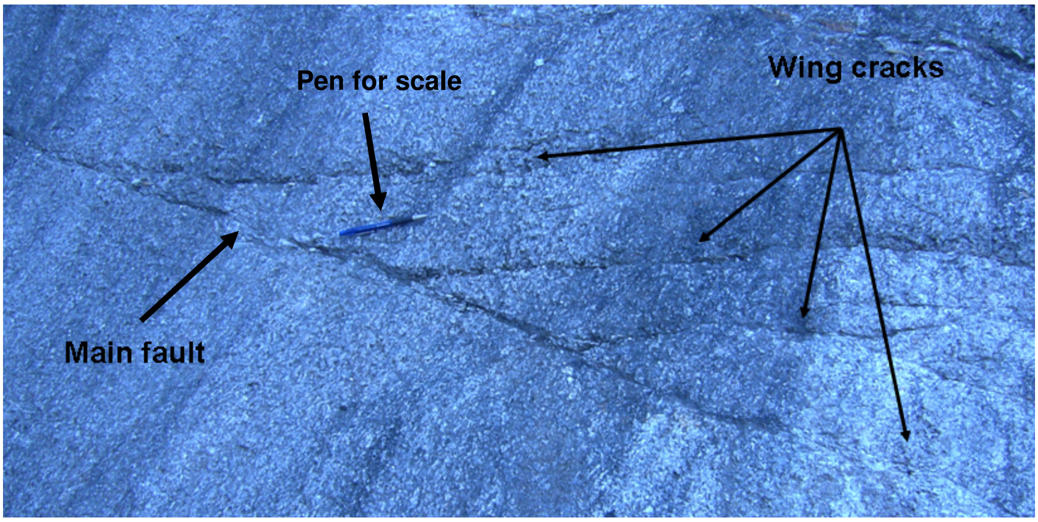

Figure 2.14 - An example of wing cracks in a granite exposure in the Southern uplands, Scotland. An alternative name for the features illustrated could be tail cracks, splay fractures or horsetail cracks (photo taken by author).

In the field the secondary fractures which develop at the tip (or near the tip) of a pre-existing feature have been observed to exhibit many different structures (Figure 2.15).

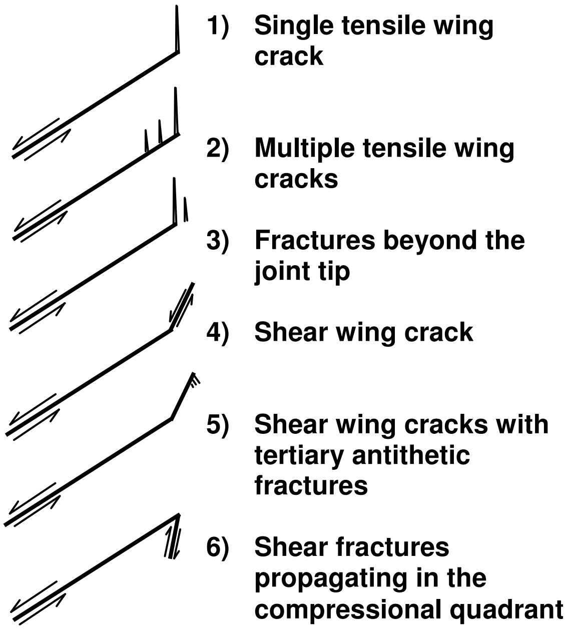

Figure 2.15 – Geological features associated with a single fault.

These features are seen in many different rock types, wing cracks have even been observed in the ice shell of the Jupiter moon Europa [*Kattenhorn and Marshall*, 2006]. Wing cracks observed in the field vary in length from a few centimetres to several meters [*Segall and Pollard*, 1983].

Many of these features have been reproduced in laboratory testing of different rock types [*Lockner et al.,*1991; *Al-Shayea*, 2005; *Granne et al.,* 2007]. *Yang et al.* [2008] produced experimental results in marble which included both tensile and shear failure, Figure 2.16, similar results were obtained by *Misra et al.,* [2009] using a polymethylmethaacrlate which was shown to behave in a brittle fashion. It has been suggested that where wing cracks do not evolve under laboratory conditions it may be due to the fact that the artificially created 'pre-existing' structures are too smooth, unlike naturally occurring ones which typically have a degree of roughness [*Golshani et al.,* 2006].

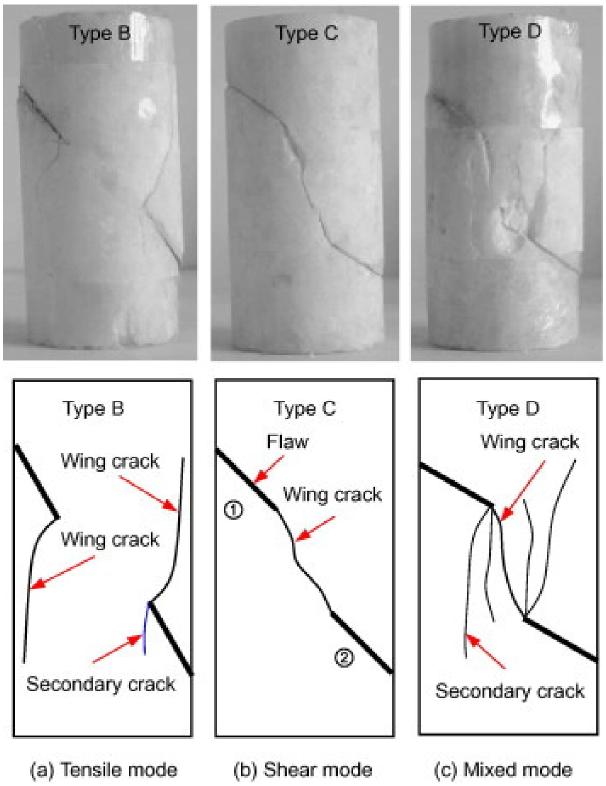

Figure 2.16 – Experimental results of laboratory testing of Marble, from Figure 18 of *Yang et al.,* [2008]. Different failure modes produced dependant on the initial geometry of the pre-existing flaws.

During laboratory testing failure is typically monitored by acoustic emission. For an intact specimen (with no pre-existing fractures) the pattern of the acoustic emissions of the microscopic failure is random then they begin to coalesce onto what will become the macroscopic failure [*Lockner et al.,* 1991; *Amitrano,* 2006]. *Granne et al.*, [2007] show that in experiments on limestone when the load is less than 25% of that required for failure the pattern is random, at 60% the acoustic emissions start to group along micro-cracks and by 88% the micro-cracks begin to interact.

The research carried out in laboratories around the world, in conjunction with field observations, has allowed some understanding of the mechanical properties of brittle rock to be established. In particular they have enabled prediction of the orientation of linkage fractures and their mode of failure, for a single fracture or pair of fractures in an ideal homogeneous medium. It is possible to identify which factors may be significant in determining which type of failure is likely to occur, these include:-

- Heterogeneity of host rock [*Tang,* 1997; *Martel*, 1999; *Tang et al.,* 2007]. *Tang* [1997] carried out lab tests on samples taken from a core of an apparently homogeneous rock and showed that its material properties varied throughout the core.
- Strength of host rock [*Martel,* 1999].
- Friction of the fault surface [*Martel*, 1999].
- Fracture roughness [*Renshaw and Pollard*, 1994].
- Angle of pre-existing discontinuity to maximum compressive stress [*Renshaw and Pollard*, 1994; *Lunn et al.,* 2008; *Yang et al.,* 2008; Blenkinsop, 2008].

- Ratio of σ_1 to σ_3 [*Renshaw and Pollard*, 1994; *Lunn et al.,* 2008*;* *Blenkinsop,* 2008].
- Location of neighbouring features [*Martel,* 1999; *Yang et al.,* 2008]. As shown in Figure 2.13 a pre-existing feature which is experiencing a load will alter the stress field around that feature. Where more than one feature is present the altered stress fields interact. This is discussed later and is illustrated in Figures 2.19 and 2.20. The wing cracks that develop may link adjacent pre-existing structures, this is one of the ways in which faults may evolve.

2.3.1.1 Martel's conceptual model for fault zone evolution.

The conceptual model for the growth of strike slip faults in granite, through the linkage of pre-existing joints detailed by *Martel* [1990] has four stages. At each stage greater displacement is accommodated. The first stage of Martel's conceptual model (Figure 2.17a) depicts the formation of parallel joints which form parallel to the direction of the maximum compressive stress. The joints are not randomly distributed, because each joint lowers the stress in the vicinity of its location [*Pollard and Segall,* 1987] which inhibits further joints forming. The observation that these joints are often parallel to the region stress field at the time the granite cooled is widely accepted [*Pachell et al.*, 2003] and is described in some detail by *Bergbauer and Martel* [1999].

In the second stage of Martel’s conceptual model (Figure 2.17b) it is assumed that the regional stress has rotated, such that the direction of the maximum horizontal compressive stress now makes an angle of around 20º with the strike of the joints. This causes left lateral slip on the joints (Figure 2.18) It is widely accepted that the displacement on a fault is greatest in the centre of the fault (or fault segment) [C*owie and Scholz*, 1992; *Joussineau and Aydin*, 2007]. Wing cracks (termed splay fractures by Martel) form off the tips of the faults and propagate at angles between 36º and 48º relative to the original joint direction. In some cases the faults develop single wing cracks, and in others multiple wing cracks. In cases where the original joints step left, the wing cracks may link the faults. It should also be noted that not all of the joints form wing cracks.

In the third stage (Figure 2.17c) pairs of simple left lateral faults interact, and form simple fault zones. Simple fault zones are characterized by prominent fractures that strike at an oblique angle to pairs of boundary faults. Infill fractures develop within the simple fault zones.

Finally, in the fourth stage of Martel’s conceptual model, Figure 2.17d, the simple fault zones interact and fracturing occurs between the simple fault zones. This is a similar process to stage three but occurring at a scale one magnitude larger linking the simple fault zones together into larger structures termed compound fault zones.

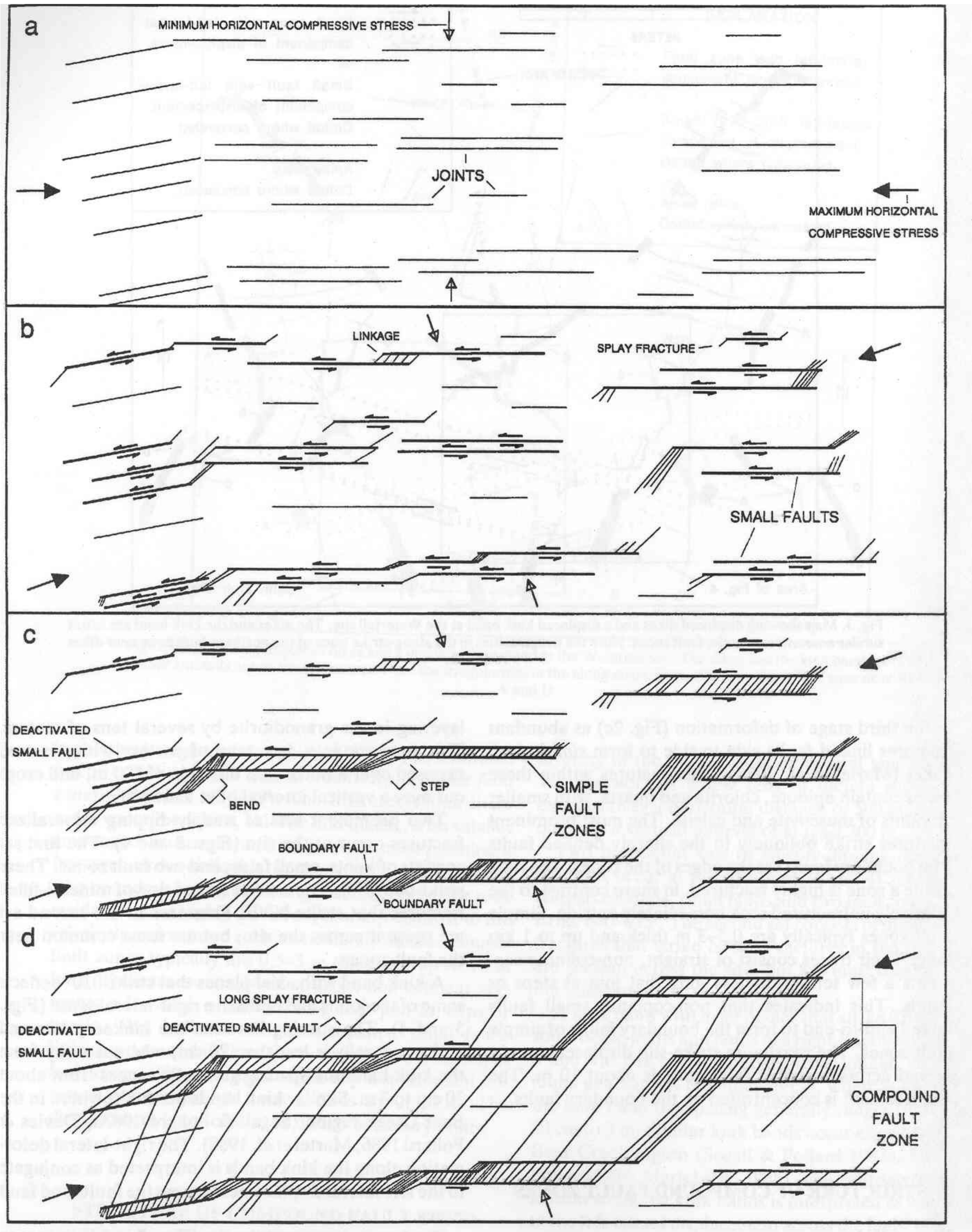

Figure 2.17 - Conceptual model of fault evolution based on field evidence in the Bear Creak area of the Mount Abbot quadrangle [*Martel,* 1990].

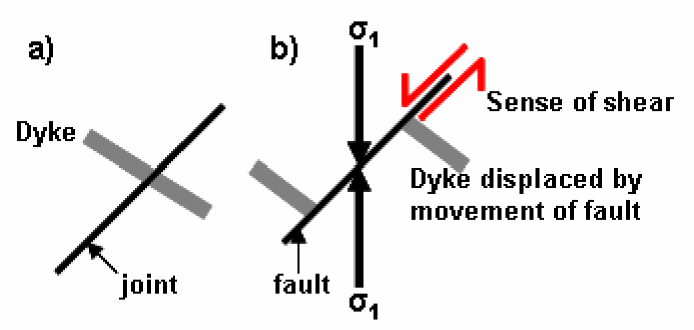

Figure 2.18 – A joint evolving into a fault. There is no displacement of the dyke illustrated in a) but once a load is applied (σ_1) slip is created on the joint causing displacement of one side of the fault with respect to the other (b) . Once slip has occurred this feature is no longer a joint, it has become a fault.

Though the conceptual model detailed above was developed for fault zone evolution in granite other researchers have proposed similar models for other lithologies [*Kim et al.,* 2004; *Myers and Aydin*, 2004; *Flodin and Aydin,* 2004]. *Myers and Aydin* [2004] and *Flodin and Aydin* [2004] examined Jurassic sandstone in Nevada, USA and from their observations of the damage zone surrounding faults within the sandstone they developed a model for fault zone evolution. Their model suggests that faults evolve through the development of deformation bands and splay fractures and that the geometries of the splay fractures is governed by the orientation of the pre-existing joints to the maximum principal compressive stress at the time of faulting. Where the sense of shear and the step sense are opposite (right stepping/left lateral or left stepping/right lateral) the splay fractures develop out from the fault zone, increasing the width of the fault zone, Figure 2.19.

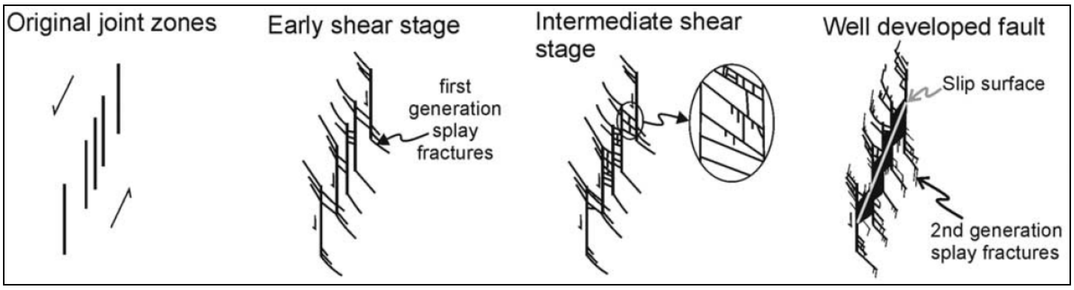

Figure 2.19 - **Fault development in a contractional geometry redrawn from Figure 15 of [*Myers and Aydin,* 2004] (this is an example of right stepping/left lateral relationship).**

Where the sense of shear and the step sense are the same (left stepping/left lateral or right stepping/right lateral) the splay fractures develop towards adjacent joints resulting in increased deformation/damage between the joints, Figure 2.20. The same structures are observed for large and small faults but are generally more complex for larger faults [*Myers and Aydin*, 2004].

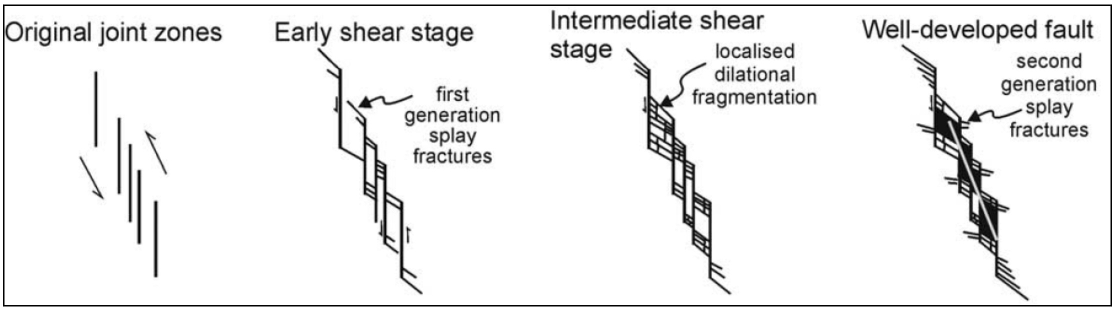

Figure 2.20 - **Fault development in a dilational geometry redrawn from Figure 15 of [*Myers and Aydin,* 2004] (this is an example of left stepping/left lateral relationship).**

These conceptual models are supported by field observations of wing crack evolution from single joints or faults [*Joussineau et al.,* 2007] and by observations of linking fracture networks that have developed between pairs of isolated faults [*Peacock and Sanderson*, 1995; *Kim et al.*, 2004].

Though faults have been shown to nucleate from pre-existing structures, these structures may also result in fault termination. If a fault propagates towards an area with many features which allow slip the numerous small features can dissipate the local stress and inhibit fault growth, [*d'Alessio and Martel*, 2004]. Such fault terminations have been shown to develop at significant depths [*Kirkpatrick et al.*, 2008].

2.3.2 Fault zone evolution through the development of a process zone

An alternative theory to linkage through the development of wing cracks (which is not examined in this thesis) is that shear fractures extend in length by the development of a process zone. Here microfractures form near the tip of the fault where the stress concentrations are highest, these then coalesce into a through-going fault [*Lockner et al.,*1991; *Reches & Lockner* 1994; *Moore and Lockner, 1995; Vermilye and Scholz,* 1998], Figure 2.21.

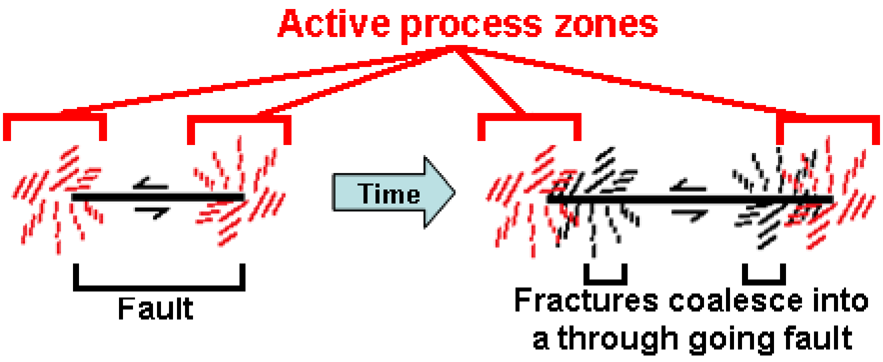

Figure 2.21 - Schematic of the evolution of a fault through the development of a process zone after *Vermilye and Scholz* [1998].

Vermilye and Scholz [1998] concluded that small faults grow by repeated ruptures in the plane of the fault and that each extension is smaller than the length of the fault. The microfractures which are left behind as the tip propagates become inactive and constitute the damage zone around the fault. The extent of the active process zone and hence the width of the damage zone is related to the stress concentration around the tip of the fault [*Cowie* and *Scholz*, 1992]. This implies that microfracture density should decrease with distance from the fault plane and their orientation should vary depending on whether they formed in the tensile or compressive region.

Of fault damage associated with the Atacama fault system, northern Chile was examined by *Mitchell* and *Faulkner* [2009], they compared the mapped damage patterns with those predicted by different conceptual models of damage zone evolution. They conclude that though the fracture pattern was consistent with that predicted by the migrating process zone model but it was also consistent with other models and that distinguishing between them was not possible based only on field observations.

2.4 Fault zones and fluid flow.

Fractures in crystalline rocks provide the dominant fluid pathways at depth [*Caine et al.*, 1996]. Research at the EU's Soultz-sous-Forệt Hot Dry Rock test site supports this contention [*Evans et al.*, 2005]; 95% of flow at the test site occurs within ten open fractures; these fractures are associated with a single fault zone at a depth of 3490m. For a few fractures to provide the main focus for regional flow, they must be uniquely linked to a through-going network. Hydraulic observations taken by *Douglas et al.* [2000] over a 50 year period from a Canadian Shield mine also show flow to be principally governed by fractures associated with a few regional faults. Furthermore, additional geochemical data suggest these faults are isolated from one another. This implies that the fractures within these fault zones are connected along strike, but are largely isolated from the surrounding fractured host rock. The geometry of fault zone associated fracture networks (including orientation, connectivity and aperture) will be governed, in part, by the continuously evolving stress field during fault zone evolution.

For a few faults to dominate regional fluid flow in the manner of *Evans et al.* [2005] and *Douglas et al.* [2000] the fault zone must comprise both a regionally connected network (in comparison to the surrounding fractured host rock) and contain high permeability fractures. Hence, investigating how such fracture networks develop within fault zones will help to understand and predict the hydrology of fault zones.

2.5 Summary

Faults and fault zones are highly complex and in brittle rocks they can have a major influence on fluid flow particularly within the damage zone of a fault.

One conceptual model as to how these fault zones evolve is through the linkage of pre-existing features. It is this process which is simulated by the MOPEDZ code described in Chapter 3.

3 Numerical Modelling of Fault Zone Evolution

This chapter describes the early development of the MOPEDZ code and the theories upon which it was based. It will start, in section 1, with a brief description of the theory behind the mechanical modelling and lead up, in section 2, to a summary of the early development of MOPEDZ carried out by *Willson et al.* [2007]. The final section of this chapter will detail the changes made to the model as part of this research to allow the code to simulate larger more realistic fault zone development within different lithologies. The final section will also include descriptions of new display routines which have allowed close examination of the stress and strain changes around a failure.

3.1 The theory of mechanical modelling of rocks

In order to model the macroscopic behaviour of a brittle rock we have assumed that it behaves as a continuum. This assumption is also made in Linear Elastic Fracture Mechanics (LEFM) [*Pollard and Segall,* 1987]. The continuum approach means that the rock is assumed to behave as a homogeneous medium and any fracturing present is represented by reduced material properties (e.g. Young's modulus, Poisson's ratio, strength) for that particular section of rock. For example Figure 3.1a shows a splay fracture in sandstone, this whole area could be represented by a single homogeneous square with material properties reflecting the degree of fracturing or it could be divided into smaller sections (Figure 3.1b) with each small section being given material properties reflecting the degree of fracturing within that particular section (Figure 3.1c). Using a finer grid allows more detailed structures to be simulated, compare figures 3.1c(i) and 3.1c(ii).

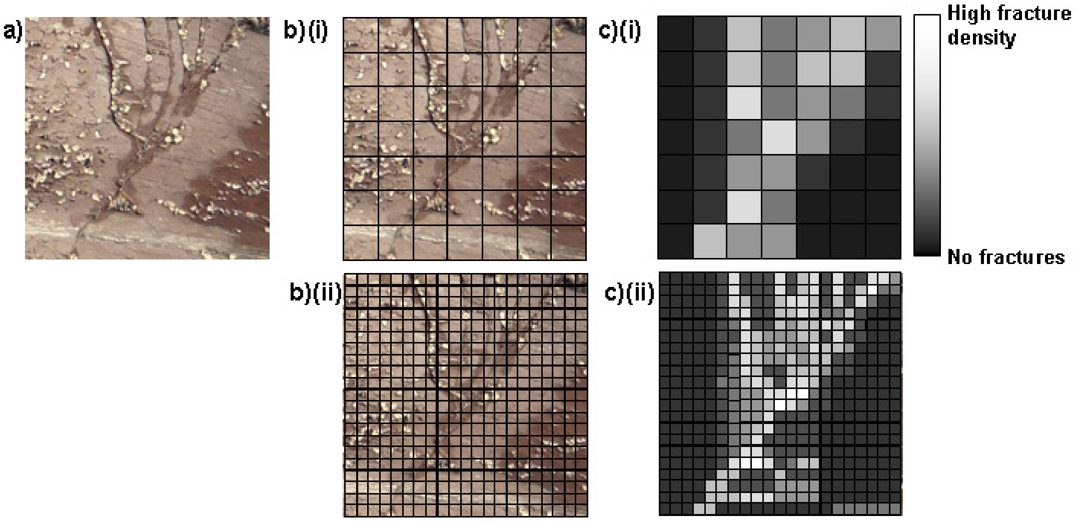

Figure 3.1 – Illustration of the continuum approach. a) Splay fractures in a sandstone exposure (photo taken by author). b) Divide exposure into a grid for finite element simulation (i) coarse grid (ii) fine grid. c) Grid of homogeneous elements the material properties of which represent the degree of fracturing in that element, as the grid becomes finer the detail of the fracture pattern become more apparent.

Assuming that the rock behaves as a continuum allows standard equations of stress and strain to be used. The concepts of stress, strain and Mohr-coulomb failure envelopes will only be discussed briefly as they are readily available in many text books [*Benham et al.,* 1996; *Craig,* 1999; *Scholz,* 2002].

3.1.1 Stress

Stress is the total force acting across a real or imaginary surface of an element of unit area. The stress on a plane can be resolved into a normal stress and two shear stresses, Figure 3.2.

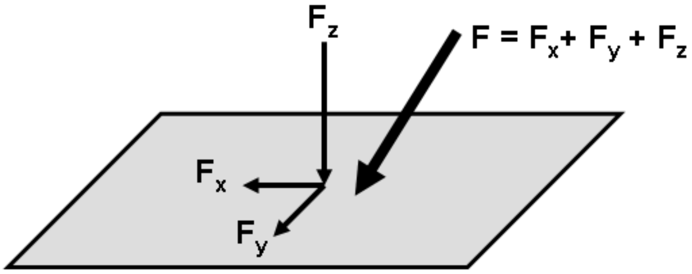

Figure 3.2 Total force acting on the plane is equivalent to the sum of 3 mutually perpendicular forces F_x, F_y and F_z

As we have assumed the rock behaves as a continuum, stress will vary continuously over the surface of the rock unit and through the body of the unit, it is useful therefore to define stress at a point for that unit. To do this we imagine a small cube the dimensions of which are δx, δy and δz, if these are small enough (as they tend to zero) the stress, and hence the force, can be considered constant over the face of the cube. The force acting on each face can be resolved, as above, into three mutually perpendicular forces, Figure 3.3.

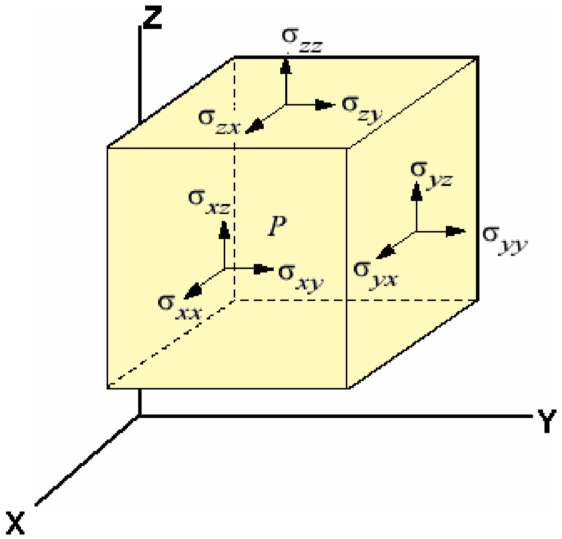

Figure 3.3 - Stress at point P on a small cube

Hence the stress at point P can be expressed by the tensor :-

$$\mathbf{S} = \begin{pmatrix} \sigma_{xx} & \sigma_{xy} & \sigma_{xz} \\ \sigma_{yx} & \sigma_{yy} & \sigma_{yz} \\ \sigma_{zx} & \sigma_{zy} & \sigma_{zz} \end{pmatrix}$$

By assuming the sides to be very small we can determine that:-

$$\mathbf{F} = \nabla . \mathbf{S} \qquad \text{where} \quad \mathbf{F} = (F_x, F_y, F_z)$$

3.1.2 Strain (E)

Stress is not observed in geology, only the results of stress as the rock is deformed. Strain is the amount of deformation an object experiences. Like stress, strain is a tensor with values dependent on the choice of coordinate axes. In one dimension stress can be expressed as the change in length over the original length. The same concept holds for strain, **E**, in three dimensions and it can be shown that :

$$\mathbf{E} = \tfrac{1}{2} (\nabla \mathbf{u} + \nabla \mathbf{u}^T)$$

where $\mathbf{u} = (u, v, w)$ i.e. the displacement in the x, y and z directions.

3.1.3 The relationship between stress and strain

Standard formulae can be derived that relate stress and strain [*Benham et al.,* 1996; *Craig,* 1999; *Scholz,* 2002] through the use of Young's modulus (*E,* not to be confused with strain **E**) and Poisson's ratio (υ) . Young's modulus is a measure of the stiffness of a material, the higher the value, the stiffer the material; rubber for example has a Young's modulus of around 0.05 GPa whereas diamond has a Young's modulus of around 1220 GPa. Poisson's ratio is a measure of how the shape of the deformed material changes (the ratio of transverse contraction strain to longitudinal expansion strain), for isotropic linear elastic materials the values range from 0 for materials which don't change shape prior to failure to 0.5 for materials such as rubber which easily change shape prior to failure. Young's modulus and Poisson's ratio are considered constant for any given material at a given temperature and pressure and are sufficient to relate stress and strain, however, the formulae are simplified by utilising additional constants namely the 1st and 2nd Lamé constants, λ and μ_L, and the bulk modulus, K_{bm} (the shear modulus G is equivalent to μ_L and is often referenced rather than the 2nd Lamé constant). The standard formulae are:

$$\lambda = E\upsilon \ / \ (1+\upsilon)(1-2\upsilon)$$

$$\mu_L = G = E/\ 2(1+\upsilon)$$

and

$$K_{bm} = E/\ 3(1-2\upsilon)$$

Hooke's law states that elastic strain is proportional to the stress applied, a generalization of that law is:

$$\mathbf{S} = C\,[\mathbf{E}]$$

Where **S** is the 3x3 stress tensor, **E** (not to be confused with young's modulus *E*) is the strain tensor and C is the stiffness matrix, the exact form of which is determined by the material, but in the case of linear elastic mechanics will consist of the various formulas involving the 1st and 2nd Lame constants, λ and μ_L. For the simple case of an isotropic medium this can be simplified to

$$\begin{bmatrix} \sigma_{xx} \\ \sigma_{yy} \\ \sigma_{zz} \\ \sigma_{yz} \\ \sigma_{zx} \\ \sigma_{xy} \end{bmatrix} = -\begin{bmatrix} 2(\mu_L+\lambda) & \lambda & \lambda & 0 & 0 & 0 \\ \lambda & 2(\mu_L+\lambda) & \lambda & 0 & 0 & 0 \\ \lambda & \lambda & 2(\mu_L+\lambda) & 0 & 0 & 0 \\ 0 & 0 & 0 & 2\mu_L & 0 & 0 \\ 0 & 0 & 0 & 0 & 2\mu_L & 0 \\ 0 & 0 & 0 & 0 & 0 & 2\mu_L \end{bmatrix} \begin{bmatrix} \varepsilon_{xx} \\ \varepsilon_{yy} \\ \varepsilon_{zz} \\ \varepsilon_{yz} \\ \varepsilon_{zx} \\ \varepsilon_{xy} \end{bmatrix}$$

3.1.4 Navier's Equation

Navier's equation models the physical deformation of a solid when it is subjected to external forces. A steady state version of Navier's equation is derived by combining the standard equations for stress and strain detailed above.

$$\nabla \bullet c \nabla \mathbf{u} = \mathbf{F}$$

where *c* is a matrix such as the one shown above where each entry is a function of λ and μ_L, and $\mathbf{u} = (u, v, w)$ i.e. the displacement in the x, y and z directions.

It is possible to derive a full time-varying version of Navier's equation however this level of complexity is not modelled by MOPEDZ. The justification for implementing the simpler steady state version of Navier's equation is that fault evolution appears to happen in stages; there is rapid movement as a slip event occurs followed by a period of little or no movement which persists until local stresses are sufficient to trigger further failure with associated rapid movement. In addition we are not attempting to simulate seismic faults.

3.1.5 Mohr's Circle

The Cartesian stress tensor discussed in 3.1.1 is dependent on the coordinate axes, *x, y* and *z*, but the orientation of these axes can be varied resulting in different values of stress. There always exists an orientation of the reference frame such that the shear stresses on the surfaces aligned with the Cartesian planes are zero [*Timoshenko and Goodier,* 1970].

If we consider stress in two dimensions, it is possible to calculate all the possible states of stress for varying rotations of the coordinate axes, the graphical representation of this is known as Mohr's circle.

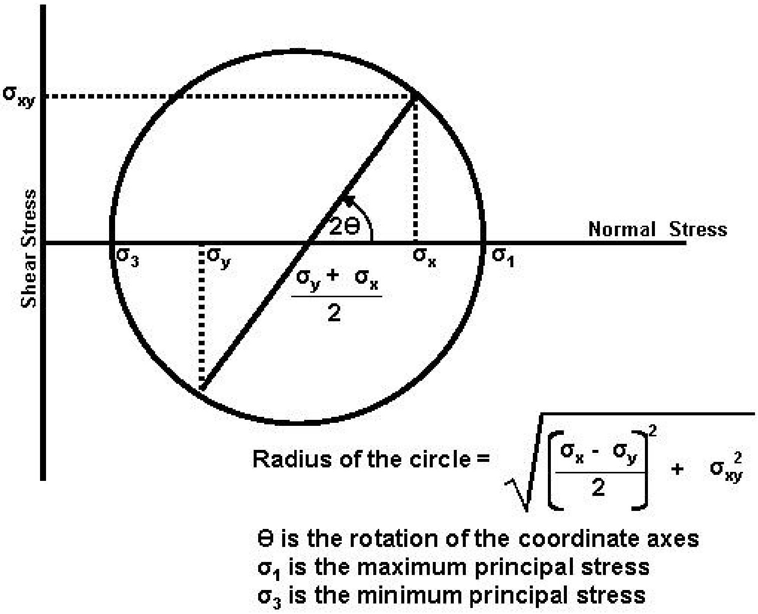

Figure 3.4 – Mohr circle. When coordinate system is rotated such that the shear stress σ_{xy} is equal to zero the principal stresses are denoted by σ_1 and σ_3.

3.1.6 Failure Criteria

Having modelled how a material may behave when forces (stresses) are applied, the next criteria which has to be established is how the material might fail. When rock (or any material) is stressed it may deform either elastically, returning to its original shape when the force is removed, or plastically undergoing some form of permanent deformation. For very small loads rock will behave elastically but for most forces once the rock deforms irreversible changes occur, e.g. fracturing, folding or formation or deformation bands.

To simplify the modelling only brittle rocks (as defined in Chapter 2) will be modelled allowing us to assume perfectly elastic behaviour. To model more ductile rocks an elasto-plastic behaviour would have to be considered where Young's modulus is no longer constant once the elastic limit has been reached but is in fact a function of both stress and strain [*Galli et al.,* 2004].

Even once we have assumed elastic behaviour there are still a number of failure criteria which can be chosen. Generally these are either based on a regional stress field or a local stress field. Models of fracture development in rock based on linear elastic fracture mechanics [*Segall and Pollard*, 1983; *Martel*, 1990; *Bergbauer and Martel*, 1999] have a failure criteria based on regional values of stress. They assume an infinite domain where the material behaves as a continuum and that any fracture is both perfectly planar and has zero width, and that there is no friction between adjacent sides. The failure criteria of these models distinguish different modes of failure; tension or two types of shear, Figure 3.5. Each mode of failure has a different stress intensity factor based on the assumed regional stress field, different researchers have used this stress intensity to establish different failure criteria [*Du and Aydin*, 1993; *Shen*, 1993]. These failure criteria assume failure based on a single fracture in a regional stress field and are related to the length of the original fracture. As MOPEDZ will model the evolution of a fault zone, with an associated damage zone which may contain many fractures and/or faults, these failure criteria are not the most effective. It is more useful to use a failure criteria based on the local stress field so as to account for stress changes imposed on the regional stress field by features such as other proximal fractures/faults.

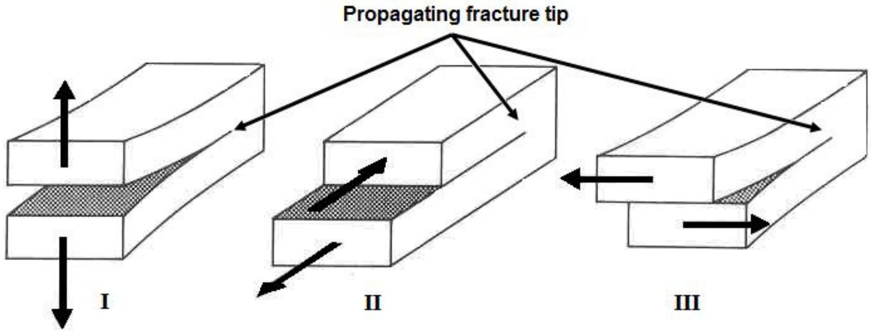

Figure 3.5 – Failure modes. Fracture tip is propagating in the same direction but each has a different mode of failure. Mode I is tension, modes II and III are in shear. [*Scholz*, 2002]

Failure criteria based on the local stress field have generally been established through laboratory testing and are very dependant on the rock type or material being tested. Many models are two dimensional and only consider the maximum compressive stress, $\sigma_{1,}$ and the minimum compressive stress, $\sigma_{3,}$ and ignore the effect of σ_2. Many lab tests, and hence the data available for modelling, use the same value for σ_2 and σ_3. True triaxial testing as carried out by *Haimson and Chang* [2000] showed that the effect of having a different value for the intermediate principal stress is not insignificant. However, whilst variations in the load at which the failure occurs could be related to variations in σ_2, the general shape of the structures obtained were very similar to those tests where σ_2 and σ_3 were the same. *Healy et al.,* [2006] developed a 3D model of fracture development and they too showed that consideration of σ_2 does alter the geometry of the structures obtained however, when a slice is taken through their 3D model, the plots are consistent with 2D simulations produced by other researchers, which effectively ignore the effect of σ_2.

When modelling, the most commonly used failure criteria for brittle rock is the Mohr-Coulomb envelope, which is only appropriate for failure in compression (Figure 3.6). If the the Mohr-coulomb envelope was extended to the normal stress axis, the angle it makes, φ, is termed the angle of internal friction. When modelling it is more common to use the coefficient of internal friction, μ, given that $\varphi = \tan^{-1} \mu$. Failure at location A on the Mohr-Coulomb envelope is in tension (extension) failure, at location C (on the linear part of the Mohr-coulomb envelope) failure is in shear and at location B it is a combination of the two.

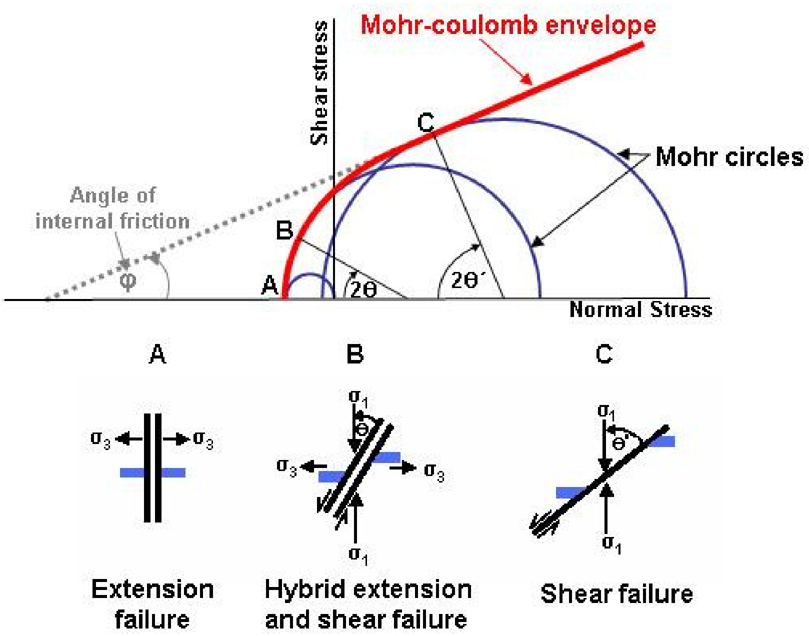

Figure 3.6 – Mohr-Coulomb failure criteria (after [*Singhal and Gupta*, 1999])

A number of numerical models have been developed using the criteria discussed above. These models have simulated the evolution of wing cracks from the tips of pre-existing structures [*Shen and Stephansson*, 1993; *Burgmann et al.*, 1994; *Kattenhorn et al.,* 2000; *Willson et al.*, 2007] or the linkage of pairs of faults with dilational and contractional geometries [*Du and Aydin*, 1995; *Bremaecker and Ferris* 2004; *Lunn et al.*, 2008]. These simple 2D models have enabled prediction of the orientation of linkage fractures and their mode of failure, for a single fracture or pair of fractures in an ideal homogeneous medium. However, these simulations, derived from one or two fractures, are not sufficient to understand the range of complex geometries observed in the field, examples of which are shown in Figure 3.7.

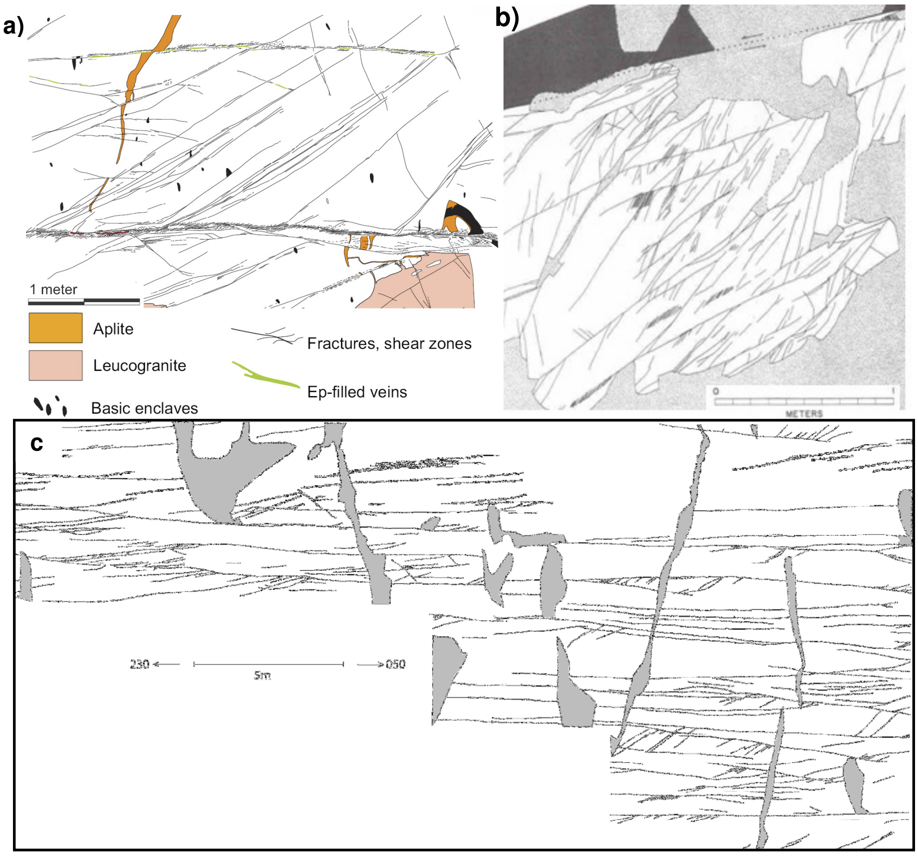

Figure 3.7 - Field examples of mapped sections from fault zones a) A segment of the outcrop map from NE of Neves lake in the Italian Alps showing a section of fault zone with smooth planar features [*Pennacchioni and Mancktelow*, 2007] b) A segment of the outcrop map from the Waterfall region in the Sierra Nevada, California [*Martel*, 1990]. c) Map of fractures in an exposure of the Lake Edison granodiorite in the Bear Creek region in the Sierra Nevada, California, UTM coordinates are: 0333075 4136569, mapped by J. Kirkpatrick, University of Glasgow. [*Moir et al.*, 2010]

3.2 Early Development of MOPEDZ code.

As mentioned in the introduction, this research utilises a computer code called MOPEDZ (Modelling Of Permeability Evolution in the Damage Zone surrounding faults) to simulate spatial and temporal evolution of complex patterns of linking fractures. MOPEDZ was developed using the commercially available finite-element software COMSOL which is called from within the MATLAB code. The COMSOL finite-element routines assume plane strain during the simulations. MOPEDZ is a two-dimensional finite-element model which solves Navier's equation in a series of 'quasi' steady states and uses a combined Mohr Coulomb and tensile failure criteria. Elements within the finite element mesh are either intact host rock or fractured host rock. Elements which contain fractures (including the initial joints) are represented by lower effective material values (10% of the host) for Young's modulus, Poisson's ratio and material strength (shear and tensile), in a similar approach to *Tang* [1997]. Representing the accumulation of damage within each element by altering that element's material properties is consistent with other damage mechanics models [*Jing,* 2003]. Shear strength is the stress at which unconfined rock fails in shear [*Orbert et al.* 1946].

The initial configuration for all MOPEDZ simulations is similar to that illustrated in Figure 3.8 with the host rock (granodiorite) having the properties listed in Table 3.1 and any elements containing pre-existing joints having reduced material properties (10% of the host) [*Willson et al.,* 2007]. The simulated maximum compressive far-field stress direction, σ_1, is parallel to the y axis (i.e. top-to-bottom in all MOPEDZ figures) and the minimum, σ_3, is parallel to the x axis (i.e. left–to–right in all MOPEDZ figures) (Figure 3.8). Note that in the field (with the exception of the ignimbrite simulations discussed in Chapter 5) both σ_1 and σ_3 are horizontal. Early simulations using MOPEDZ displaced the top and bottom (σ_1) boundaries while the side boundaries were either held constant or were free to move. Later simulations (including those presented in the following chapters) were conducted such that initially all boundaries are displaced inward holding $\sigma_1 = 2\sigma_3$, (in compression) however following the first failure (either Mohr Coulomb or tensile) the σ_3 boundaries are held constant and from that point on only the σ_1 boundaries are displaced towards each other i.e. σ_1 progressively increasing with σ_3 held constant. All simulations presented within this thesis are in compression. Throughout this thesis σ_1 and σ_3 refer to the far-field stress imposed by the boundaries of the finite-element model and σ_1^{Local} and σ_3^{Local} refer to the local stress field around damaged cells. All simulations use square finite-elements.

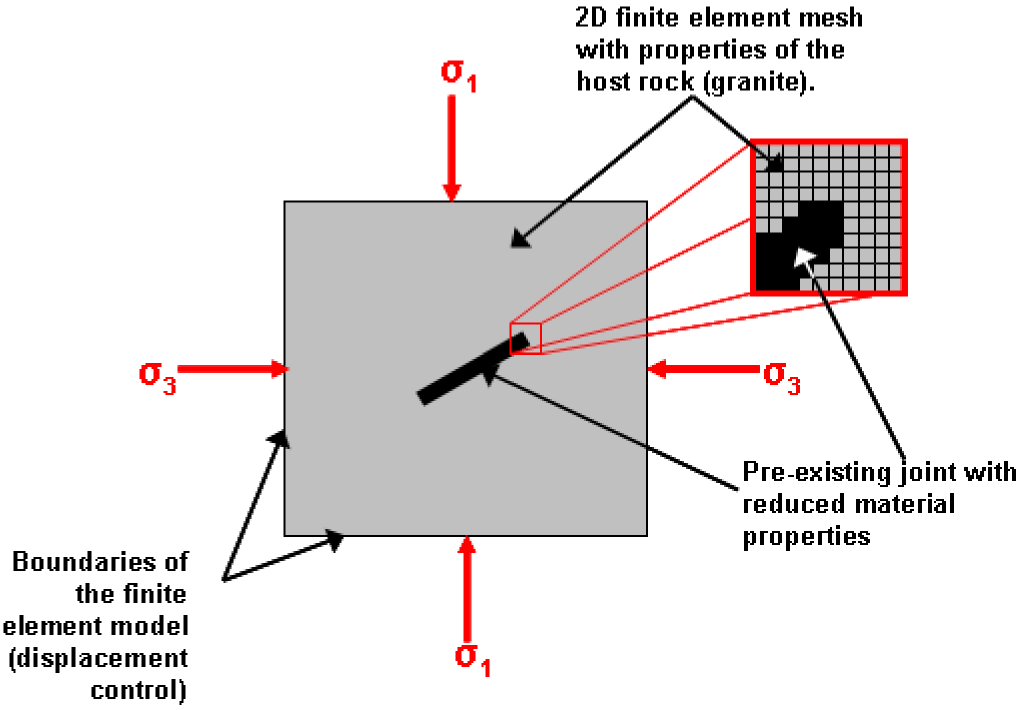

Figure 3.8 – Initial configuration for MOPEDZ simulation from a single joint.

In MOPEDZ as an element fails (in either shear or tension) its material properties are altered. Although the first failures are triggered by displacement of the boundaries, the alteration of the material properties of those failed cells causes a change in both the direction and magnitude of σ_1^{Local} and σ_3^{Local} [*Lunn et al.,* 2008]. This alteration of the local stress may be sufficient to trigger additional failures without any further displacement of the model boundaries. These subsequent failures can be adjacent to previous failures, i.e. representing the lengthening of a macroscopic fracture, or they can occur in locations that are disconnected from any previous failure, or they may be further fracturing of the same element or any combination of these. As discussed in section 3.1.6 the material is assumed to behave in a perfectly plastic manner, however, it has been shown that even brittle rocks show a change in material properties as they approach failure [*Heap and Faulkner*, 2008]. *Hamiel et al*., [2006] examined micro-crack density in brittle rocks which showed that damage starts to develop well before failure occurs and that the evolution of this damage affects the mechanical properties of the rock. Within the MOPEDZ model, to reflect this change in material properties, each element may fail up to a maximum of six times (resulting in a reduction of strength, Young's modulus and Poisson's ratio); material properties are progressively reduced using a geometric sequence [*Willson et al*., 2007] until they reach the lowest value permitted which is equivalent to the starting value for the pre-existing joints. I would emphasise that each element in the mesh may represent, at a sub–element scale, any number of micro or macroscopic failures in the field.

Table 3.1: MOPEDZ simulation parameters for brittle rock. Where relevant the right hand column contains the reference from which the value of the mechanical property was derived.

Rock Property	**Value**	**Reference**
Host Rock Young's modulus	60 GPa	*Martin* [1997] *Turcotte and Schubert* [2002]
Host rock Poisson's ratio	0.2	*Turcotte and Schubert* [2002]
Young's modulus of fractured element	1.2 GPa	*Segall and Pollard* [1983]
Poisson's ratio of fractured element	0.02	
Co (Shear strength)	130 MPa	*Martin* [1997]
μ (Coefficient of friction)	0.6	*Byerlee* [1967]
To (Tensile strength)	10 MPa	*Martin* [1997]
Number of cells permitted to fail in any one step of the MOPEDZ code	6	

Once a steady-state solution has been achieved for a given boundary displacement, the top and bottom boundaries undergo further displacement towards each other and the whole solution process is repeated. During any one iteration of the code, only a small number of elements (<6 in most simulations) are permitted to fail to ensure stability of the model solution and provide an estimation of the temporal propagation of the fractures. Many hundreds of simulations have shown that this number allows controlled failure of the simulation and produces structures observed in the field.

3.3 Better understanding of MOPEDZ

As stated previously initial development of MOPEDZ was carried out by *Willson, et al.*, [2007], the model had, on a small scale, in homogeneous rock successfully simulated the features illustrated in Figure 2.15, for example

Figure 3.9 shows the evolution of multiple wing cracks from a pre-existing joint which compares well to multiple wing cracks mapped by *Lim* [1998], Figure 3.10

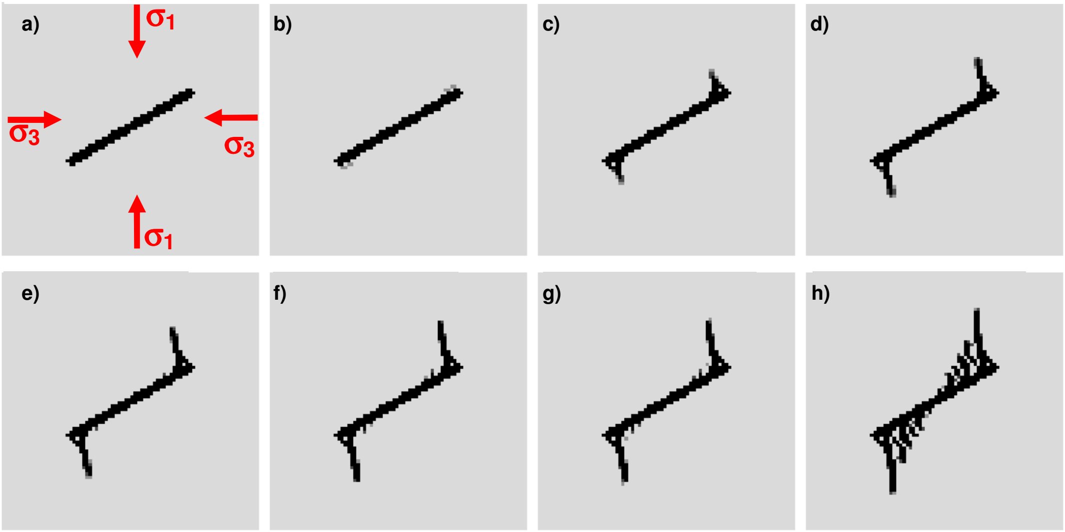

Figure 3.9 – MOPEDZ simulation of multiple wing cracks forming from a single pre-existing joint, after Figure 6.12 in *Willson* [2006]

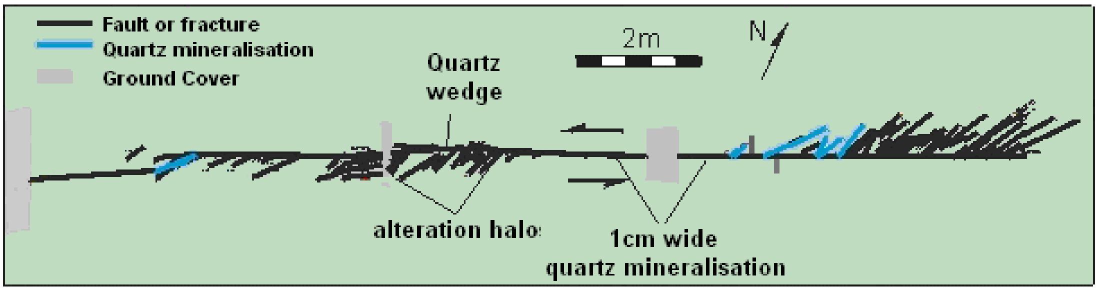

Figure 3.10– Mapped exposure showing multiple wing cracks on the fault, [*Lim*, 1998].

My initial research re-examined these early simulations of wing crack development from single (or pairs of) pre-exiting joints in order to obtain a better understanding of what changes were occurring to the local stress field and how those changes were affecting the evolving fractures. This was carried out by looking in detail at the stress changes around the tip of the fracture, plots were produced in COMSOL which show the ratio of σ_1 to σ_3 at regular points across the whole model domain, Figure 3.11.

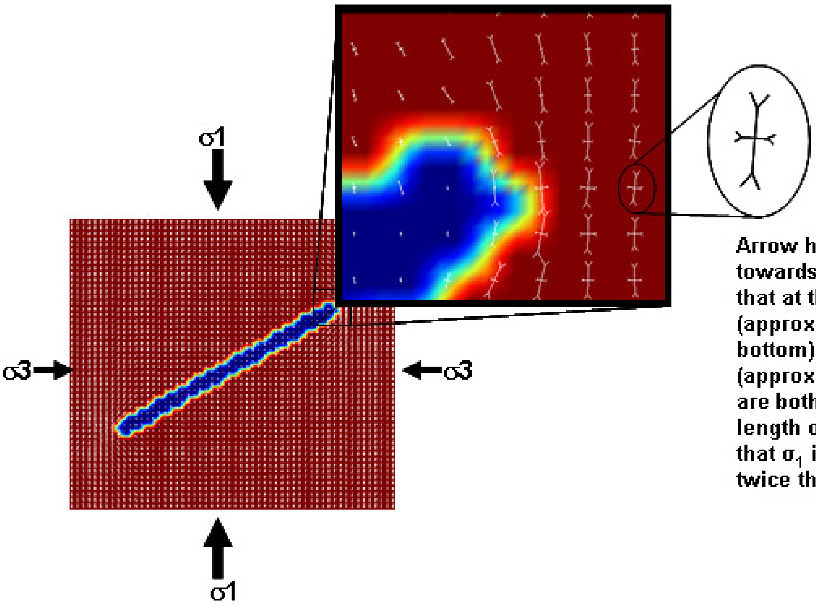

Arrow heads pointing towards each other show that at this exact location σ_1 (approximately top-to-bottom) and σ_3 (approximately left –to-right) are both in compression. The length of the arrows shows that σ_1 is approximately twice the value of σ_3.

Figure 3.11 – MOPEDZ plot with stress arrows overlaid. Zooming in on the tip of the fracture allows the rotation of the local stress to be observed. Each pair of arrows indicates the direction and relative size of σ_1^{LOCAL} and σ_3^{LOCAL} at that point in the finite element model. Colours simply represent Young's modulus to highlight where the fracture is in the simulation.

Initial simulations conducted by *Willson, et al.*, [2007], considered two scenarios for wing crack development from a single fracture. In the first the top and bottom (σ_1) boundaries were displaced towards each other while the side boundaries were free to move, this resulted in a high stress ratio with $\sigma_1 >> \sigma_3$, in the second the side boundaries are fixed which results in a low stress ratio with $\sigma_1 \approx 2\sigma_3$. The different scenarios resulted in wing crack evolution at different orientations, Figure 3.12; this does not suggest that the ratio of σ_1 to σ_3 is the only control on wing crack evolution.

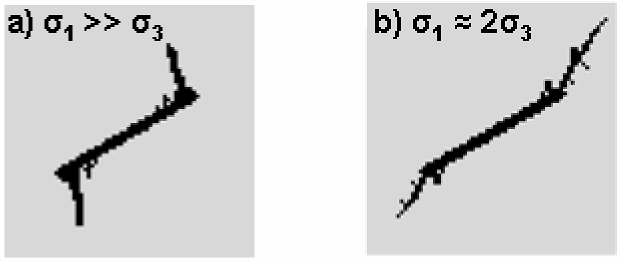

Figure 3.12 – A single pre-existing joint at 60° to σ_1 develops different wing crack geometries when the ratio of σ_1 to σ_3 is changed from (a) high ($\sigma_1 >> \sigma_3$) to (b) low ($\sigma_1 \approx 2\sigma_3$).

Close examination of the stress field and failure mechanism around the tip of a propagating fracture for the first scenario (side boundaries free to move, $\sigma_1 >> \sigma_3$) revealed that failure is predominately in tension. Close examination of the local stress changes show a marked change in the direction of the local maximum compressive stress (σ_1^{LOCAL}) and in the ratio of σ_1^{LOCAL} to σ_3^{LOCAL}, this is illustrated in Figure 3.13. The local stress at the point marked by the red oval in Figure 3.13 initially shows the simulated regional stress with σ_1^{LOCAL} vertical and much larger than σ_3^{LOCAL}. As the wing crack evolves there is a marked change in the rotation of the local stresses coupled with a change in the ratio of σ_1^{LOCAL} to σ_3^{LOCAL}, Figure 3.13. Failure of the central point is in tension; this point does not show the highest stress value (largest arrow) but does show the lowest ratio of σ_1 to σ_3 and the largest rotation of the local stress field. As the fracture continues to propagate, the local stresses on either side of the fracture begin to align with the fracture and the ratio of σ_1^{LOCAL} to σ_3^{LOCAL} returns to being high.

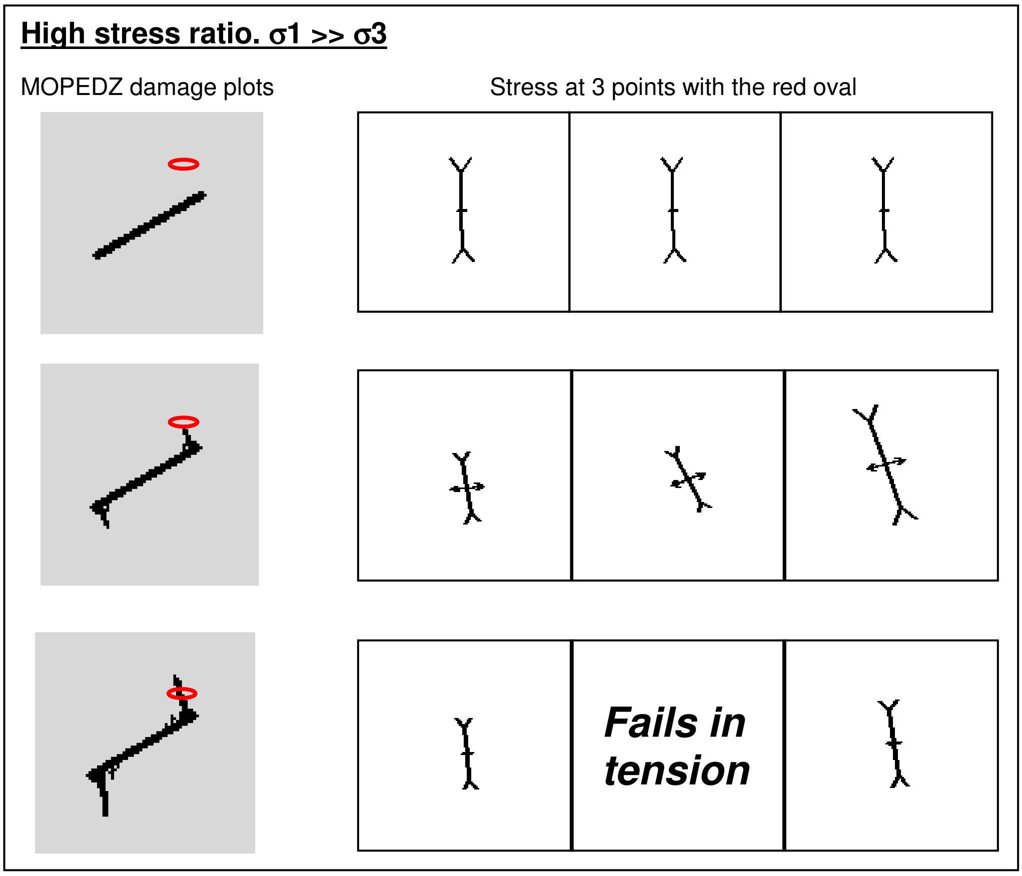

Figure 3.13 – Rotation and change in ratio of local σ_1 to σ_3 as a wing crack develops with a regional σ_1 much larger than σ_3. The stress arrows for 3 points with the red oval are shown, initially the show the simulated regional stress, then the stress arrows show a marked change in the local stress as the fracture develops.

Close examination of the stress field and failure mechanism around the tip of a propagating fracture for the second scenario (side boundaries fixed, $\sigma_1 \approx 2\sigma_3$) revealed that failure is predominately in shear. Close examination of the local stress changes show a marked change in the direction of the local maximum compressive stress (σ_1^{LOCAL}) and in the ratio of σ_1^{LOCAL} to σ_3^{LOCAL}, this is illustrated in Figure 3.14. As before, the local stresses in the cells within the red oval marked in Figure 3.14 initially show the simulated regional stress with σ_1 vertical and larger than σ_3 and all in compression. As the wing crack evolves there is a marked change in the rotation of the local stresses coupled with a change in the ratio of σ_1^{LOCAL} to σ_3^{LOCAL}, Figure 3.14. Failure of the central point is in shear; this point does not show the highest stress value (largest arrow) but does show the largest change in the ratio of σ_1 to σ_3 combined with a rotation of the stress field. As the fracture continues to propagate the stresses in the cells on either side of the fracture begin to align with the fracture and the ratio of σ_1^{LOCAL} to σ_3^{LOCAL} begins to return towards its original value.

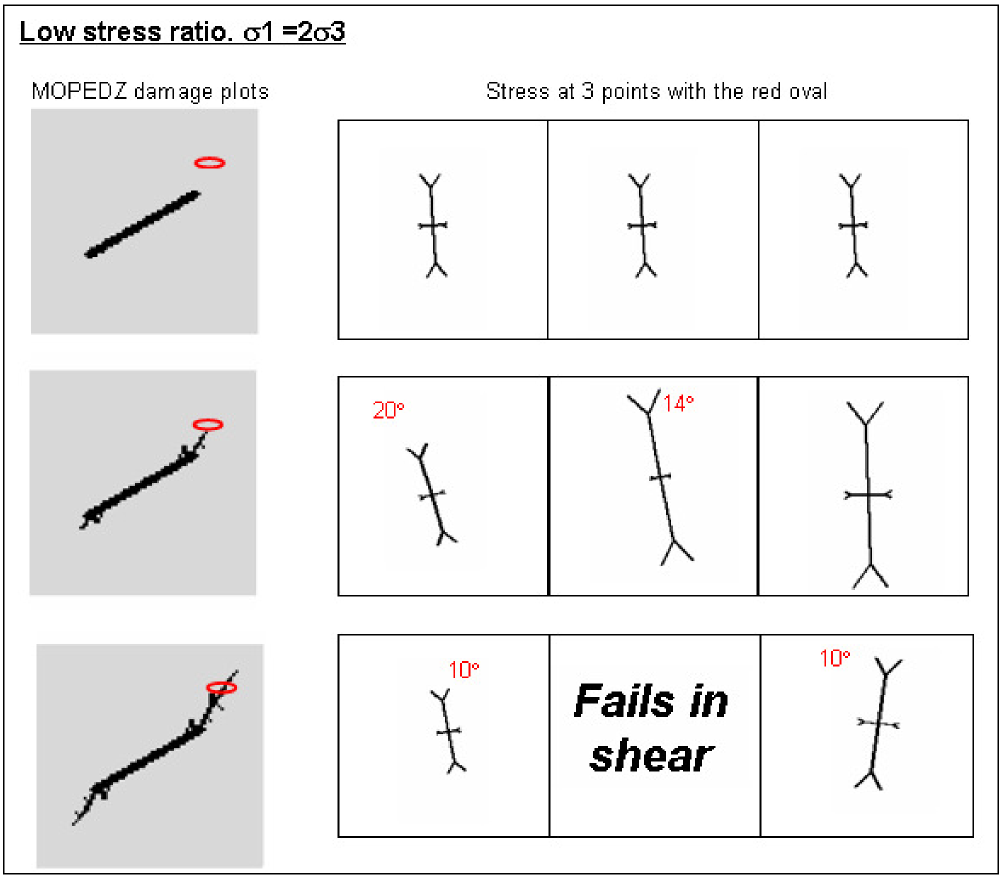

Figure 3.14 – **Rotation and change in ratio of local σ_1 to σ_3 as a wing crack develops with a regional σ_1 twice that of σ_3 . The stress arrows for 3 points with the red oval are shown, initially the show the simulated regional stress, then the stress arrows show a marked change in the local stress as the fracture develops.**

My results (Figures 3.13 & 3.14) contributed to our understanding of the evolution of the fractures and were published with *Lunn et al.*, [2008].

3.4 Linkage of pairs of joints

Earlier research using MOPEDZ to examine failure from a single joint [*Willson et al.,* 2007] shows that fracture-trace geometries are not sensitive to the initial mechanical properties of the host rock (Table 3.1). In other words, if the Young's modulus of the crystalline host rock is reduced, the same trace geometries are formed but at lower values of the displacement of the boundaries. Fracture-trace geometries are principally determined by local variations in the Young's modulus (i.e. previously damaged elements or material discontinuities), the orientation of the pre-existing joint to the far-field maximum compressive stress and the ratio of σ_1 to σ_3. Earlier research also showed that in simulations where $\sigma_1 >> \sigma_{3,}$ the mode of failure is predominately in tension (Figure 3.13), and for those where σ_1 is close to $2\sigma_{3,}$ the mode of failure is predominately in shear (Figure 3.14). This variation in the failure modes results in different orientations of the evolving wing cracks.

MOPEDZ simulations of fault linkage involving just two initial joints [*Lunn et al.,* 2008] showed that fracture-geometries develop in a predictable way summarised in Figure 3.15. Four initial stepover geometries were modelled: (a) under-lapping extensional, (b) under-lapping contractional, (c) overlapping extensional and (d) overlapping contractional. These were modelled when applying a low stress ratio (Figure 3.15a to 3.15d) and also for a high stress ratio (Figure 3.15e to 3.15h). The geometries of linkage structures are governed by three key factors: 1) the ratio of σ_1 to σ_3, 2) the initial relative positions of the joints, specifically, contractional vs. extensional geometries and overlapping vs. under-lapping joints, 3) the orientation of the most compressive principal stress direction (σ_1) relative to the initial pair of joints.

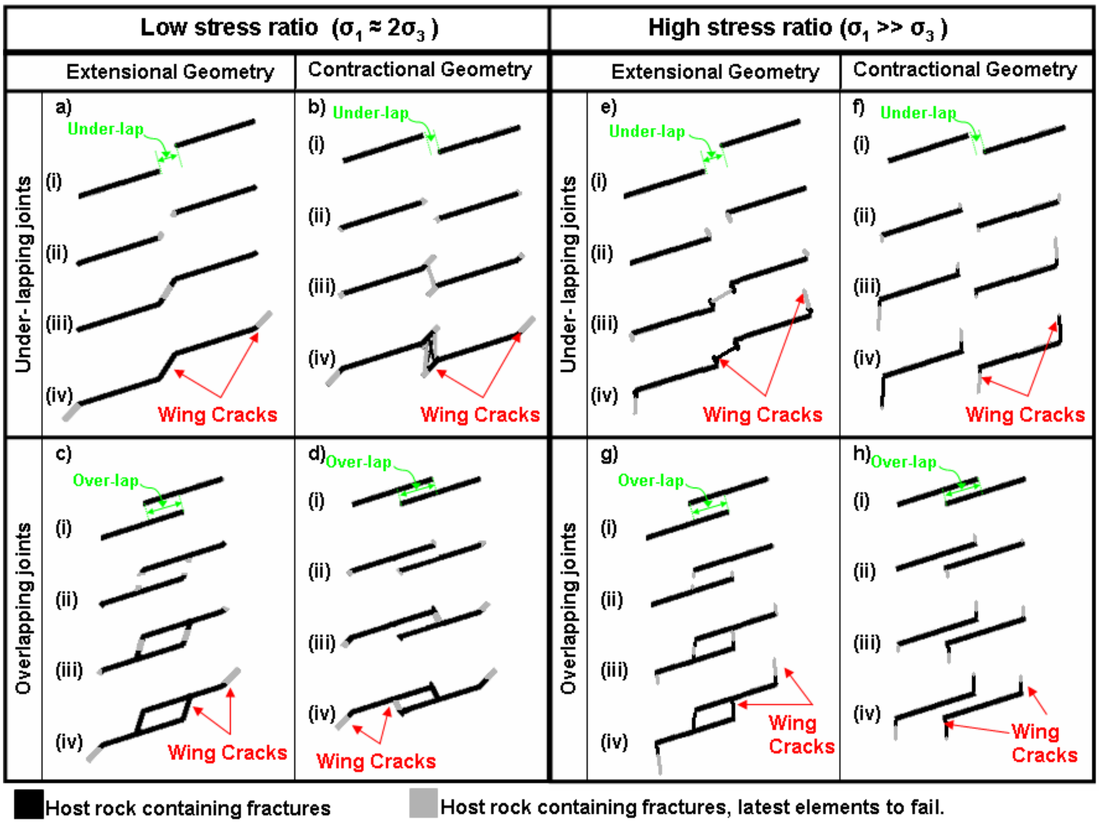

Figure 3.15 - Cartoon showing the evolution of restraining and releasing bends for a pair of overlapping and under-lapping pre-existing joints with either contractional or extensional relationship, (i) is the initial orientation of the joints, and sequences (ii) to (iv) show evolution of the predicted structure. All slipped joints are left lateral. (a) to (d) have a low stress ratio while (e) to (h) have a high stress ratio.

By examining the changes in the local stress fields around pairs of fractures it is possible to study their interaction. The alteration of σ_1^{LOCAL} and σ_3^{LOCAL} in both magnitude and direction at the tips of a propagating fracture (or the original joint) results from a combination of factors (Figure 3.16):

- The shape of the stress field around a fracture or joint is affected by its orientation with respect to the simulated far-field stresses σ_1 and σ_3 (Figure 3.16a).
- The stress fields of neighbouring faults and/or fractures interact such that they can act to enhance or diminish local perturbations in the stress field (Figure 3.16b).
- Wing cracks which have a different orientation to that of the initial joint will generate new perturbations in the local stress field (Figure 3.16b(ii) for 60°).

These factors that control the perturbations in the local stress field have an influence on the different styles of linkage structures which develop between initially co-linear joints.

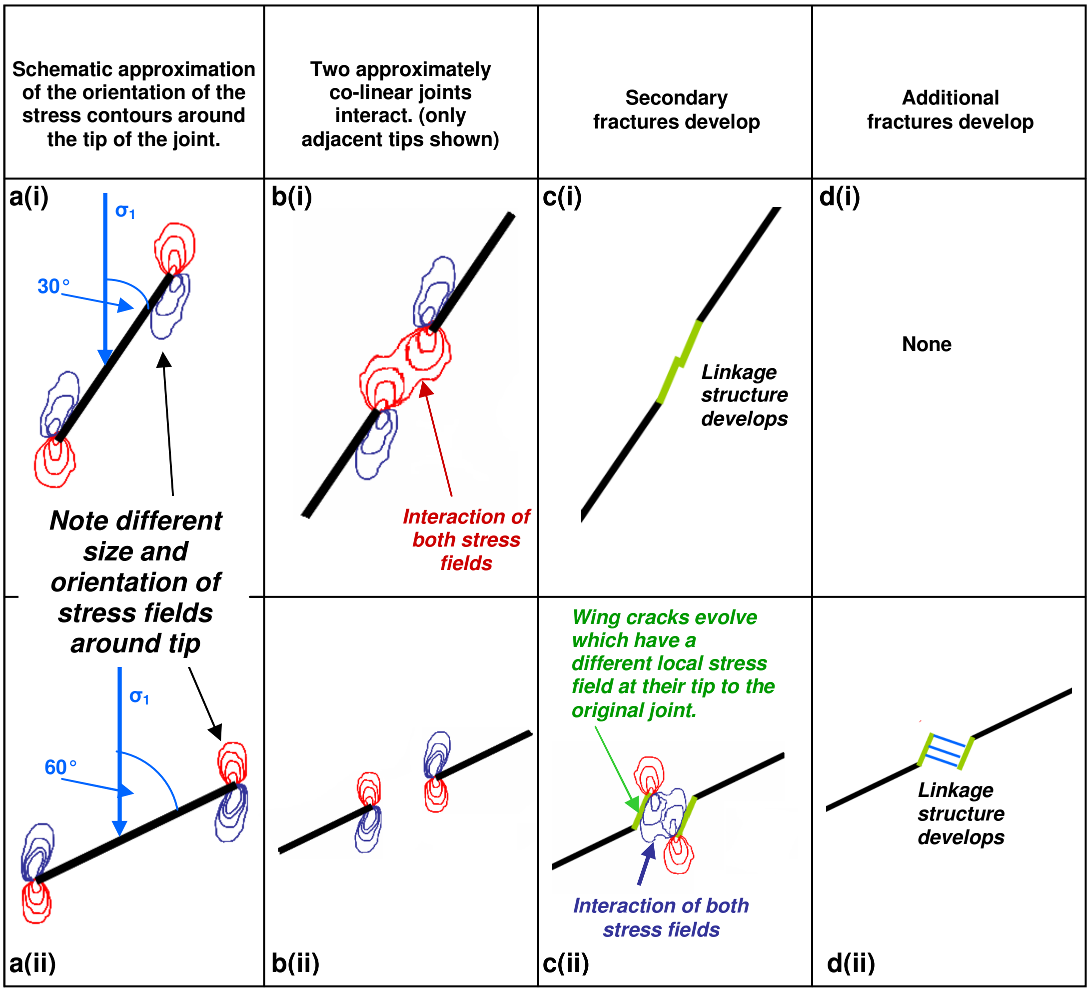

Figure 3.16 - Smoothed stress contours around the tip of a joint (or fault). a) Orientation of the joint to the far-field stress affects the orientation of the local stress field around the tip (Red contours are extensional stress contours, blue are compressional stress contours). b) Different styles of linkage structures which develop between initially co-linear joints due to different interaction of the local stress field. Here joints at 30° to σ_1 link up approximately along strike, those at 60° develop wing cracks which later link through additional fracturing when the local stress field associated with the wing cracks interact.

3.5 Further development of MOPEDZ

Having re-examined early simple simulations to gain a better understanding of the physical processes involved and the code itself it became apparent that the MOPEDZ code would require further development to allow much larger, complex simulations to be carried out. This development included:-

- Making the code more efficient to allow completion of each simulation in a realistic timescale, this had not been a consideration when MOPEDZ was developed for small scale simulations.
- The original MOPEDZ code simulated fault growth in a single homogeneous rock type and as a result variables like the coefficient of friction and density were entered into the code as a constant. This had to be changed to allow different and multiple rock types to be simulated.
- The boundary movement, particularly the side boundary movement had to be refined, to allow more geologically realistic loads to be applied.
- Large simulations required changes to be made to the control loops which ensured failure progressed in a stable way (i.e. keeping the number of elements which failed in one iteration at a low number)

Each alteration of the code was compared to known results produced by the original code for wing crack development from a single fracture at various orientations.

3.5.1 Improving efficiency

MOPEDZ uses the commercially available finite element software, COMSOL, which is executed from within MATLAB. Most of the processing time is spent on processing within COMSOL rather than within the MATLAB code. Originally, COMSOL communicated with the MATLAB source code through a number of sub-routines. It was possible to streamline these sub-routines, this reduced the processing time but not by a significant amount. Newer versions of COMSOL incorporated a number of ‘more efficient’ finite element routines (e.g. PARDISIO), these were tested and found to make very little difference. Consequently, as different routines had been extensively tested in the early development of MOPEDZ it was decided to continue with the original routines as the new ones did not improve the processing time.

The main reason for using a combination of MATLAB and COMSOL is that it is not possible to change the properties of an element, within a single iteration of the code, when using COMSOL in isolation. When an element fails stress is redistributed around the failure and this in turn may trigger further failures. This limitation in COMSOL results in having to transfer arrays of material properties in and out of COMSOL every time failure(s) is detected. In effect this meant that a brand new simulation was being initiated at each step in the iterative stage process. To increase efficiency, MOPEDZ was redesigned such that the previous solution of the COMSOL finite element routine was saved after every failure and then used as the starting point for the subsequent iteration of the code (after changing the material properties within the MATLAB source code). This modification to MOPEDZ resulted in COMSOL finding a solution much more quickly, cutting the processing time for large 160,000 element simulations by more than 50%.

3.5.2 Adjusting variables

It was envisioned that along with exploring the effect of increasing the heterogeneity of the size, shape, number and orientation of any pre-existing structures, that the code would also explore the effect of increasing the heterogeneity of host rock including having multiple rock types in a simulation. The original code was therefore modified to allow variables, such as the coefficient of friction and density, to be an array of values which could be transferred between COMSOL and MATLAB in a similar manner to other material properties such as Young's Modulus.

3.5.3 Movement of model boundaries

As discussed above the original MOPEDZ code displaced the top and bottom boundaries (σ_1) while the side boundaries (σ_3) were either fixed or free to move. These early simulations by *Willson et al.* [2007] exploring wing crack evolution from a single pre-existing fracture, showed very different crack evolution when the side boundaries were fixed (low stress ratio between σ_1 and σ_3) as compared to those simulations where the side boundaries were free to move (high stress ratio between σ_1 and σ_3), Figure 3.12. As the ratio σ_1 to σ_3 appeared to be significant the possibility of utilising load control on the boundaries rather than displacement control was explored.

The MOPEDZ code was modified to allow load control rather than displacement control on the boundaries, as this would allow different ratio's of σ_1 to σ_3 to be explored. Unfortunately, this modification resulted in rapid uncontrolled failure (more elements failing than were permitted). Many modifications were attempted to address this issue but it was not resolved. However, this modelled behaviour is also observed in experimental labs; test rigs which operate under load control tend to result in quick catastrophic failure where as those which operate under displacement control tend to produce a more stable failure (personal conversation with Prof. Chris Marone, Pennsylvania State University).

To address the problem of catastrophic failure under load control the model was adjusted to a *hybrid* approach of both load and displacement control. Initially, load control was employed to determine the displacement of the boundaries at the point when the first failure occurred. The simulation was then reset and run under displacement control with the size of the first displacement step set to the values obtained when using load control. This process resulted in the first step producing a number of failed cells within an acceptable limit and at this point (first step) the ratio of σ_1 to σ_3 was pre-determined. After this first failure the σ_3 boundaries were held constant and from this point on only the σ_1 boundaries were displaced towards each other i.e. σ_1 progressively increasing with σ_3 held constant. This allowed a compromise between setting the ratio of σ_1 to σ_3 and producing a controlled failure.

3.5.4 Ensuring stability

Once the code had been developed to simulate larger more realistic failures it sometimes proved difficult to keep the number of failed cells low (<6). In the cases where more than six elements failed (even after four reductions in the size of displacement of the σ_1 boundaries) it was decided to only fail (i.e. adjust the material properties) of the six elements associated with the six highest stress values and leave the remaining ‘failed’ elements unchanged. A simplified flow chart of the MOPEDZ code which includes this modification is shown in Figure 3.17. Once the properties of these six elements had been changed, the local stress field was recalculated, and the simulation was tested for further failures without any change in the displacement of the boundaries. This additional level of control often allowed for rapid, but controlled failure, to be predicted. Despite these modifications, uncontrolled failure still occurred in some simulations.

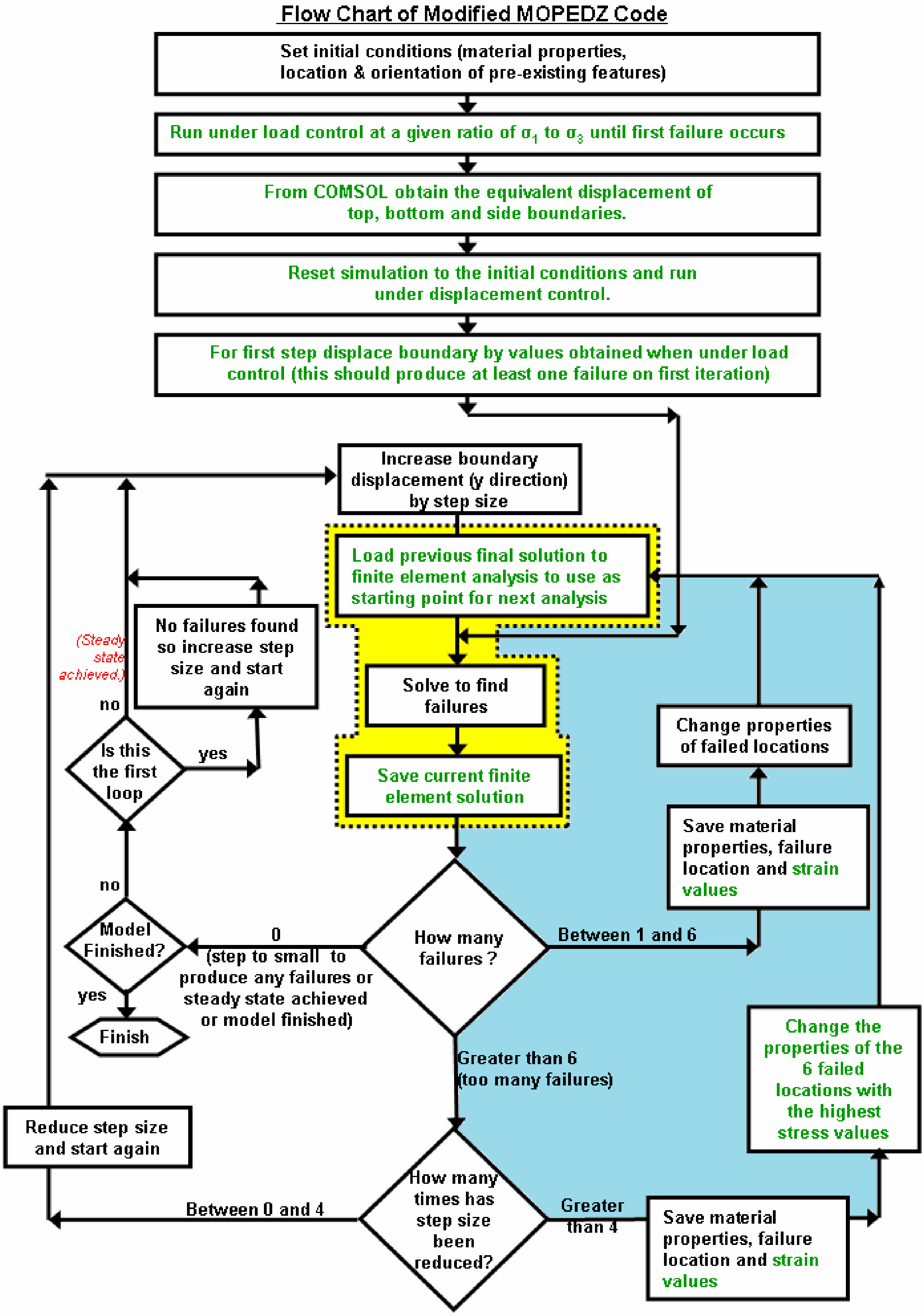

Figure 3.18 - Simplified flow diagram illustrating the modified MOPEDZ code. Steps in Green are modifications to the original code, those steps shaded in yellow are carried out within COMSOL, loop(s) in the 'blue' section of the diagram are carried out until a stable state is achieved or for a single displacement of the boundary the iterations reach 100 (this number will only be reached if there is uncontrolled failure).

3.6 Displaying Output from MOPEDZ

Plots showing the results from MOPEDZ simulations are either produced within COMSOL or from within MATLAB. Those produced within COMSOL have to be output during the simulation but those produced within MATLAB are generated after the simulation is complete. At each iteration of the MOPEDZ code the results (arrays containing physical properties) are saved to a file for later post-processing.

Examples of output from MOPEDZ simulations which have been presented so far are in the form of damage plots, see Figure 3.9. Damage plots show the elements that have failed - grey indicates intact host rock and black indicates fractured host rock (since individual elements may fail multiple times in shear and/or tension, modes of failure are not shown).

Surface plots of the local principal stress show the spatial distribution of σ_1^{Local}, Figure 3.18. Note that surface plots of the local principal stress were produced within COMSOL in which compression is negative and tension positive (the opposite convention is usually adopted within the geological literature).

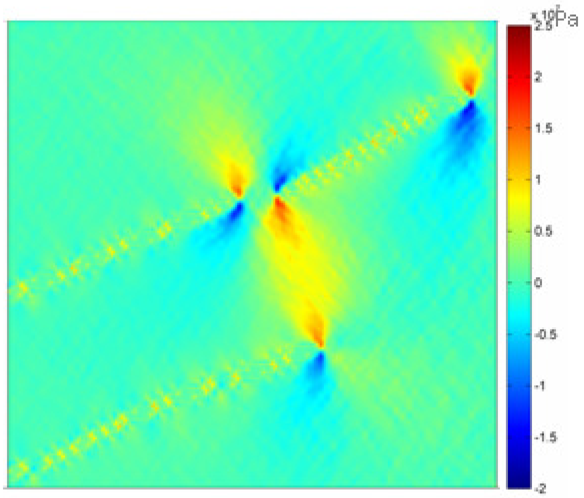

Figure 3.18 – Example of a surface plot of the local principal stress produced within COMSOL.

Within the geological literature faults are often discussed in terms of strain evolution, hence, it seemed a logical step to examine this feature. To obtain a plot of the strain evolution required significant modification to the MOPEDZ code to allow the different strain values required to generate the strain tensor to be saved during the MOPEDZ run for later post processing. The strain plots which were produced show the Euclidean norm of the strain tensor, which is one of the methods of representing the scalar magnitude of a strain tensor [*Mathews and Fink,* 2004].

It is widely accepted that in a single fault, strain (and hence displacement) is highest at the centre of the fault and reduces to zero at the tip of the fault. It is not easy to observe this feature of the strain in the thin pre-existing features typically simulated within MOPEDZ as it is often masked by the pixellated nature of the pre-existing feature. During the development of the code, to allow examination of the strain evolution a single wide fracture was simulated which does indeed show the highest strain in the centre of the fracture, Figure 3.19.

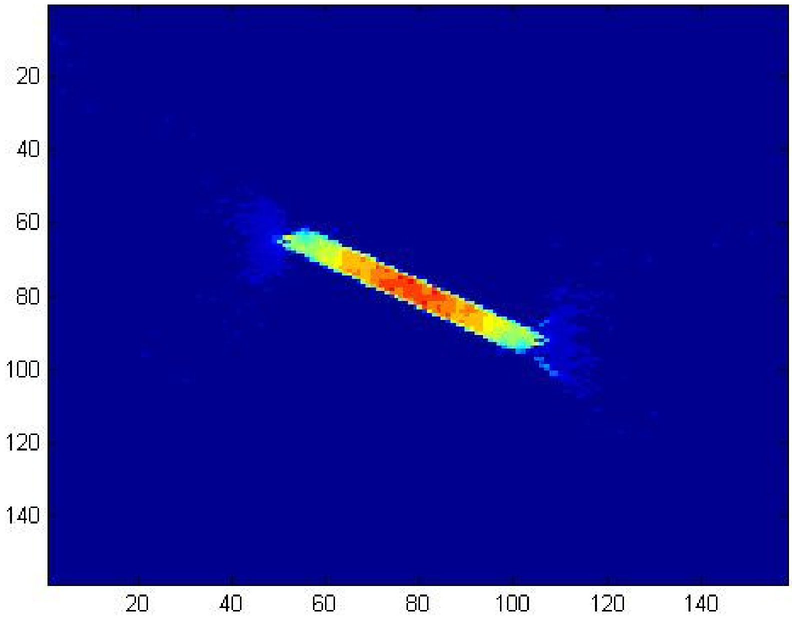

Figure 3.19 – Colour strain plot showing highest strain (red) in the centre of the fracture, reducing to the lowest (blue) towards the tip.

Plots of the norm of the strain tensors for each element elucidate a more detailed structure than the damage plots (which just show failure), since they also highlight elements which are under a high strain but that have not yet failed. An example of this distinction is shown in Figure 3.20, in this example the strain plot (Figure 3.20b) was produced using a grey scale with the highest strain as black. The strain plots are not appropriate for direct comparison with field data since all simulations start from an initial condition of zero strain. Plots show accumulated strain from the start of the simulation.

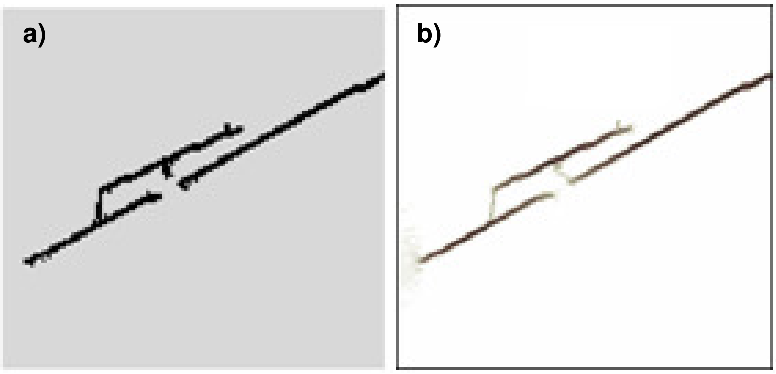

Figure 3.20 – Comparison of typical damage plot (a) and strain plot (b) for same simulation.

For the early simple plots such as those illustrated in Figure 3.9 it was sufficient to plot the complete sequence as a single figure, however once large simulations with more than 20 pre-existing joints were being carried out the output had to be changed to allow one large figure to be produced for each iteration. The reasons for this were two fold. First, the complexity of the joint pattern and evolving geometry could only be clearly seen if the figure was increased in size, Figure 3.21; secondly, these large simulations typically involved over 350 steps and could therefore not be displayed on one screen; Figure 3.22 illustrates the effect of showing just the first 28 frames of one simulation. Within this thesis, isolated frames which show a significant change in fracture pattern were chosen to best illustrate the fracture evolution. However, the most informative way of presenting the output from these large simulations, for both damage plots and strain maps, was to produce a video of the consecutive plots, examples of these are presented in Appendix A.

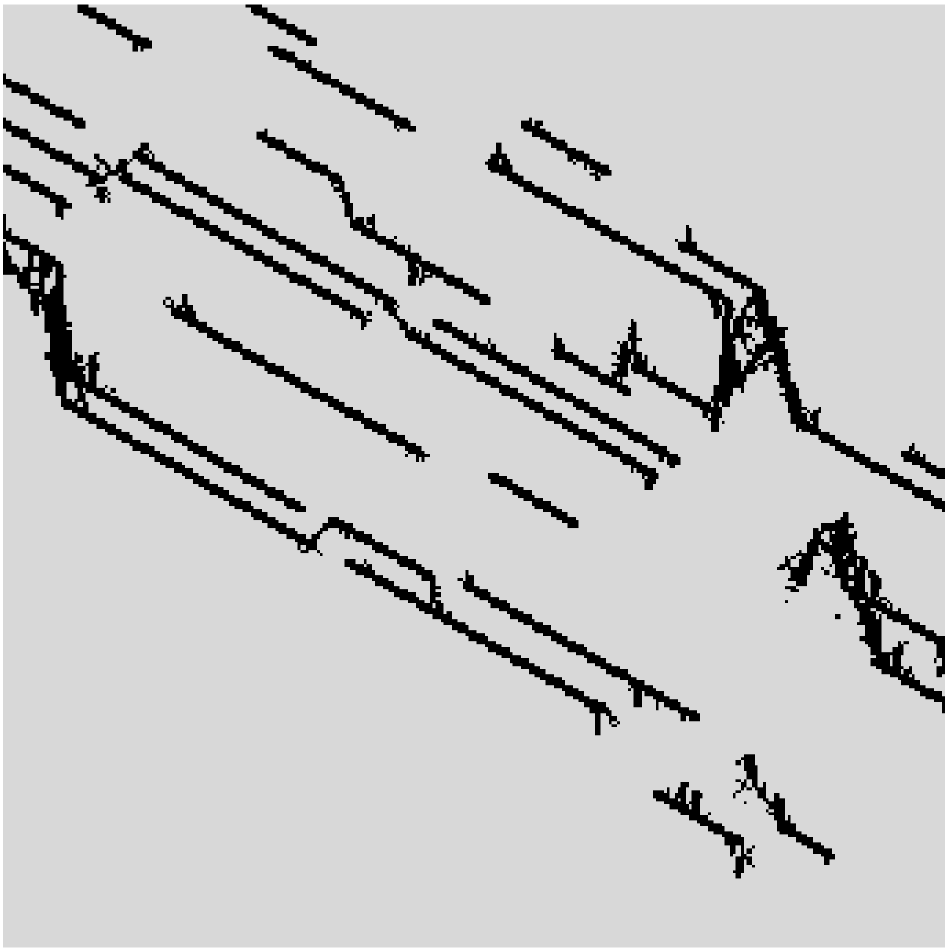

Figure 3.21 – An example of a single frame of a MOPEDZ simulation from more than 20 pre-existing joints illustrating the increased complexity which had to be displayed.

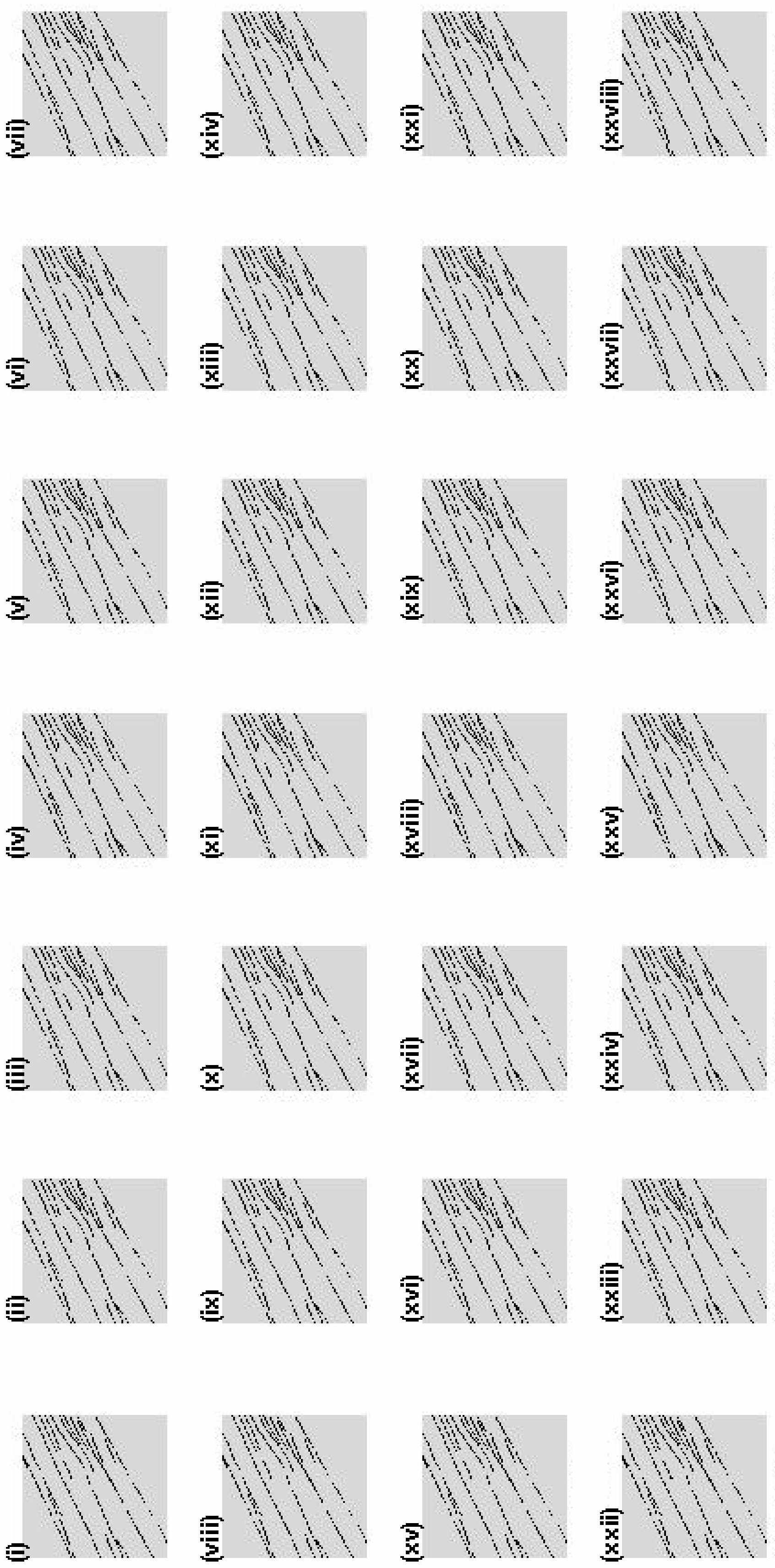

Figure 3.22 - Example showing the first 28 frames from a simulation consisting of 350 steps, this illustrates how difficult it is to see all of the detail of the fracture pattern and why all 350 frames can not be presented as one image.

In the examples shown so far only fracturing in a single rock type has been simulated with the fracture being represented by black squares and host rock by grey. The development of MOPEDZ included the ability to simulate fracture development in multiple rock types, when this was the case the plots had to be generated in colour (Figure 3.23).

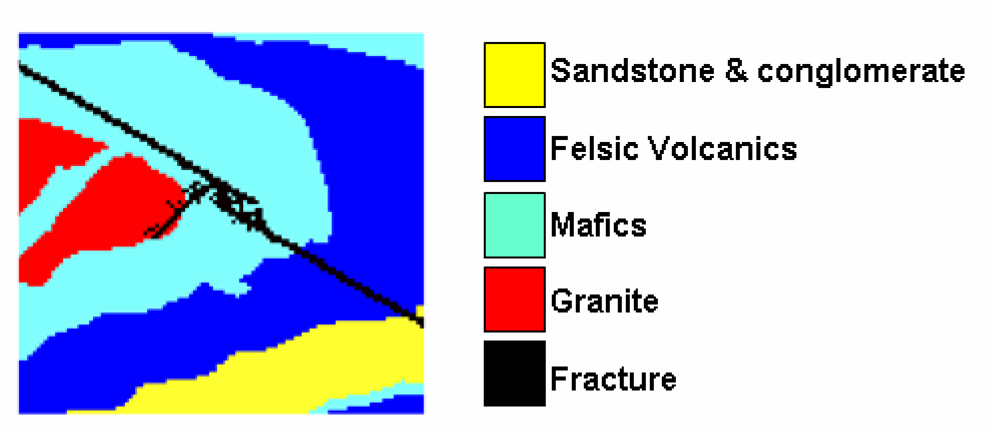

Figure 3.23 – Example of colour image generated when more than one rock type was simulated.

3.7 Summary

The MOPEDZ code is based on the standard theories of mechanical modelling using a combined Mohr-Coulomb and tensile failure criteria. The code has been modified to increase its efficiency and allow larger, more realistic simulations to be carried out. All of the following simulations presented in this thesis were carried out using the modified MOPEDZ code (detailed in section 3.5). These modifications allowed the heterogeneity of the pre-existing features to be increased (Chapter 4) it also allowed the heterogeneity of the host rock to be increased, including simulating fractures through different rock types (Chapter 5).

The simulations presented in Chapters 4 and 5 were based on field data collected from natural exposures and with the exception of the ignimbrite deposits presented in Chapter 5, the mode of failure in the field sites examined suggested that a low stress ratio ($\sigma_1 \approx 2\sigma_3$) is most appropriate, hence all simulations presented (with the exception of the ignimbrite simulations) were conducted with a low stress ratio.

The data presented in the following chapters is in many forms including:

- Damage plots
- Colour damage plots
- Strain maps
- Stress maps
- Videos

as detailed in section 3.6.

4 Modelling fault zone evolution from many pre-existing features.

In this chapter of the thesis I present the first numerical simulations of the temporal and spatial evolution of fault linkage structures from more than 20 pre-existing joints, the initial positions of which are based on field observation. It is shown that both the constantly evolving geometry and local stress field within this network of joints contribute to the resulting fracture pattern. The locations of the final fractures are in turn affected by the heterogeneity of the initial joint pattern, including initial joint length, separation, overlap, under-lap, spacing, and orientation to σ_1. Markedly different fault-zone-trace geometries are predicted when the joints are at different angles to the maximum compressive far-field stress ranging from evolving smooth linear structures to complex ‘stepped’ fault-zone trace geometries.

4.1 Increasing the heterogeneity of the pre-existing structures.

For MOPEDZ to become a realistic tool which could ultimately aid in increasing the accuracy of fluid flow models it had to be able to simulate large natural exposures where the pre-existing features from which faults often nucleate show a high degree of heterogeneity. By choosing a natural exposure to base the simulation on, the pre-existing structures were of varying sizes, lengths, orientations to σ_1 and notably were frequently not straight features (there were often slightly curved) in addition to this there was a change in the density of the pre-existing structures.

4.2 Choosing a Natural Exposure

The researchers who have developed conceptual models for fault growth through linkage of pre-existing structures have usually done so whilst examining mapped exposures [*Martel*, 1990; *Myers and Aydin*, 2004; *Flodin and Aydin,* 2004]. The granite bodies in the Sierra Nevada offer excellent exposures for this work as recent glacial activity and lack of extensive vegetation offer a well exposed outcrop, Figure 4.1.

Figure 4.1 - An exposure of the Lake Edison granodiorite in the Bear Creek region in the Sierra Nevada, California, UTM coordinates are: 0333075 4136569, mapped by J. Kirkpatrick, University of Glasgow. This was the exposure chosen for the MOPEDZ simulations presented in this chapter. Map of this site is shown in Figure 3.8c, a section of which is reproduced in Figure 4.2.

The distribution of the pre-existing joints for the following MOPEDZ simulations are based on part of an exposure of the Lake Edison granodiorite in the Mount Abbot Quadrangle in the central Sierra Nevada, California (Figure 4.21a). The damage zones at this and near-by locations consist of joints and minor faults [*Martel,* 1990; *Evans et al,.* 2000; *Kirkpatrick* et al., 2008]. These faults are thought to have developed through slip along a population of joints [*Segall and Pollard*, 1983]. These joints were most likely formed during the cooling of the plutons [*Bergbauer and Martel*, 1999].

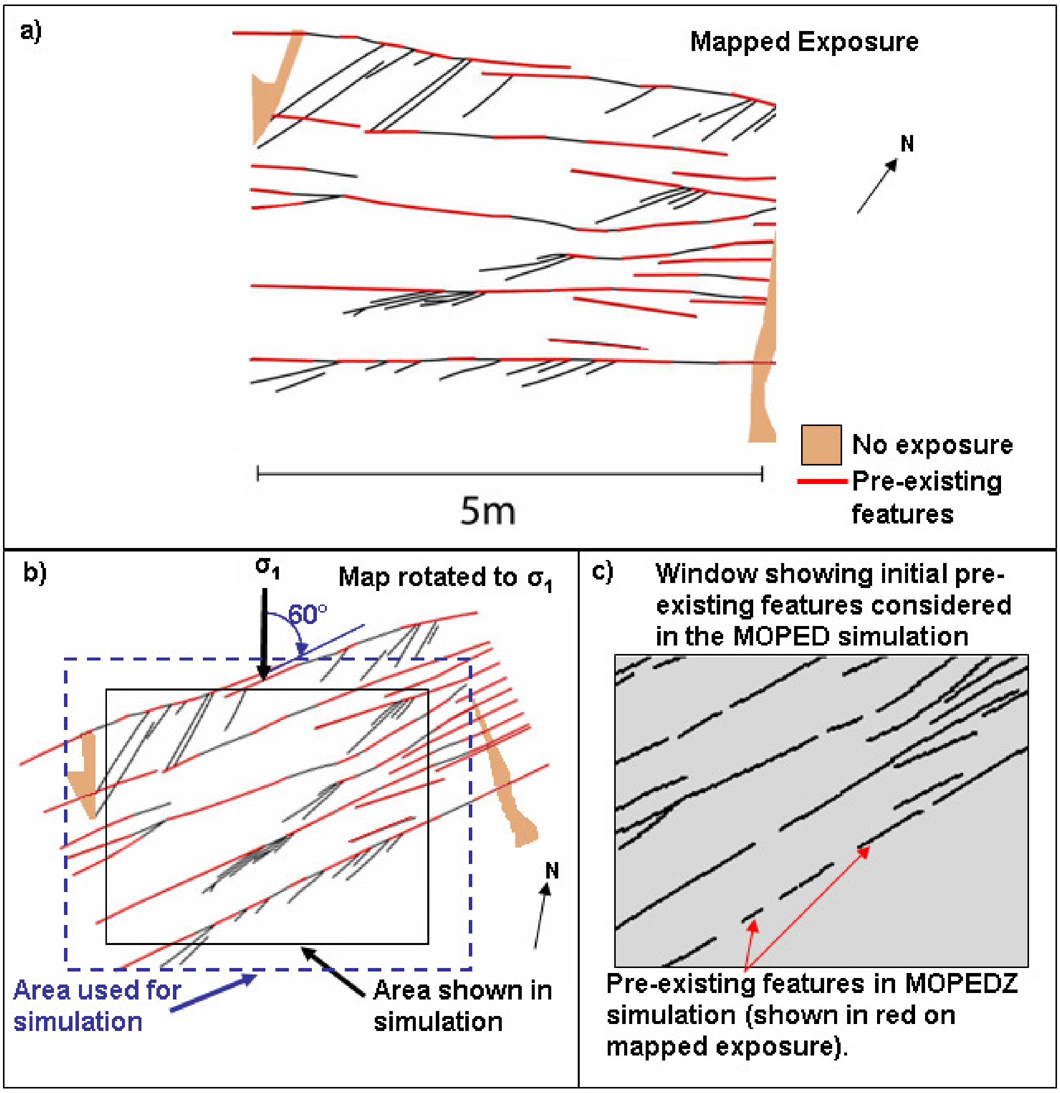

Figure 4.2 a) Small section from map shown in Figure 3.8c. b) Mapped joints oriented at 60° to the maximum principal stress (σ_1) (model requires σ_1 to be parallel to the y axis), c) Finite-element mesh containing initial pre-existing joints (n.b. the pixelated nature of the pre-existing joints is a product of the model). [*Moir et al.,* 2010]

4.3 Implementing MOPEDZ simulations based on the Natural Exposure

From the chosen geographical location field observations were used to approximate the sections of the small faults that may have comprised the original joints (before some joints were reactivated). Un-reactivated joints were identified as fractures that exhibit zero shear offset (through observations of aplite dykes or mafic enclaves) and lack any association with wing cracks. The locations of re-activated joints were then defined as those portions of the small faults that have similar trace orientations (within 10º) to the un-reactivated joints. The initial joint population input into the following MOPEDZ simulations includes both the un-reactivated and reactivated joints. The mapping of this field site, including observations of possible shear indicators, was carried out by J. Kirkpatrick from the University of Glasgow.

Figure 4.2a shows (in red) the locations of both the unreactivated and reactivated joints, as derived from the field data, for input to the MOPEDZ simulations. Prior to each simulation, this joint map is rotated such that the mean direction of the initial joints is at the desired angle to σ_1 (Figures 4.2b and 4.2c). The mode of failure in this field site was predominately in shear, as stated in Chapter 3 this mode of failure suggests that a low stress ratio ($\sigma_1 \approx 2\sigma_3$) is most appropriate, hence all simulations presented in this chapter were conducted with a low stress ratio. For the simulations with >20 joints to remove the effect of the boundary, results are displayed and discussed only for an internal area in the centre of the finite-element mesh, the edges of which are defined in Figure 4.2b and then in more detail in Figure 4.3

Small-scale simulations are also presented within this chapter to investigate behaviour at specific locations within the larger mesh shown in Figure 4.2c. These smaller scale simulations display results over the whole model domain (i.e. no internal window is taken). In each case presented below, initial damage predictions for the small mesh were compared with those within the larger mesh to confirm that predicted structures were similar, and hence that boundary effects were not having a substantial effect on model results.

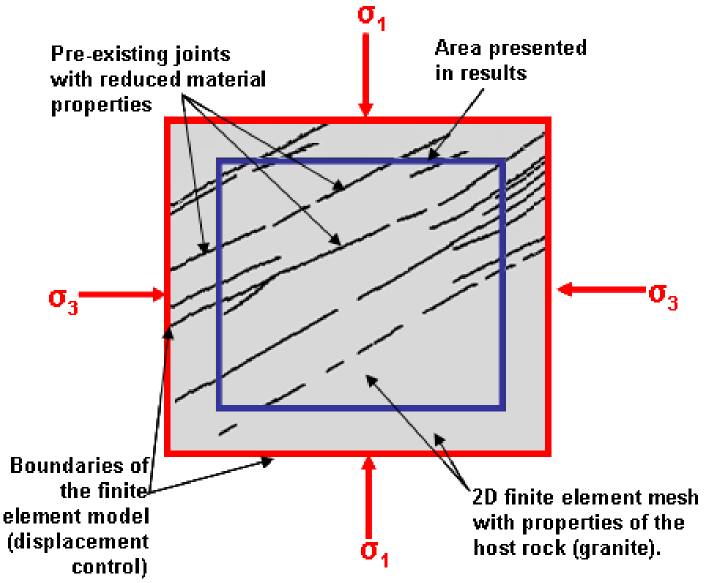

Figure 4.3: Typical initial setup showing the orientation of σ_1 and σ_3 (simulated far-field stress). Gray area is host rock, black is host rock containing joints (n.b. the pixellated nature of the pre-existing joints is a product of the model). The model boundaries (red) are under displacement control, following the initial failure only the top and bottom boundaries are displaced. To avoid consideration of structures generated at the boundary in the large simulations, only the central window (within the blue box) was presented in the results. For all small simulations no window was taken and all results within the red model boundaries are presented. The number of mesh elements varies from 6400 to 136,500 depending on the size of the simulation. [*Moir et al.,* 2010]

The remainder of this chapter describes simulations of fault zone development starting from all or part of the initial joint pattern shown in Figure 4.2. The purpose of these simulations is not to reproduce the detailed fault-trace geometries observed in the field (since the actual locations of original joints are not known with certainty) but to investigate the conditions that may promote differing styles of fault-zone development.

4.4 Results of MOPEDZ simulations

The spatial and temporal evolution of the fracture development and linkage predicted by MOPEDZ, for the joint pattern in Figure 4.2c, is shown in Figure 4.4 as a damage plot. The initial joints are at approximately 60° to σ_1 (Figure 4.4(i)). At first wing cracks begin to develop on some but not all joints (Figure 4.4(ii)). The orientation of the propagating wing cracks are similar to those predicted for the isolated joint pairs in Figure 3.15, for ease of comparison the relevant section of Figure 3.15 illustrating results for a low stress ratio regime are reproduced here in Figure 4.5. As the simulation continues (Figure 4.4(iii) to Figure 4.4(vi)) several types of linkage structures are observed which are similar to those in Figure 4.5. Note that only six frames are shown from a simulation consisting of 350 steps, (Appendix A contains a video of the full simulation).

For locations A through to D on Figure 4.4 predictions are similar to those using pairs of joints (Figure 4.5). At Location A, the linking structure is similar to that for an overlapping pair of joints in an extensional orientation. At

Location B the structure is similar to that for under-lapping joints in a contractional geometry (the joints under-lap by a single mesh element). At Location C the structure is the same as that for under-lapping joints in an extensional geometry. At Location D stepover geometries for both overlapping extensional joints and under-lapping contractional joints are represented, the predicted linkage structure is similar to that for overlapping joints in an extensional orientation.

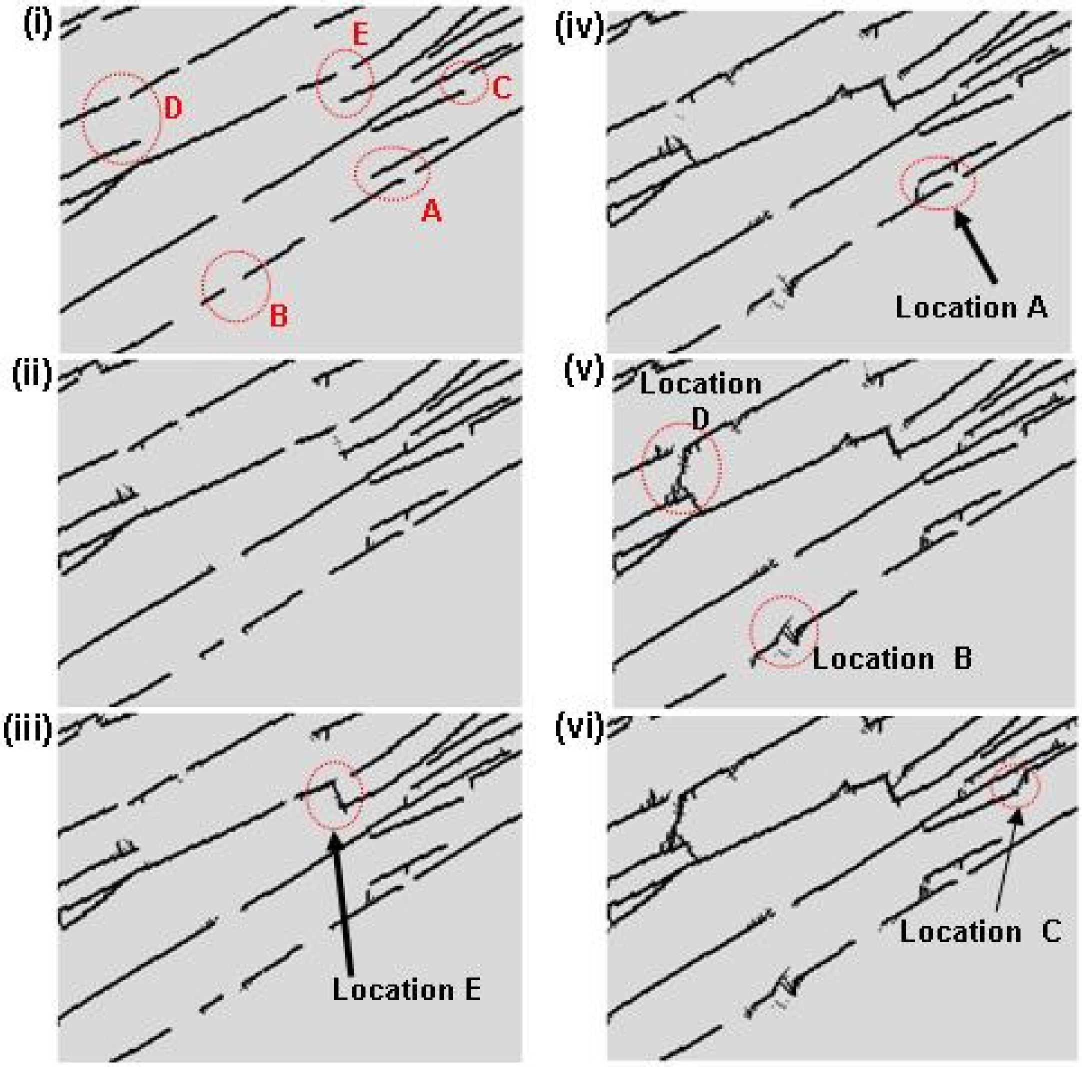

Figure 4.4 - Damage plot showing six frames from a simulation consisting of 350 steps which illustrate the temporal evolution of the linking fractures predicted by MOPEDZ from (i) the initial joints through to (vi) the final structure (finite-element mesh 390 x 350). The joints are oriented at approximately 60° to σ_1. Linkages at locations A are in a different orientation to the rest of the simulation. At location B overlapping joints in an extensional geometry link in a similar way as those in Figure 4.5c. At location C under-lapping joints in a contractional geometry link in a similar way as those shown in Figure 4.5b. At location D two closely spaced joints in a contractional geometry link with a third more distant joint which is in an extensional geometry. At location E joints under-lapping and in an extensional geometry link in a similar way as those shown in Figure 4.5a. All slipped joints are left lateral.

At Location E, however, the linkage structure that develops is different to that predicted for an isolated pair of under-lapping contractional joints (Figure 4.5b). At E, initial failure occurs in the host rock between the two joints as opposed to propagating from the joint tips. Because processing time for the large simulation (<20 joints) was 5-6 days, a small (6400 element mesh) simulation was conducted to investigate local behaviour at location E using three joints in the same relative positions; both the physical size represented by each finite element and the boundary conditions (progressive displacement of the σ_1 boundaries starting from an initial value of $\sigma_1 = 2\sigma_3$) remained the same as that for the large simulation in Figure 4.4.

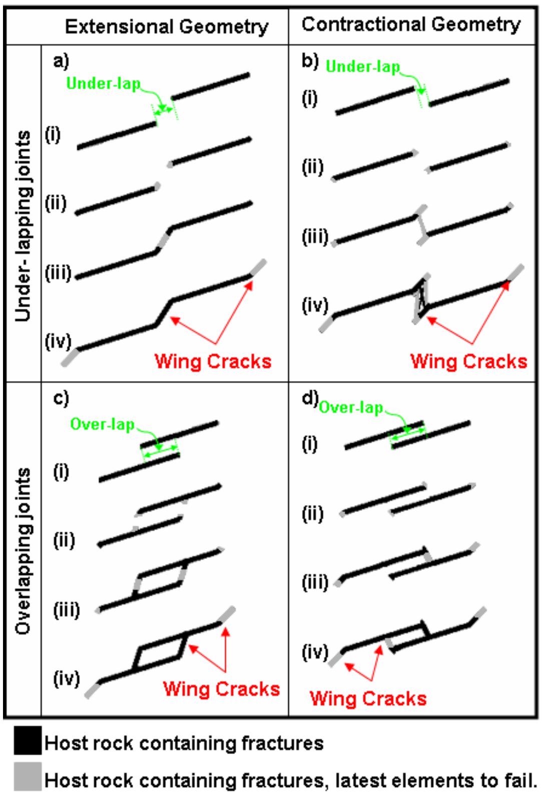

Figure 4.5 - **Cartoon showing the evolution of restraining and releasing bends for a pair of overlapping and under-lapping pre-existing joints with either contractional or extensional relationship in a low stress ratio. (i) is the initial orientation of the joints, and sequences (ii) to (iv) show evolution of the predicted structure. All slipped joints are left lateral. (section of Figure 3.15)**

Results of the simulation using the smaller mesh at location E are presented in Figure 4.6. The stress field (Figure 4.6a) shows that the *relative* position of the pre-existing joints facilitates interaction of the compressional quadrants of the two joints (j_1 and j_3), which results in linkage due to shear failure. Note that stress plots are produced within COMSOL which considers compression to be negative, i.e. Red colour indicates extension and blue compression. In Figure 4.6 joints j_1 and j_3 shown in Figure 4.6b overlap by 38mm. Further simulations showed that if the tip of joint j_3 was adjusted (by at least 38 mm either way) either to clearly over- or under-lap j_1, the linkage geometries obtained were once again similar to those expected for over- or under-lapping pairs of contractional joints (Figure 4.5b).

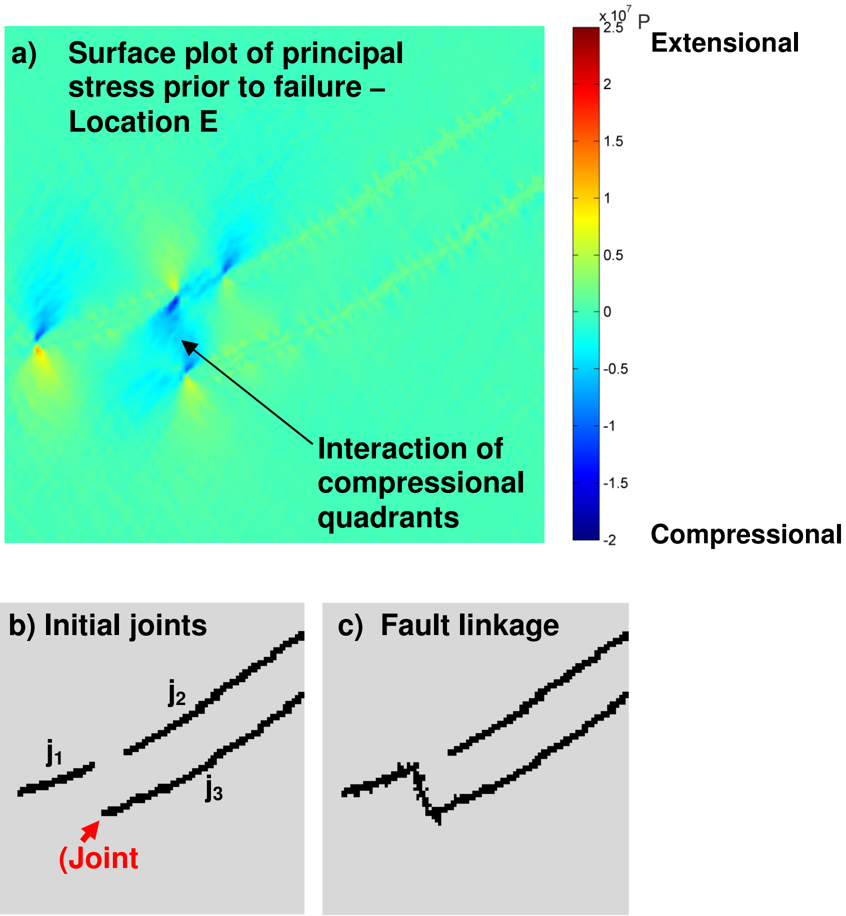

Figure 4.6 - Small simulation (80x80 finite-element mesh) with the joints in the same orientation as Location E. a) Surface plot of the principal stress prior to failure showing interaction of the compressional quadrants of both joints. Note that this plot was produced within COMSOL which considers compression to be negative, i.e. Red colour indicates extension and blue compression. b) Initial joint pattern entered into MOPEDZ (overlap between j_1 and j_3 of 38mm). c) Damage plot of the final structure obtained.

The three joints circled at Location A (Figure 4.4(i)) form two stepovers. The left stepover is extensional and the right stepover is contractional. The damage evolution (Figure 4.7a) and strain evolution (Figure 4.7b) were investigated in more detail using a small-scale simulation (6400 elements) with the joints in the same relative locations. Initially, the pair of joints on the left behaves as the extensional geometry in Figure 4.5c. However, as the fracture propagating from the middle of the upper joint lengthens, it interacts with the joint on the right of the figure, changing its orientation and eventually resulting in linkage of the pair of joints on the right that are in a contractional geometry (Figure 4.5d).

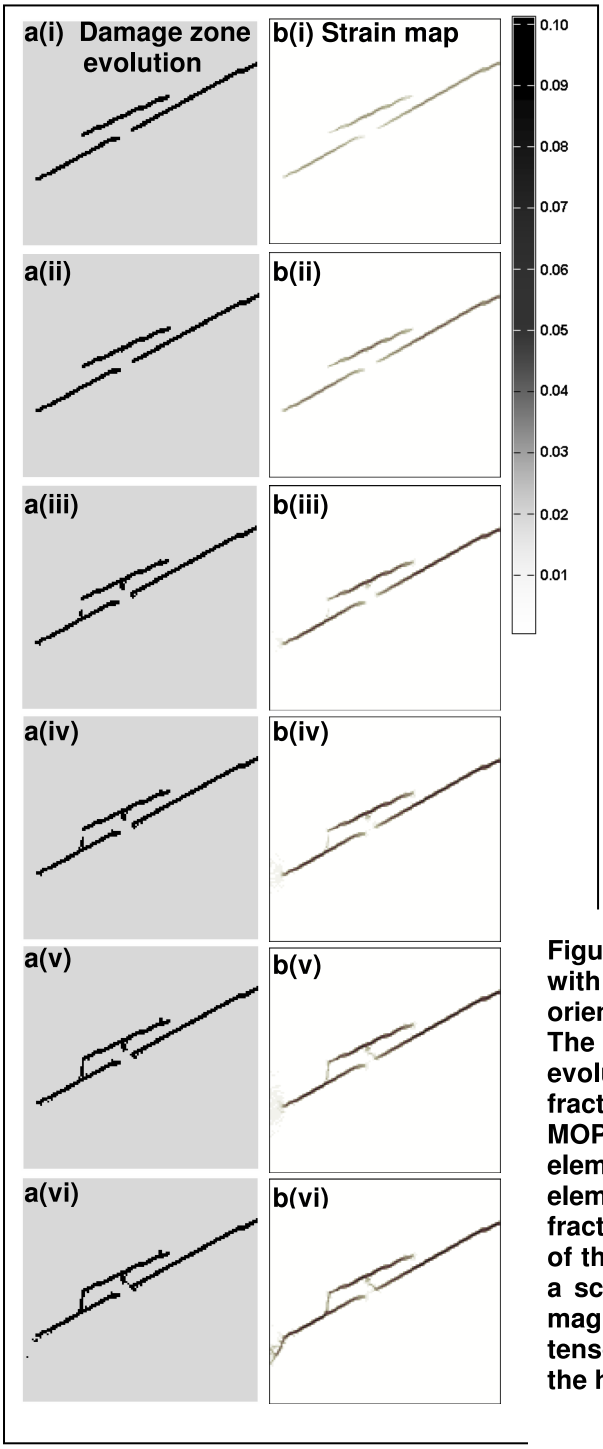

Figure 4.7 - Small simulation with joints in the same orientation as Location A. a) The spatial and temporal evolution of the linking fractures predicted by MOPEDZ; black represents elements of the of the finite-element mesh which contains fractures. b) Plots of the norm of the strain tensor which give a scalar representation of the magnitude of the strain tensors; the darker the colour the higher the strain.

Location B (Figure 4.4) evolves a linkage structure similar to that predicted in Figure 4.5b for under-lapping contractional geometries (the joints are displaced from being collinear by approximately 1 cm). At location D, however, despite the upper two joints being closer together than those at Location B and in a more pronounced under-lapping contractional geometry, a similar linkage structure does not develop. Instead, a wing crack propagates from the much more distant, extensionally-related joint below.

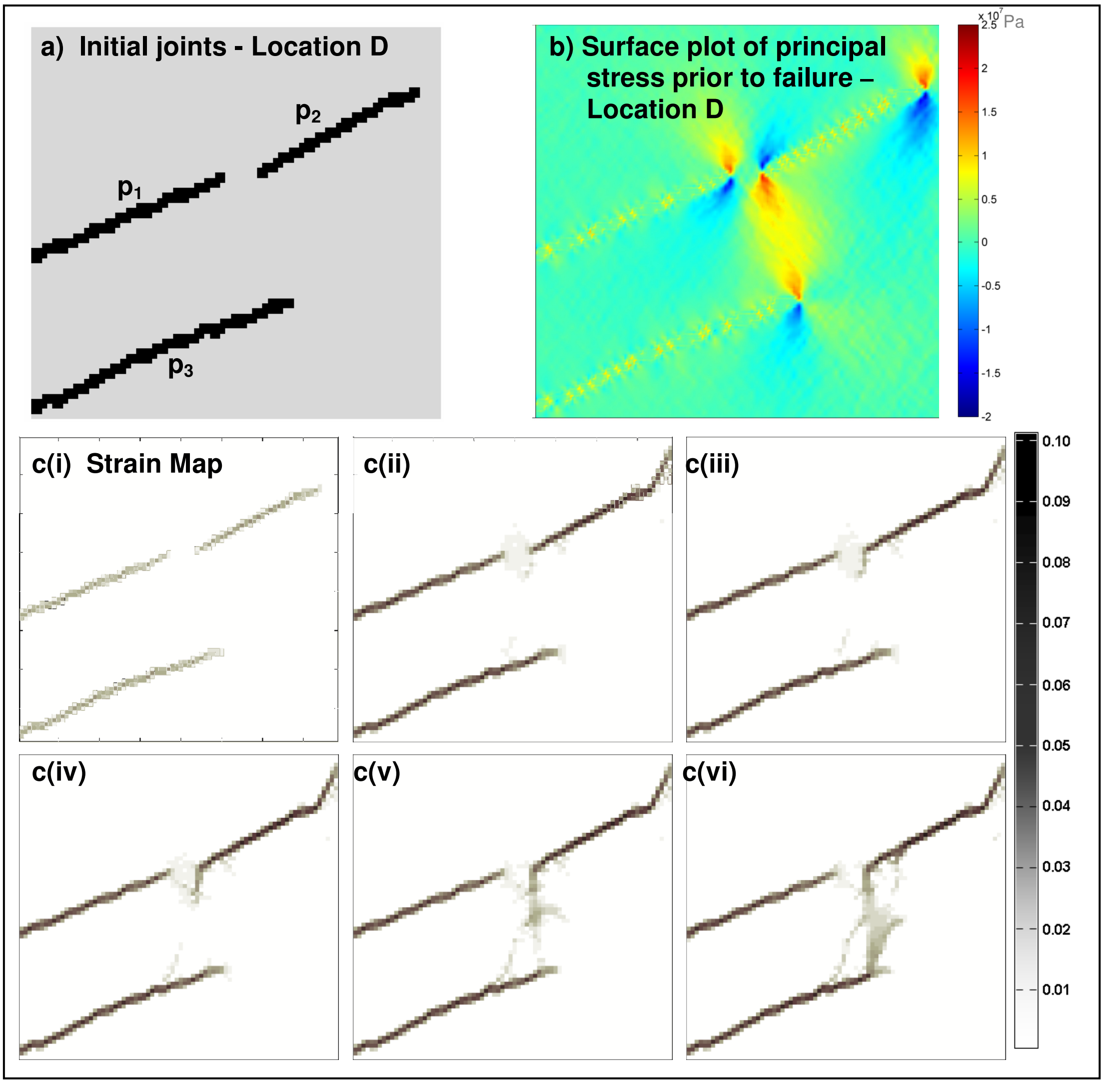

Figure 4.8 - **Small simulation with joints in the same orientation as at Location D. a) Initial orientation of joints for MOPEDZ simulation (80x80 finite-element mesh, the pixelated nature of the pre-existing joints is a product of the model). b) Surface plot of the principal stress immediately prior to first failure. c) Plots of the norm of the strain tensor (scalar representation of the magnitude of the strain tensors) illustrating the predicted evolution of the fractures.**

To illustrate the effect of neighbouring joints on the resulting fracture pattern, a small-scale simulation was performed for the three joints at location D. The initial joint configuration is shown in Figure 4.8a and the magnitude of σ_1 prior to failure is shown in Figure 4.8b. Comparison of Figure 4.8b with the stress fields which are predicted for each of the three joints if simulated separately (Figure 4.9) shows that having all three joints present reduces the magnitude and extent of the region of compressional stress surrounding the interacting tips, and increases the magnitude and extent of the tensional stress, most notably between joints p_2 and p_3.

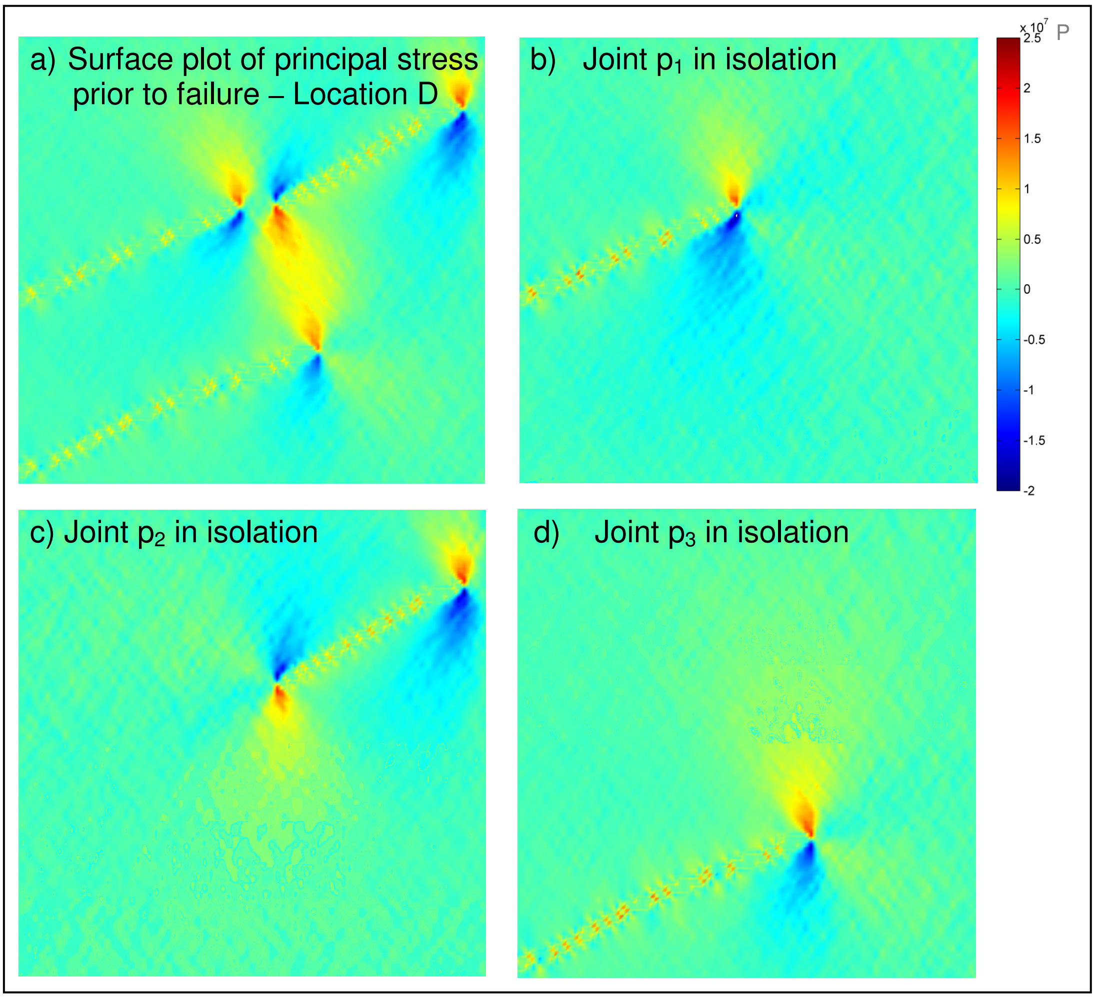

Figure 4.9- **Surface plot of the principal stress prior to failure for individual pre-existing structures in the same orientation as those at location D, Figure 4.4.**

This interaction of local stress fields around the fault tips explains the linkage structure that develops between the more distant extensional pair of joints, evident from the strain evolution (Figure 4.8c). The resulting fracture pattern is similar to that seen in a geometrically similar configuration of starter joints in *Segall and Pollard* [1980] (Figure 4.10, their Figure 12a).

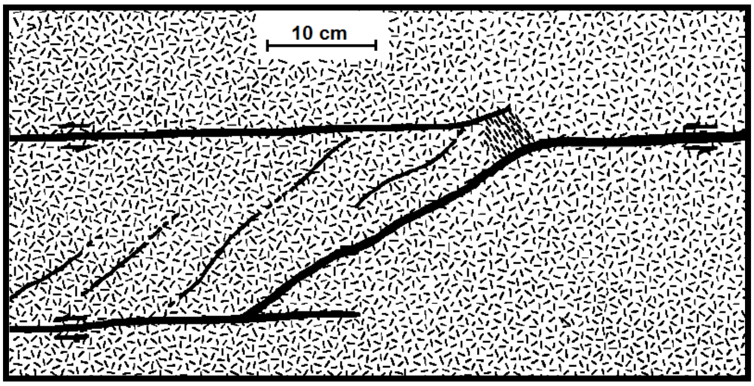

Figure 4.10 - Secondary fractures associated with left-lateral faults in the Sierra Nevada from *Segall and Pollard* [1980] (their Figure 12a).

From the above it is clear to see that the same geometric structures as predicted for isolated pairs of joints are still observed in the large network of joints. However, which pair of joints will link and which will remain in isolation is not obvious, this is well illustrated at location D.

The small simulation examined above for location D was explored in more depth to test the influence of joint length and proximity on determining which joints will link and which will not.

4.4.1 The influence of joint length on linkage

Based on field observations, the extent of the local stress perturbation associated with a fault has been related to its trace length (e.g. *Segall and Pollard*, [1980]). To explore the effect of joint length on evolving fault linkage, small scale simulations were performed adjusting the joint configuration at Location D. The lengths of the upper joints (p_1 and p_2) were increased, keeping the relative position of the adjacent joint tips constant (Figure 4.11). When the length of either one (Figure 4.11a) or both (Figure 4.11b) of the upper joints are doubled, joints p_1 and p_2 link in a manner similar to that for under-lapping contractional joint pairs. Previously, in Figure 4.8, linkage was between the extensional pair of joints p_2 and p_3. From these simulations it is apparent that the length of the joints does affect the extent of the local stress perturbation, and in these simulations has enhanced the likelihood of linkage between the upper two joints which have an under-lapping contractional geometry,

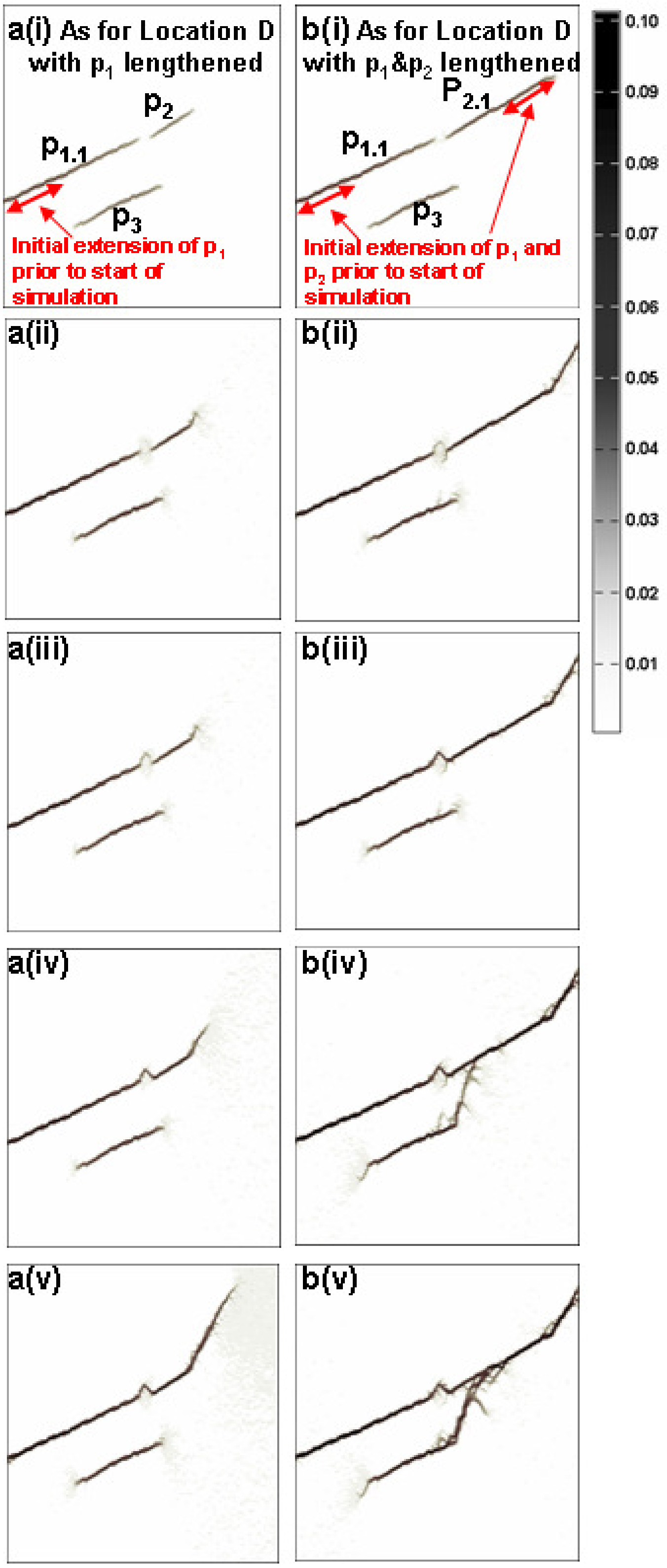

Figure 4.11 - Spatial and temporal evolution of strain predicted by MOPEDZ with pre-existing structures in the same relative positions as location D but with a) the initial length of p_1 doubled ($p_{1.1}$) and b) initial length of p_1 and p_2 were both doubled ($p_{1.1}$ and $p_{1.2}$ respectively). Note that wing cracks only develop on p_3 when the upper wing cracks reach the boundary; had it not done so the growth of wing cracks from p_3 would have been suppressed. (All faults are left lateral.).

4.4.2 Separation between joints

Small-scale simulations consisting of up to three joints were used to explore the effect of joint separation; this was investigated by increasing or decreasing the distance between joints in the y direction. The position of the lower joint (based on the configuration at location D) was adjusted until it was separated enough to allow the upper two (p_1 and p_2) to link (Figure 4.12a). The stress perturbations due to each joint were then explored by systematically removing each from the simulation (leaving only two joints in the simulation). Results for each remaining pair are shown in Figures 4.12b, 4.12c and 4.11d. The simulations predict varying joint linkage geometries from joints linking rapidly (Figure 4.12b) through joints that fail to link, but show an evolving structure within the linkage zone (Figure 4.12c) to joints which do not link (Figure 4.12d). Note that in this final simulation (Figure 4.12d) the wing crack which develops from p_3 does so at a different angle (40° from σ_1) than for the original simulation (24° from σ_1). The simulations illustrated in Figure 4.12 show that the proximity of neighbouring joints affects both the location and orientation of the linkage structures that develop.

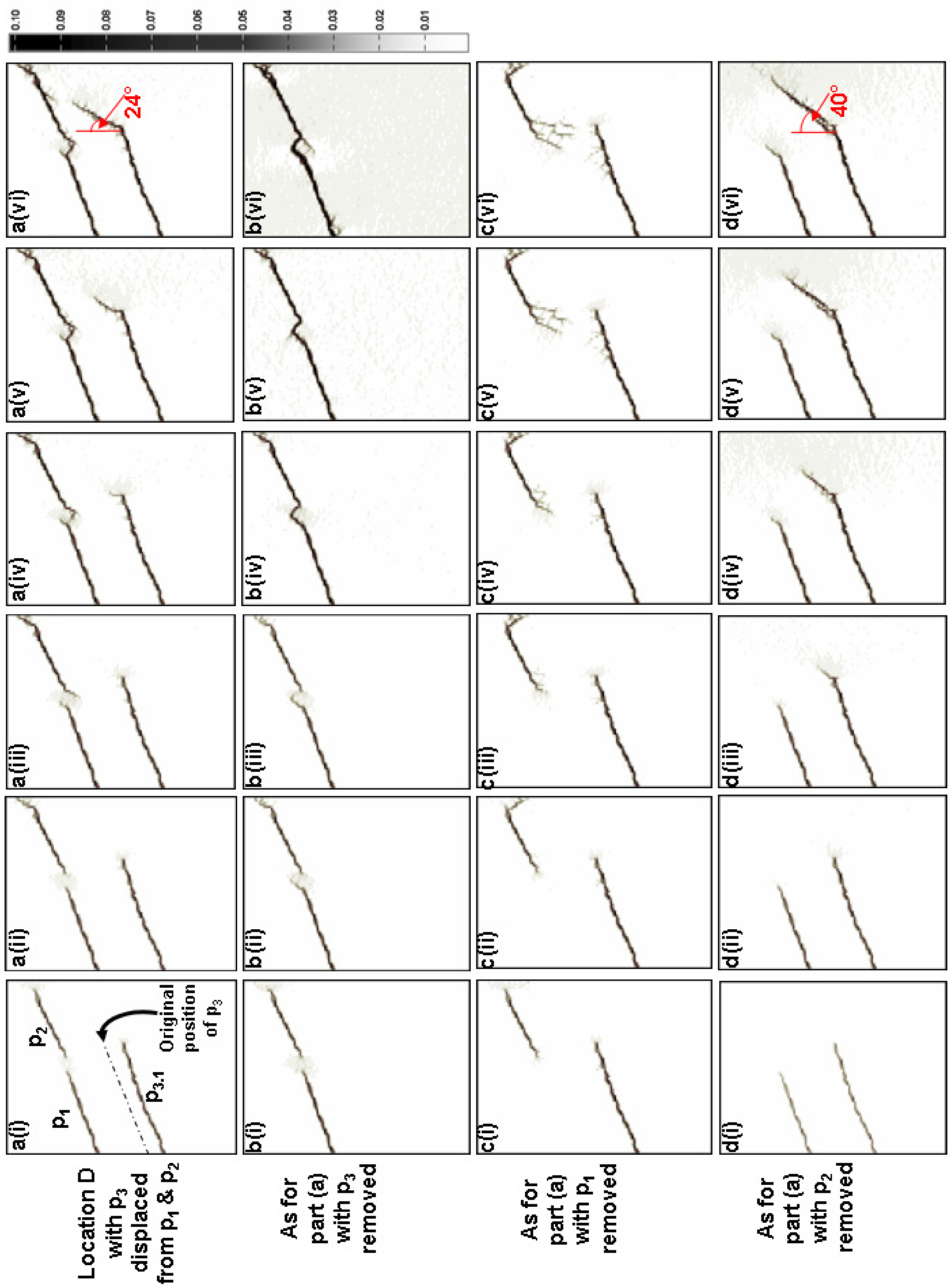

Figure 4.12 - a) Spatial and temporal evolution of strain predicted by MOPEDZ with joints in the same relative positions as location D but with p_3 displaced away from the upper two joints. Temporal evolution of strain predicted by MOPEDZ b) if p_3 is removed, c) if p_1 is removed and d) if p_2 is removed. Note that the angle of the wing crack propagating from the p_3 is 24° for simulation a) but is 40° for simulation d).

Figure 4.13 explores the effect of joint-parallel separation. When p_3 is adjusted such that in the initial configuration it is closer to p_1, (labelled as $p_{3.2}$ in Figure 4.13a) the linkage structure which evolves is more defined and typical of under-lapping extensional joints as illustrated in Figure 4.5.

Even with the reduced joint-parallel separation between joints 1 and 3, the presence of neighbouring joints still has an effect on the final damage structure which evolves; comparing Figure 4.13b and Figure 4.13d, it can be observed from Figure 4.13c that there is some growth on p_1 which is completely inhibited when p_2 is present within the simulation; however, the growth on p_1 is greatly reduced from the earlier simulation illustrated in Figure 4.12d where the two pre-existing joints were further apart.

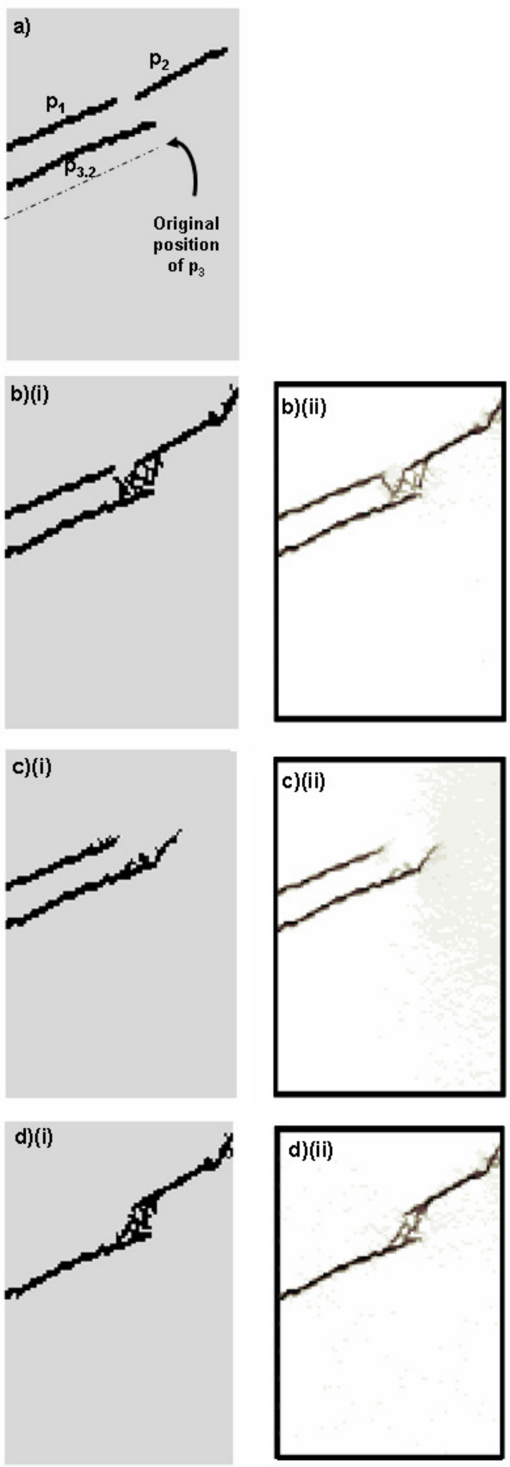

Figure 4.13 - a) Initial position of the pre-existing joints in the same relative positions as location D but with p_3 displaced towards the upper two joints, now $p_{3.2}$. b) Final linkage structure which evolves when all thee joints are present (i) damage plot and (ii) strain plot. c) Final structure when p_2 is removed from the simulation (i) damage plot and (ii) strain plot. d) Final structure when p_1 is removed from the simulation (i) damage plot and (ii) strain plot.

4.4.3 Exploring the effect of orientation of the regional stress field

Simulations of linkage from isolated pairs of joints in *Lunn et al.* [2008] showed that one of the key factors controlling the fault-zone geometry was the orientation of the joints to σ_1. In the case of joints at a low angle to σ_1 wing cracks were found to propagate back into the compressional quadrant, similar to structures observed in the field [*Vermilye and Scholz,* 1998]. To explore what effect the orientation of σ_1 can have on fault-zone evolution from a complex joint pattern, the joints in Figure 4.2 were rotated to an angle of approximately 30° to σ_1 (Figure 4.14(i)). The predicted evolution of linkage structures through time is shown in Figures 4.14(ii-vi); a visual comparison of Figure 4.14(vi) and Figure 4.4(vi) shows the final geometries to be very different. Critically, joint traces that were approximately co-linear now progressively link up along strike to form long smooth linear fault traces (e.g. Location B and D). Further, the few wing cracks that do evolve in Figure 4.14 only develop once neighbouring joints have linked to form through-going faults and propagate back into the compressional quadrant (e.g. Location A and F). The only exception to this is at Location C, (Figure 4.14(iv)) where an extensional stepover of the under-lapping joints develops.

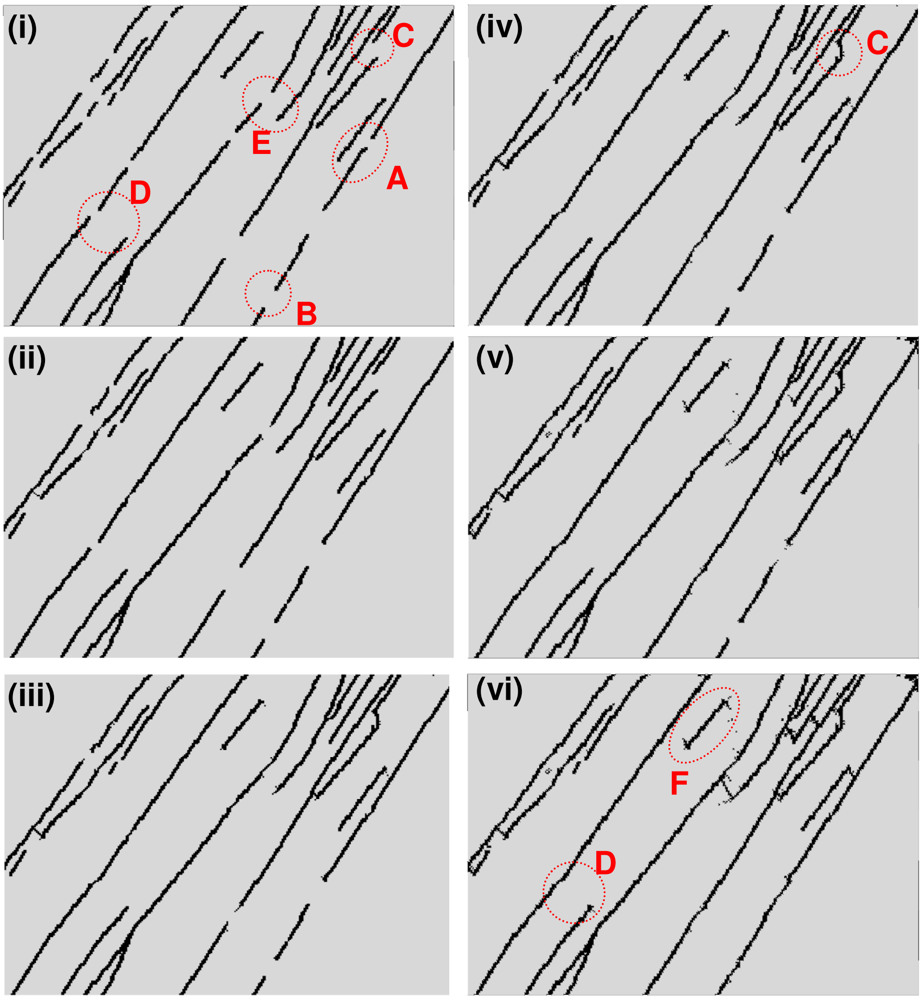

Figure 4.14 - Damage plot showing six frames from a simulation consisting of 350 steps which show the spatial and temporal evolution of the fractures predicted by MOPEDZ from (i) the initial joint pattern through to (vi) the final structure. The joints are oriented at 30° to $\sigma 1$. Locations A – E indicated on (i) correspond to those in Figure 4.4(i). Simulation was carried out with the same initial conditions as that shown in Figure 4.4. All faults are left lateral.

Three key observations are apparent from a comparison of the simulation results for pre-existing joints at 60° and 30° to σ_1:

- For the simulation at 60° to σ_1 (Figure 4.4), the linking wing cracks are at a much wider variety of angles (e.g. see locations B and D in Figure 4.4) than those at 30° to σ_1 (Figure 4.14).
- For the simulation at 60° to σ_1 (Figure 4.4) many joints develop multiple wing cracks at individual joint tips and linkage structures tend to exhibit more damage than those at 30° to σ_1 (e.g. compare location D in Figs. 4.4 and 4.14).
- With structures at 30° to σ_1, approximately 60% of the joints link along strike forming smooth linear features which span the model domain (Figure 4.14); these features do not form for the simulations at 60° to σ_1.

To further explore the effect of rotating the stress field, additional large scale simulations were carried for angles of σ_1 to the initial joint orientation of 45°, 53° and 80°. These simulations were conducted with the same initial boundary conditions as the simulations illustrated above, the final structures are shown for all angles in Figure 4.15.

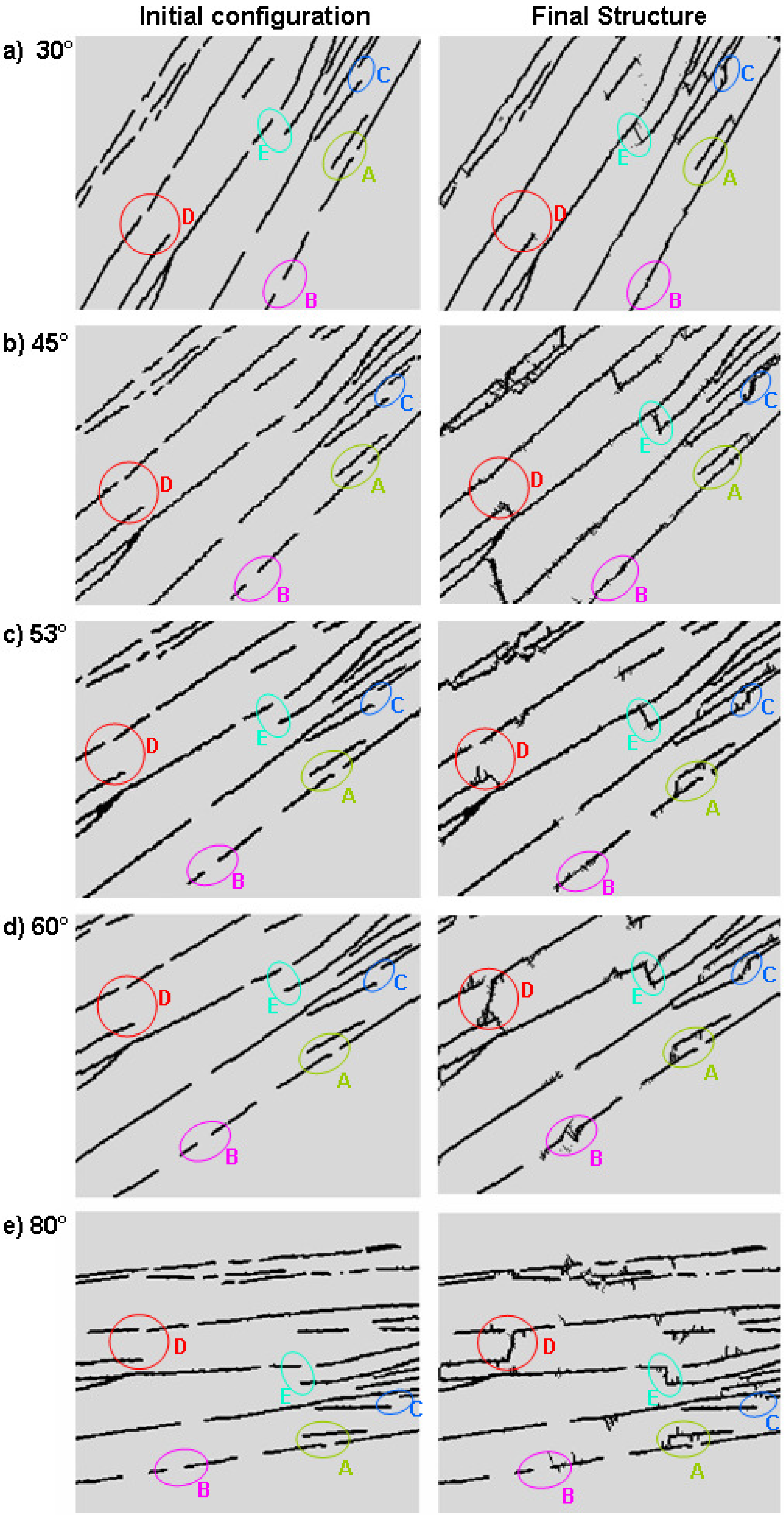

Figure 4.15 – Initial configuration and resulting final predicted damage plot with the joints at several orientations to the maximum compressive stress. a) Joints are at approximately 30° to σ_1, this is a repeat of initial and final frame of Figure 4.13. b) Joints are at 45° to σ_1. c) Joints are at 53° to σ_1. d) Joints are at approximately 60° to σ_1, this is a repeat of initial and final frame of Figure 4.3. e) Joints are at 80° to σ_1

At location A linkage structures develop between *parallel adjacent* joints when the rotation from σ_1 is 53° or higher. At orientations to σ_1 less than 53° the behaviour at A is completely different and *co-linear adjacent* joints link along strike. At location B (where there is no paraellel joint nearby) the co-linear along strike linkage typical of a low angle rotation to σ_1 develops for rotations less than 60°. At location C the under-lapping extensionally related joints always develop the structure illustrated in Figure 4.5a except for the final simulation where the joints are at 80° to σ_1. At location D the upper two joints link along strike when the rotation is at 30° and 45° however for higher rotations (60° and 80°) it is the more distant under-lapping extensionally related joints which develop a linkage structure, for the simulation at 53° linkage has not occurred but appears to be starting to develop between the extensionally related joints. At location E where the tips of the adjacent joints are aligned to allow interaction of the compressional quadrant of the local stress field associated with each joint (Figure 4.7) the linkage between these two joints always occurs at all rotations.

Comparing the final damage plots shown in Figure 4.15, for joints at 45° to σ_1 the general structures are the same as those predicted when the joints are at 30° where linkage is typically along strike. At 53° there is also significant along strike linkage creating pathways which span the model domain, however, development of some linkage features between adjacent (rather than along strike) joints occurs at some locations (see locations A and C). The linkage of adjacent (parallel) as opposed to co-linear joints is typical of most of the structures observed when the joints are at 60° to σ_1. The simulation at 80° shows the development of single and multiple wing cracks at a wide variety of angles only a few of which have linked adjacent joints.

4.5 Summary

The simulations show three key findings: 1) Local spatial and temporal variations in the stress field have a significant effect on the location, orientation and timing of wing crack development, resulting in significantly different patterns than those predicted from consideration of single fractures or pairs of fractures. 2) A significant difference in resulting fault-zone geometry is predicted when σ_1 is oriented at a low angle (45° or less) with respect to the initial joint pattern (Figures 4.14 and 4.15) compared to simulations with σ_1 oriented at a high angle 60° or greater (Figures 4.4 and 4.15). 3) The spatial distribution (lengths, separation, overlap, under-lap, spacing) of the original joints is a key control on the predicted locations, orientations and timing of wing-crack development.

4.5.1 Local variations in the stress field

The simulations focus on fault formation via linkage of pre-existing original joints and show that the proximity of neighbouring joints, and their effect on the local stress field, affects both the location and orientation of the linkage structures that develop. The large-scale simulations represent an area approximately 4.5m wide interestingly, similar results are predicted if the model domain represents a larger physical size (e.g. several kilometres wide), where the initial features are 20 en-echelon pre-existing faults (the only difference being the physical size represented by each element in the finite-element mesh and the load required to create the same number of damaged elements).

Currently researchers in many fields use predictions of static stress distribution around an existing fault network to predict the locations and orientations of likely fracture zones [*Maerten et al., 2002; Micklethwaite and Cox, 2004*]. Our simulations demonstrate that the locations of active fracture zones associated with faulting are likely to be critically affected by the constantly evolving local stress field as the fracture network develops. Simulations suggest that, in some cases, fracture zones will not begin to develop until adjacent through-going faults have fully formed. Further, the orientations of these fractures will be influenced by the evolving geometry and proximity of neighbouring features within the network. Hence, predictions of the location and orientation of fracture zones, such as those by *Maerten et al.* [2002] and *Micklethwaite and Cox* [2004] may be improved by incorporating simulation of the constantly evolving local stress.

4.5.2 Orientation of the maximum compressive far-field stress

For a simulated σ_1 at a high angle to the original joints (e.g. Figure 4.4), faults are principally formed by slip on pre-existing joints which then grow in length as wing cracks evolve and link originally discontinuous adjacent (parallel) fault traces, resulting in a ‘stepped’ fault-zone geometry. A comparison of these results with Figure 4.16 (repeat of Figure 3.7) shows them to be similar to the complex fault-zone geometry in Figure 4.16b [*Martel,* 1990]; a large number of wing cracks and linkage structures are present, at a variety of angles, with few through-going features. Our simulations suggest that the faults from the Waterfall region of the Sierra Nevada (Figure 4.16b) were formed under σ_1 at approximately 60° to the original joints. This angle to σ_1 differs from the 25°-30° derived for the same field site using Linear Elastic Fracture Mechanics (LEFM) by *Segall and Pollard*, [1983] and *Martel,* [1997]; this may be due to the assumptions inherent in LEFM where failure is inferred from the steady-state stress distribution local to a single infinitely thin fracture within an infinite elastic domain.

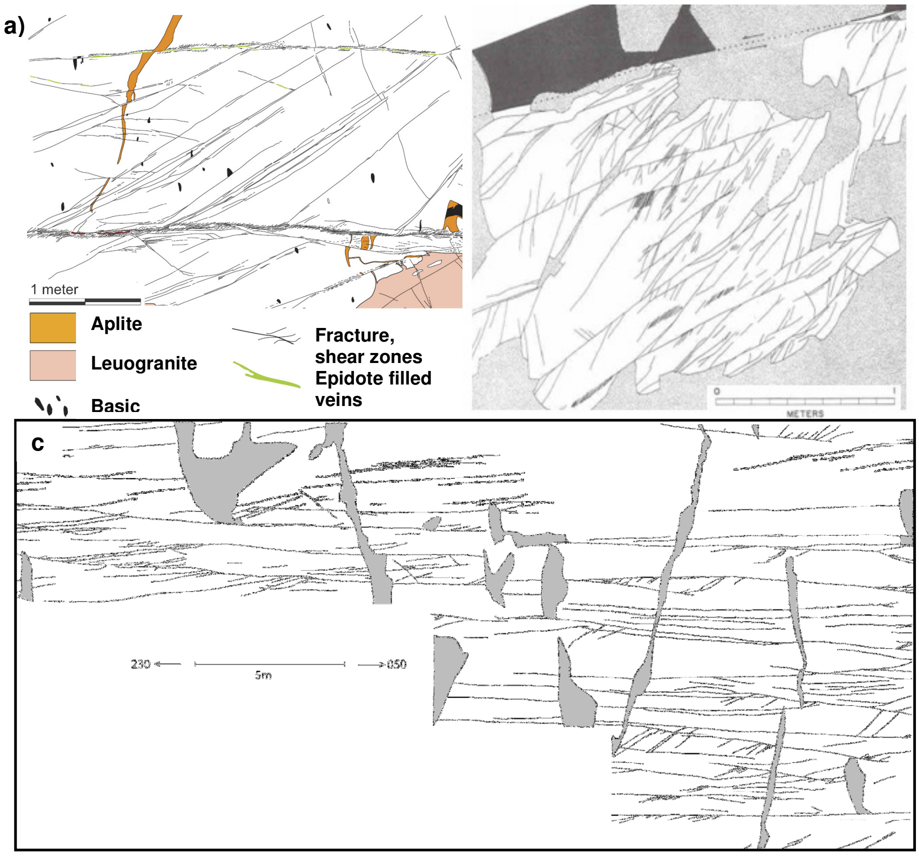

Figure 4.16 - Repeat of Figure 3.7 - Field examples of mapped sections from fault zones a) A segment of the outcrop map from NE of Neves lake in the Italian Alps showing a section of fault zone with smooth planar features [*Pennacchioni and Mancktelow*, 2007] b) A segment of the outcrop map from the Waterfall region in the Sierra Nevada, California [*Martel*, 1990]. c) Map of fractures in an exposure of the Lake Edison granodiorite in the Bear Creek region in the Sierra Nevada, California, UTM coordinates are: 0333075 4136569, mapped by J. Kirkpatrick, University of Glasgow. [*Moir et al.*, 2010]

For σ_1 at a low angle (45° or less) to the original joints, smooth linear faults are predicted in the simulations with a small number of linking fractures propagating back into the compressional quadrant. A comparison of Figure 4.13 with the field observations shows the predicted fault geometry to be similar to that in Figure 4.16a [*Pennacchioni and Mancktelow*, 2007] for the small NE-striking faults (these are labelled as fractures but offset the aplite). We suggest that these NE-striking faults may have formed by linkage of small joints and fractures when σ_1 was oriented approximately NNE.

Smooth co-linear fault traces such as those in Figure 4.16a are commonly observed in field exposures. However, they are not generally interpreted from field data as having evolved from linkage of co-linear joint traces, but instead are mapped as long, small offset faults. In many cases this is likely to be because it is difficult from field data alone to distinguish whether individual along-strike sections of a fault originated as co-linear joints or formed through along-strike linkage. Multiple offset markers could be useful because sites of linkage commonly remain as displacement minima along a fault that develops by segment linkage (e.g. *Burgmann et al.,* [1994]). However, the aplite dykes used as offset markers to determine shear direction are rare in both of the field areas in Figure 4.16. It is possible that the fault gouge within a slipped joint will have a different mineralogy, grain size distribution or fabric than that along a linkage fracture.

The faults from the Bear Creek region of the Sierra Nevada (Figure 4.16c) are a combination of frequent through-going ‘smooth faults’ and multiple wing cracks (typical of more ‘stepped’ fault-zones). We suggest that at this location one or more rotations of σ_1 may have occurred during fault-zone evolution as discussed by *Segall and*

Pollard [1983]. Rotation of σ_1 may be caused by an actual change in the regional stress field or by more local evolution of the stress field during development of larger-scale structures (e.g. due to nearby linkage of faults at a scale one order of magnitude greater than those simulated here). Alternatively the orientation may be at an angle of around 53° to σ_1 (Figure 4.14c) where a combination of both fault zone morphologies are be predicted.

5 Exploring the effect of increasing the heterogeneity of the host rock

This chapter explores the effect of increasing fault zone heterogeneity on fault zone evolution. The research explores two fundamental questions:

(1) Does the general structure of the fault zone change when host rock heterogeneity is introduced within a single rock type? This question is addressed by re-examining the joint patterns presented in Chapter 4 but incorporating heterogeneity into the surrounding host rock with the material properties varying in a smooth manner.

(2) What happens to fault zone evolution when multiple, discrete rock types are present in a single simulation? This question is explored at two different scales. First, discrete variations in rock type are investigated on the scale of a few meters by examining fault growth in ignimbrite. Second, fault zone evolution through a lithological sequence is simulated on a scale of several kilometres.

5.1 Exploring the effect of heterogeneity within a single rock type

The simulations presented in Chapter 4 show that, in general, fault zone structures are determined by: the ratio of σ_1 to σ_3; the orientation of the pre-existing joints to $\sigma_{1;}$ and the initial relative positions of neighbouring joints, specifically, contractional vs. extensional geometries and overlapping vs. under-lapping joints. All these simulations used a homogeneous host rock.

In the field, it is clear that an individual host rock is not homogeneous. For example, sandstones can vary in grain size, degree of fracturing, number and orientation of deformation bands [*Guo et al.,* 2009]. A granite exposure may exhibit changes in mineralogy that will affect its mechanical properties. Such changes may be on a scale of a few centimeters (Figure 5.1) or several kilometers (Figure 5.2). *Glazner et al.,* [2004] suggest that such variation in granitic bodies is common at all scales and is a due to the method by which they are emplaced and/or sourced.

Figure 5.1 – Exposure of granite in Sierra Nevada showing patches of lighter and darker granite (photo taken by Zoe Shipton).

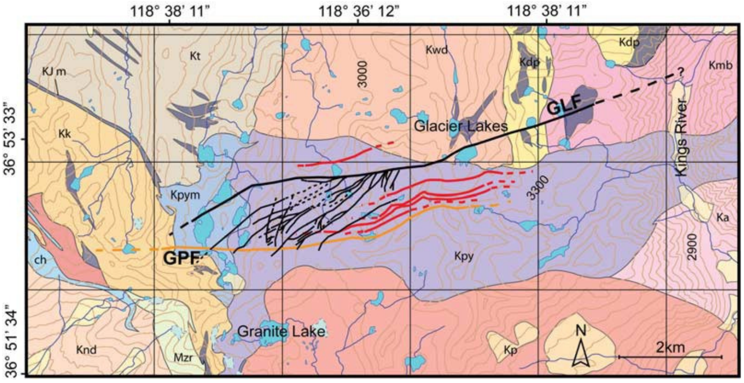

Figure 5.2 – **Each of the different granites in this field site are indicated by a different colour and the faults at the site cross different granite exposures [*Kirkpatrick et al.,* 2008].**

5.1.1 Increasing heterogeneity using a spatially correlated field

The following simulations explore the effect on fault evolution of mineralogical variations in the surrounding host rock. The most common approach to representing host rock heterogeneity is that of spatial statistics, whereby individual properties of the rock, such as strength or permeability, are described using a spatially correlated random field. This approach is standard for representing porosity and permeability within stochastic flow simulations in both the groundwater and petroleum industries [*Bruderer et al.,* 2004].

The simulations presented in this section use the same initial joint pattern as described in Chapter 4, with the inclusion of a spatially correlated random field (see example in Figure 5.3) to represent stronger and weaker ‘patches’ within the granite host rock. The average length of the initial joints for the joint pattern presented in Chapter 4 was approximately 60 pixels. Consequently, the average size of the ‘patches’ in the spatially correlated field was initially chosen to be the same (60 pixels) as this was considered to be the ‘worse case scenario’; if the heterogeneity was going to affect the evolution of the joint pattern this was the scale at which it was most likely to do so.

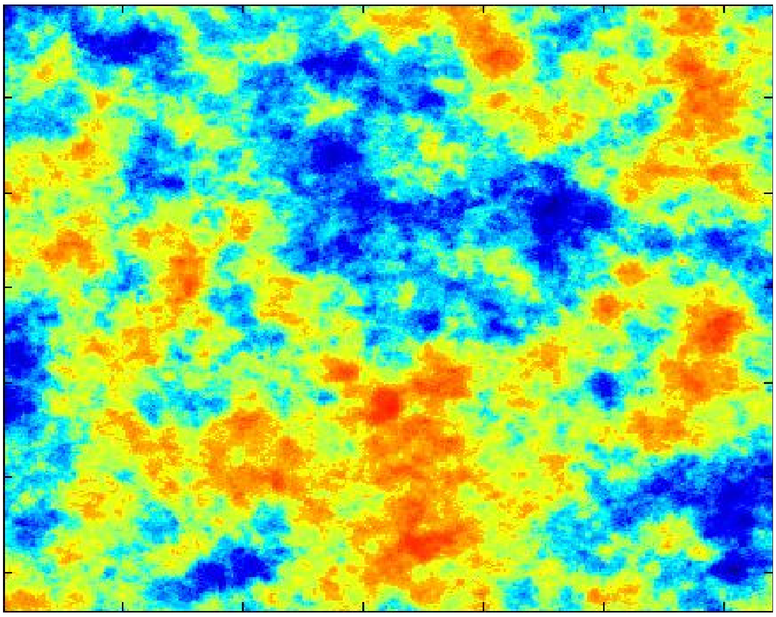

Figure 5.3 – Example of a spatially correlated field illustrating ‘patches’ of higher (red) and lower (blue) values.

A spatially correlated field is described by use of a variogram function. Unlike measures such as the mean, standard deviation and variance, which describe the distribution of a variable independent of its location, a variogram characterises how one variable varies with respect to another. In this case how the material properties vary with respect to distance. In the simplest terms, if you examine one point in a rock then points close to that point are likely to have very similar material properties, but as you move further from that point the statistical likelihood that the rock will have similar properties is reduced.

A variogram consists of two parts, an experimental variogram which is obtained from the data, and the theoretical variogram model which is fitted to that data. The theoretical variogram $\gamma(h)$ for a spatially correlated field has certain key features; as h approaches zero $\gamma(h)$ will tend to zero, in terms of the material properties of granite this simply means that close to the point you are observing the values will be similar to those at that point. As h increases the values tend towards a background variance of the material (the sill), the distance, h, at which the variogram value equals the background variance is called the range, Figure 5.4. The variogram is related to the covariance function, C(h), by the equation:

$$\gamma(h) = \sigma^2 - C(h)$$

this relationship is illustrated in Figure 5.4.

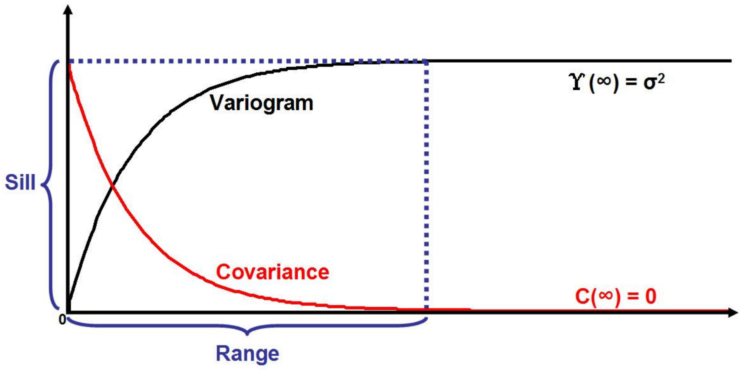

Figure 5.4 - Illustration of the relationship between the covariance function and the variogram.

The experimental variogram is obtained by comparing the difference in value of pairs of points (usually sample locations from the field), and then grouping them according to how far apart they are (h). The formula used to calculate the variogram is:

$$\gamma(h) = \frac{1}{2n(h)} \sum_{i=1}^{n(h)} \left(z(x_i) - z(x_i + h) \right)^2$$

where *z* is the value of the field (in this case Young's modulus) at the location *x*, and *n* is the number of points that are separated by the distance h. In practice, for the experimental variogram, each value of $\gamma(h)$ derived will be for a range of h (e.g. the sum for all pairs of data points that are between 5 and 10 meters apart).

In these simulations an exponential distribution was selected for the theoretical variogram to describe the heterogeneity in Young's modulus of the host rock. This takes the form:

$$\gamma(h) = \sigma^2 (1- \exp(-h/l))$$

where l is the correlation length of the field. When using an exponential distribution the range of the data is approximately equal to three times the correlation length. Figure 5.5 shows a theoretical exponential variogram with a correlation length of 20 shown by the solid line, this correlation length produces a range of approximately 60 which is similar to the average length of the initial joints. There are a number of common variogram functions that could have been adopted here, the most popular of which are Gaussian, spherical and exponential distributions. The basic properties of each of these distributions are the same, however, the shape of the variogram changes to become more, or less, convex. In the absence of any actual data from granites, the exponential function was selected, since it is commonly applied to describe variations in permeability and porosity in rocks.

The spatially correlated field shown in Figure 5.3 has a mean of zero and a variance of one. This field was generated using freely available software from mathworks (http://www.mathworks.com/matlabcentral). To validate the field simulated by the software does in fact have the correct spatial correlation, it is necessary to compare it against the theoretical variogram from which it was generated. To do this, the field in Figure 5.3 was sampled at every point, and an experimental variogram was calculated for comparison (Figure 5.5). An acceptable fit was achieved between the experimental and theoretical variograms so the field was used in subsequent simulations to generate the spatial variation in Young's modulus within the granite.

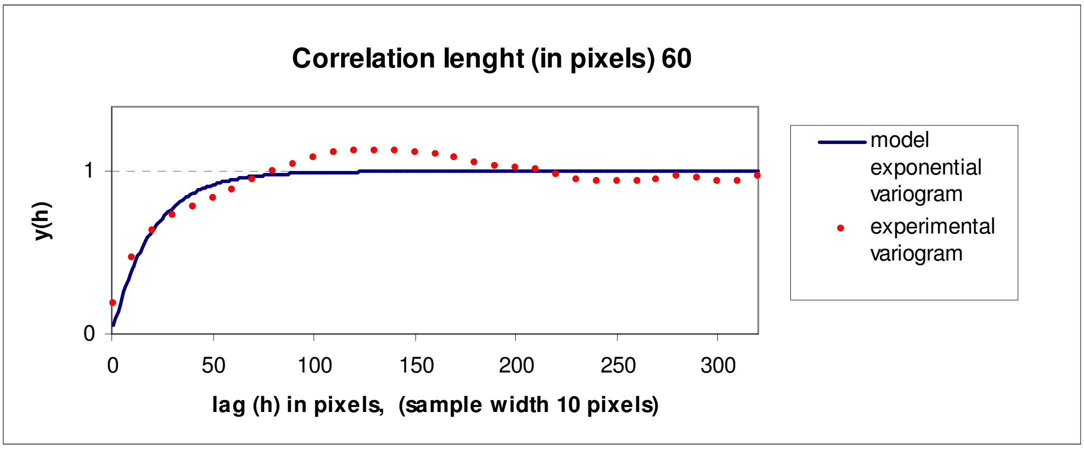

Figure 5.5 – **Experimental and model variogram for the normalised spatially correlated field shown in Figure 5.3**

It should be noted here that the use of a spatially correlated field implies that the changes in the material properties of the rock are relatively smooth. Discrete changes, such as those obtained when you move from one rock type into another are investigated in sections 5.2 and 5.3.

5.1.2 Implementation of MOPEDZ simulation

The simulations presented in Chapter 4 where the joints were orientated at 60° (Figure 4.4) and 30° (Figure 4.14) to σ_1 were repeated using the spatially correlated field shown in Figure 5.3 to investigate heterogeneity of the host rock. The values of the host rock material properties were set such that the maximum value possible was equivalent to the maximum documented value for intact granite, Young's modulus for example maintained an average of 60GPa (the same as that presented in Chapter 4) but allowed values in the spatially correlated field to range between 70GPa and 50GPa. Other than this change to the initial material properties of the host rock, the set-up and execution of the MOPEDZ simulations were the same as for those detailed in Chapter 4.

The following damage plots are slightly different to those presented in earlier chapters, in that the Young's modulus of the host rock is displayed to highlight the spatially correlated field; the fractures (damaged elements) plot as blue rather than black. An example of the initial joints within the heterogeneous host rock is shown in Figure 5.6. The joints are oriented at 60° to σ_1.

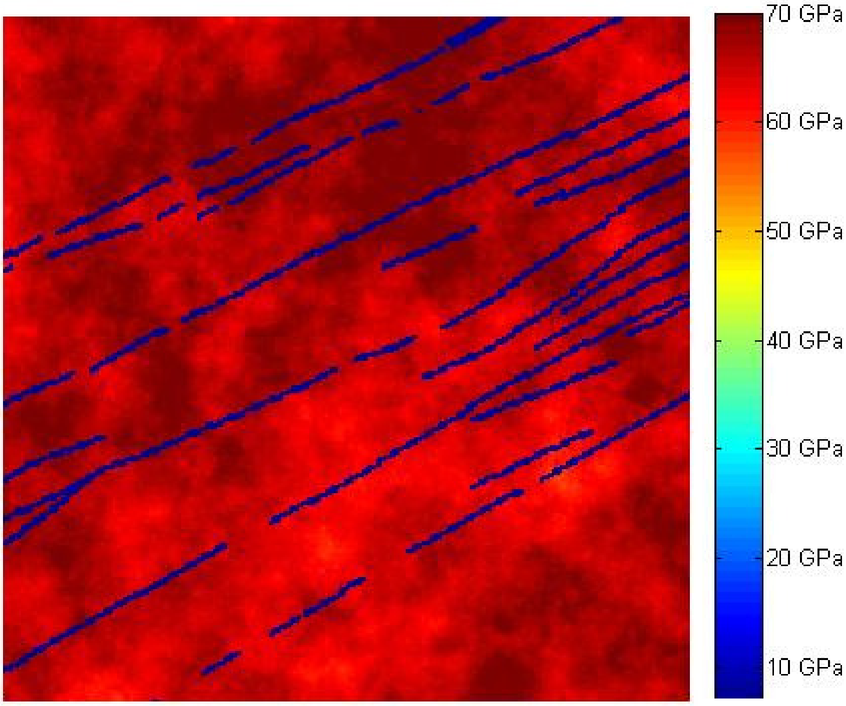

Figure 5.6 - Initial configuration of host rock with spatially correlated material properties (in this example Young's modulus) and imposed initial joint pattern where joints are at approximately 60° to σ_1.

5.1.3 Results of MOPEDZ simulations

The spatial and temporal evolution of the fracture development and linkage predicted by MOPEDZ, for the joint pattern in Figure 5.6 where the initial joints are at approximately 60° to σ_1, is shown in Figure 5.7 as a modified damage plot (full simulation in Appendix A). Note that only six frames are shown from a simulation consisting of 350 steps, (Appendix A contains a video of the full simulation).

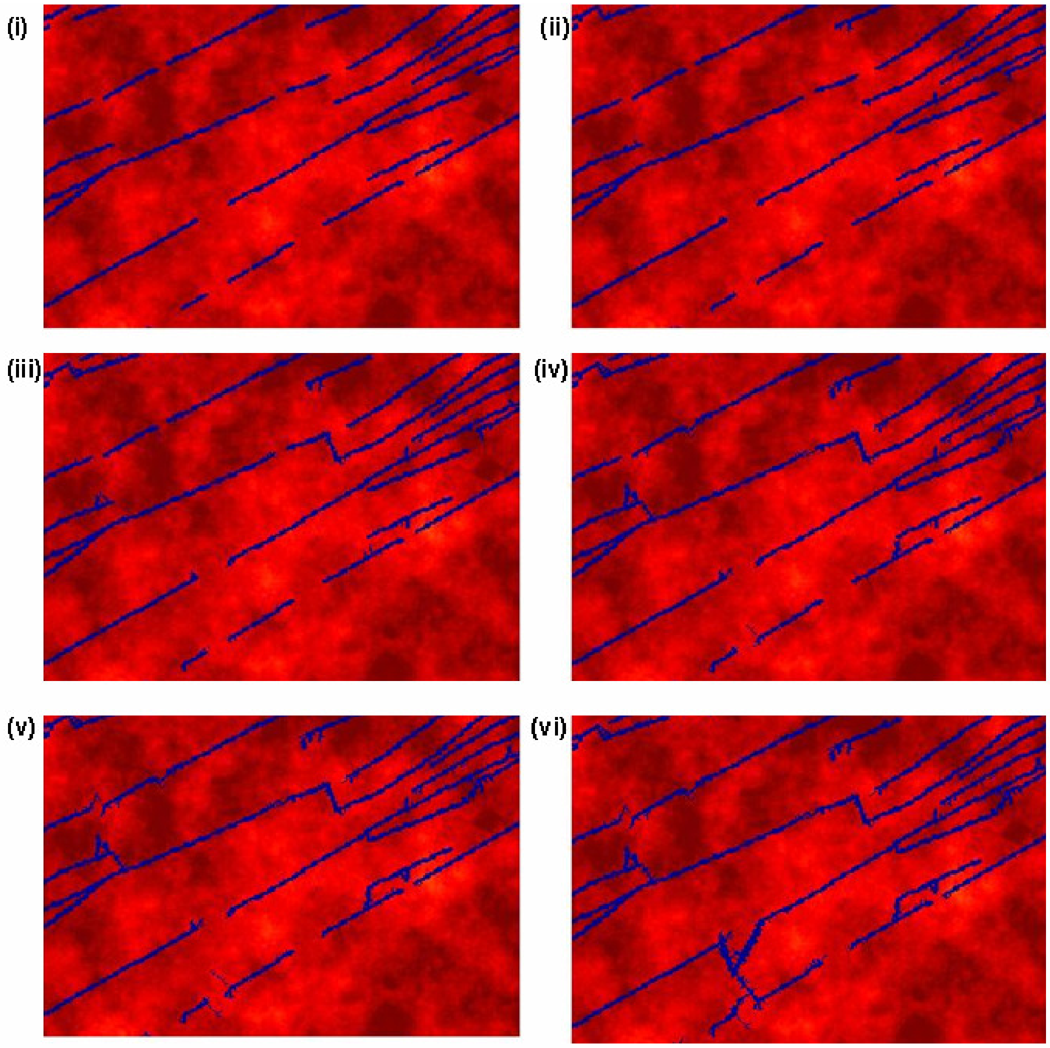

Figure 5.7 - Modified damage plot showing six frames from a simulation consisting of 300 steps which illustrate the temporal evolution of the linking fractures predicted by MOPEDZ from (i) the initial joints through to (vi) the final structure.

Comparing the evolution of the linking fractures for a heterogeneous, spatially correlated field with those produced for the homogeneous field presented in Chapter 4 (Figure 5.8) allows the following observations to be made for simulations where joints are at approximately 60° to σ_1:

- The same general structures are observed resulting in similar 'stepped' fault zone geometries both with and without the heterogeneous host rock.
- The exact location of fracture evolution may not be the same (locations B and D in Figure 5.17) but they frequently are (locations A, C and E in Figure 5.17).
- At location D in Figure 5.17a the fracture linkage between the extensional related pair of joints has been inhibited by the 'patch' of stronger rock between them.
- In the homogeneous simulation no coplanar linkage was observed between pairs of approximately coplanar joints, this style of linkage was only observed when the joints were at a low angle to σ_1. The linkage at location G (Figure 5.17a) appears to show this coplanar linkage, however, by zooming in on the location (Figure 5.17c) it is possible to observe that the structure is not coplanar and in fact follows the boundary of a slightly stronger 'patch' of granite.

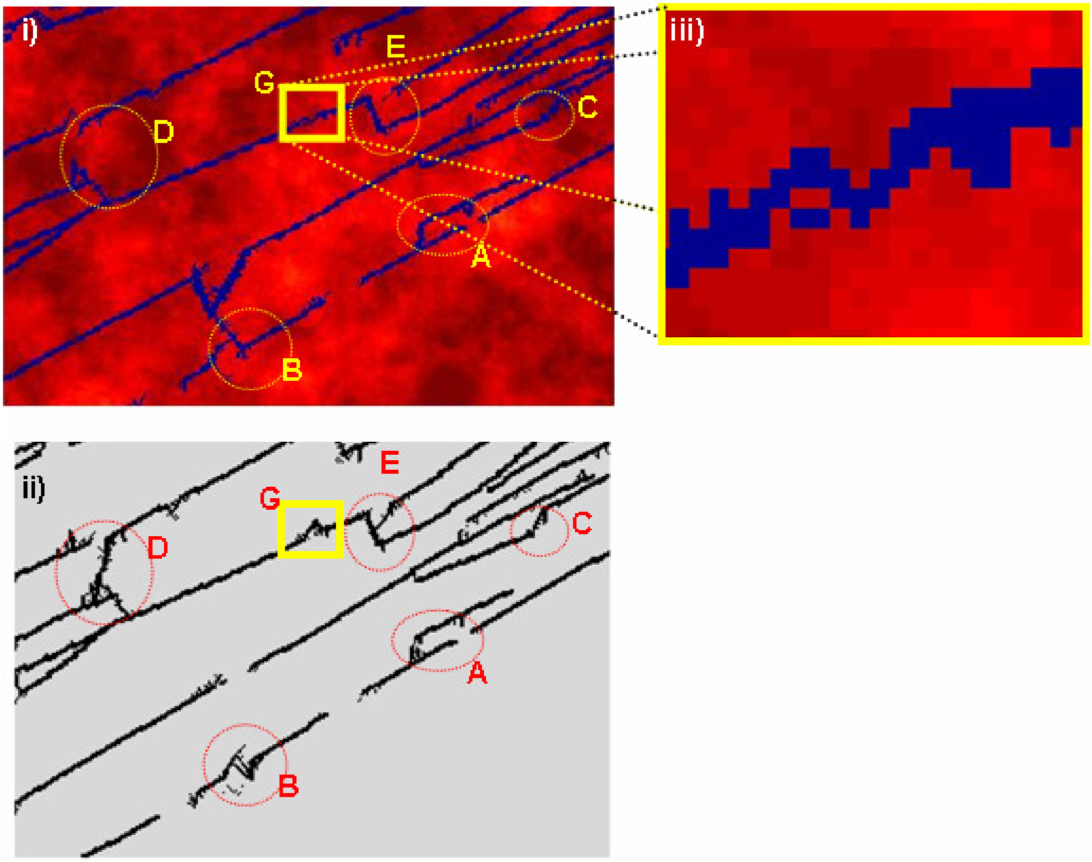

Figure 5.8 – Comparison of final linkage structures simulated by MOPEDZ for i) a host rock generated using a spatially correlated field, ii) a homogeneous host rock (repeat of final frame of Figure 4.3). Locations A to E are the same as those discussed in Chapter 4, location G is a also discussed in the text. iii) Close-up view of location (G) which gave the impression of linking along strike but in fact linkage evolves around the boundary of a stronger 'patch' of granite.

The spatial and temporal evolution of the fracture development and linkage predicted by MOPEDZ where the initial joints are at approximately 30° to σ_1, is shown in Figure 5.9 as a modified damage plot (full simulation in Appendix A).

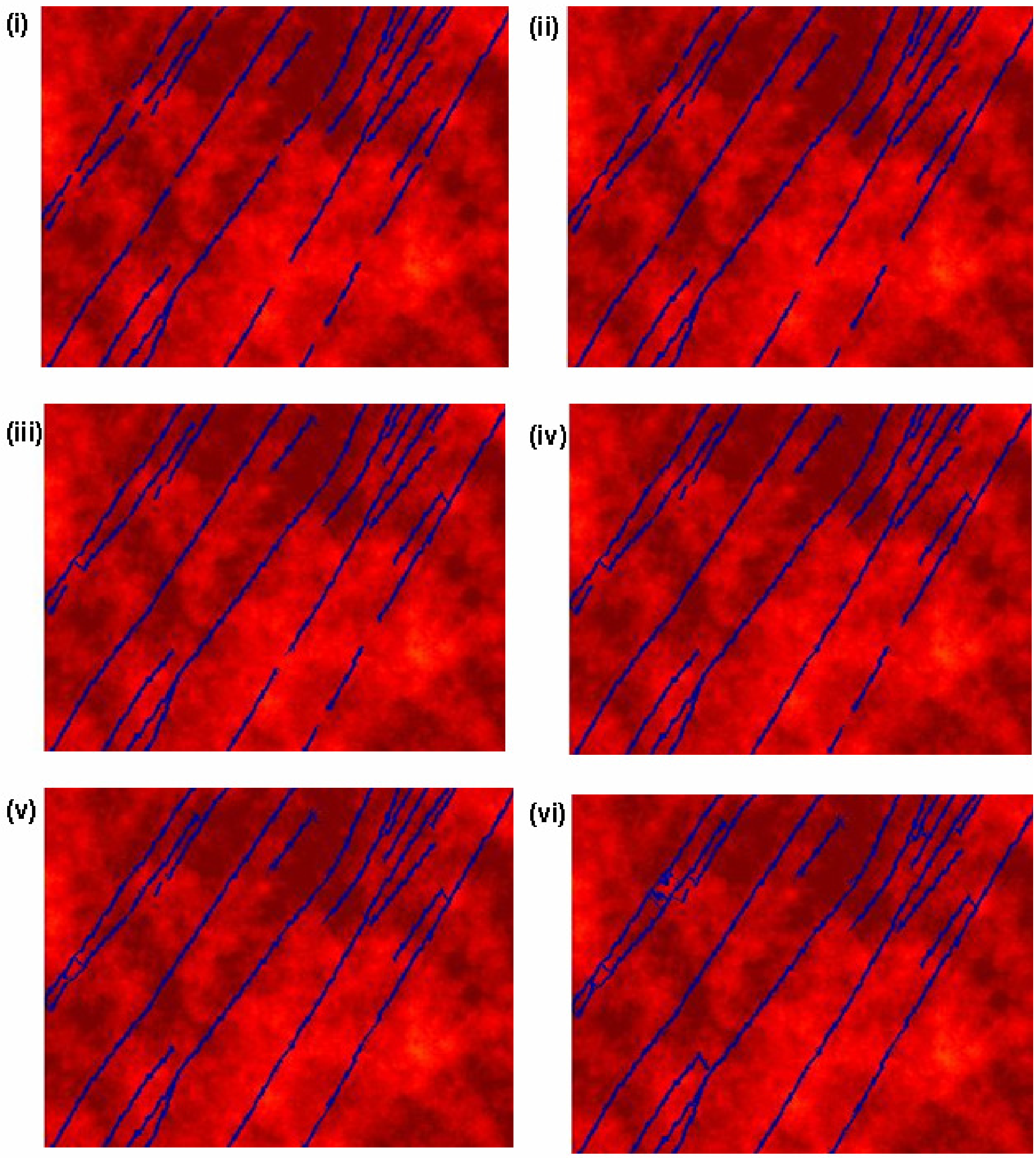

Figure 5.9 - **Modified damage plot showing six frames from a simulation consisting of 400 steps which illustrate the temporal evolution of the linking fractures predicted by MOPEDZ from (i) the initial joints through to (vi) the final structure.**

Comparing the final frame of the simulation shown in Figure 5.9 with the final frame of the homogeneous rock type with the same joint pattern (Figure 5.10) shows that in both cases the joint traces that were approximately co-linear, progressively link up along strike to form long smooth linear fault traces. The exact location of each linkage fractures is however, as in the previous example, not necessarily the same; examples, are location C, which has a ‘patch’ of stronger material between the under-lapping joints in an extensional geometry, and location F, where the wing cracks which propagate back into the compressional quadrant appear to be inhibited.

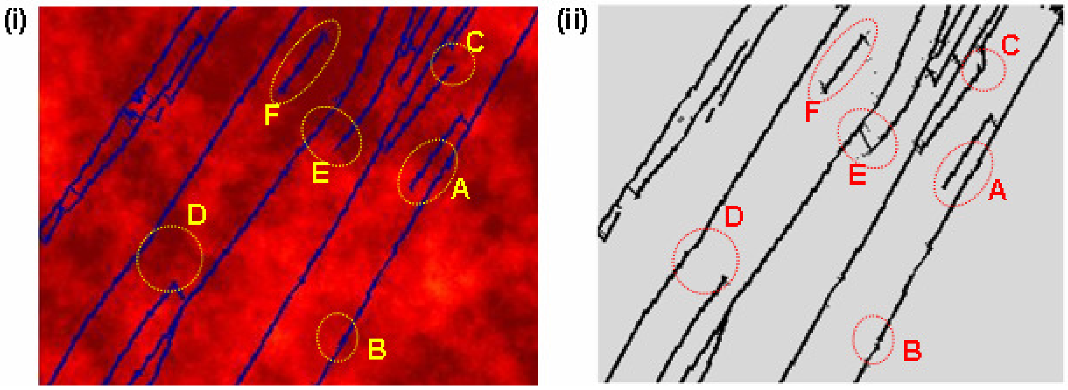

Figure 5.10 – Comparison of final linkage structures simulated by MOPEDZ for i) a host rock generated using a spatially correlated field, ii) a homogeneous host rock (repeat of final frame of Figure 4.13). Locations A to F are the same as those discussed in Chapter 4.

In summary, having a heterogeneous rock type with smoothly varying material properties does not appear to alter the general style of the linkage pattern that evolves. The dominant factor remains the orientation and relative positions of the pre-existing joints.

5.2 Investigating the effect of small-scale discrete changes in rock properties

Section 5.1 shows that smoothly varying material properties do not appear to have a significant affect on the overall geometries of fault zones that evolve from pre-existing joints. In this section, simulations explore the effect of discrete changes in material properties at a centimetre-to-metre scale.

5.2.1 Fracture evolution in Ignimbrite

Although the challenge of exploring faulting in a highly heterogeneous rock type is intellectually stimulating the main reason for examining ignimbrite is its association with nuclear waste disposal. The Yucca mountain site in Nevada, USA is comprised of ignimbrite and tuff, the Borrowdale Volcanic Group below Sellafield in the English Lake District also contains ignimbrite; both of these sites have in the past been proposed for the storage of nuclear waste. At the time of writing this thesis, work on the Yucca site has been suspended by the Obama Government.

5.2.2 What is Ignimbrite?

Ignimbrite is a highly heterogeneous rock type; it exhibits large spatial variations in composition and fabric both horizontally and vertically. Consequently, it is ideal for exploring the effect of host rock heterogeneity on fault formation. In the following sections, study of this rock type will be divided into 2 stages

- Examining the effect each parameter has on an evolving fault from a single pre-existing structure.
- Examining the interaction of a number of different pre-existing structures.

Simulation results are compared with observations from an ignimbrite deposit on Gran Canaria [*Soden,* 2008].

One definition of ignimbrite is that it includes all pumiceous materials which show evidence of having been deposited by a hot pyroclastic flow [*Walker*, 1983]. Ignimbrite deposits may blanket vast areas and have considerable thickness. The exact size and explosiveness of the eruption that generated the pyroclastic flow will determine if the deposit is controlled by topography. The extent to which the flow is fluidized influences the amount of sorting, increased fluidisation results in a greater degree of sorting. Following deposition ignimbrite may undergo a number of alteration processes [*Moon*, 1993a] :-

- Welding together of glassy fragments
- Crystallization of glassy fragments (divitrification).
- Vapour phase alteration
- Compaction

As a result of the above, the characteristics of different ignimbrite deposits vary considerably from materials suitable for building, to those that engineers would classify as soils. The characteristics of an individual deposit usually show a marked vertical variation in strength [*Moon*, 1993a]. This is exaggerated for well sorted deposits. Ignimbrite contains fiammé, Figure 5.11, which are fragments of volcanic ejecta. When deposited the fiammé were hot, had low viscosity and high permeability, following deposition they are compacted and may experience shear. The composition of fiammé ranges from volcanic glass to pumice, their shape is often idealised to an oblate ellipsoid, however, the shape is often greatly distorted by post depositional processes.

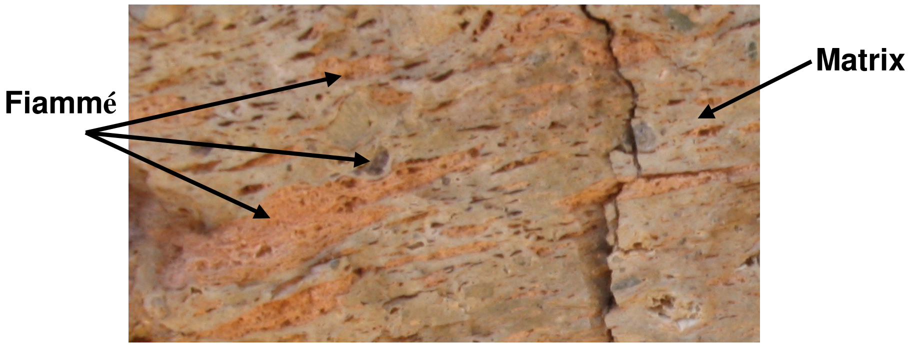

Figure 5.11 – Example of one type of ignimbrite from Gran Canaria (photo taken by Aisling Soden) showing different types of fiammé and illustrating how their shapes deviate from the idealised oblate spheroid often associated with fiammé.

From an engineering point of view one of the most significant characteristics of ignimbrite is the slake durability index. Slaking is the process in which materials weaken and disintegrate in the presence of moisture. *Moon*, [1993b] suggested dividing ignimbrite into two categories; non-durable which show a marked change in characteristics in the presence of water and durable which show little change. Durable ignimbrites have high bulk density (>1500 Kgm^{-3}, dry), effective porosity less than 35% and high strength. Only durable ignimbrites are considered in the following simulations.

Moon, [1993a] carried out a number of observations and mechanical tests on different intact ignimbrite samples, Table 5.1 shows the range of the values obtained. They suggest that compressive strength is determined by the fabric of the groundmass of the ignimbrite but that the size and distribution of the fiammé is significant as it allows a concentration of stress to develop on which micro fractures may nucleate. This agrees with observations in the field that fractures are concentrated around fiammé [*Moon*, 1993a; *Soden*, 2008]. An ignimbrite with high compressive strength will have closely packed shards which are aligned parallel to each other and are welded together, pores are in filled and fiammé are relatively small. Ignimbrites with high tensile strength also have closely packed shards which are aligned parallel to each other. Tensile strength is increased if the individual fiammé are dense and are few in number.

Table 5.1 – Example of Geomechanical properties tested by [*Moon* 1993a]

	Minimum	Maximum
Bulk Density (Kg m^{-3})		
Saturated	1644 ± 10	2290 ± 2
Oven dry	1212 ± 10	2124 ± 2
Uniaxial Compressive Strength (MNm^{-2})		
Saturated	0.23 ± 0.01	36 ± 5
Oven dry	0.73 ± 0.07	54 ± 4
Uniaxial Tensile Strength (MNm^{-2})		
Saturated	0.12 ± 0.03	7 ± 2
Oven dry	1.3 ± 0.4	7.1 ± 0.7

Ignimbrite deposits often have primary jointing due to cooling and compaction. Field observations [*Moon*, 1993a; *Soden*, 2007] show that, in ignimbrite, fractures are commonly associated with fiammé: the boundary between the fiammé and the matrix is often fractured and/or new fractures propagate from the tip of a fiammé. *Soden*, [2007] observed that joint density appears to be related to the abundance of fiammé. Hence, a logical first step in modeling ignimbrite is to model the effect of the fiammé.

5.2.3 Faulting associated with a single fiammé

The basic initial setup for modelling faulting around a single fiammé is shown in Figure 5.12 although in the early simulations described below, the elements for the fiammé/matrix boundary (orange squares) were not included. For all simulations the matrix parameters were as listed in Table 5.2 and the parameters of the fiammé were set as a fixed ratio to those values. Using this initial configuration the effect of the relative strength's of the matrix and the fiammé, the degree of welding between the matrix and the fiammé, the inclination of the fiammé and the aspect ratio of the fiammé were investigated to explore the effect each had on a propagating fracture. Unlike previous simulations presented in this thesis, which have a low stress ratio with $\sigma_1 \approx 2\sigma_3$, the ignimbrite simulations were carried out with a high stress ratio with σ_1 much greater than σ_3. This high ratio was chosen because it is consistent with the shallow burial experienced by these rocks. Results presented in the following sections are in the form of damage plots, with the different host rock materials being represented by different colours (as described, where necessary, in the appropriate figure caption).

Table 5.2 – Material Properties for matrix

Matrix Property	Value
Host Rock Young's modulus	18 GPa
Host rock Poisson's ratio	0.3
Co (Shear strength)	40 MPa
μ (Coefficient of friction)	0.6
To (Tensile strength)	4.2 MPa
Number of cells permitted to fail in any one step of the MOPEDZ code	6

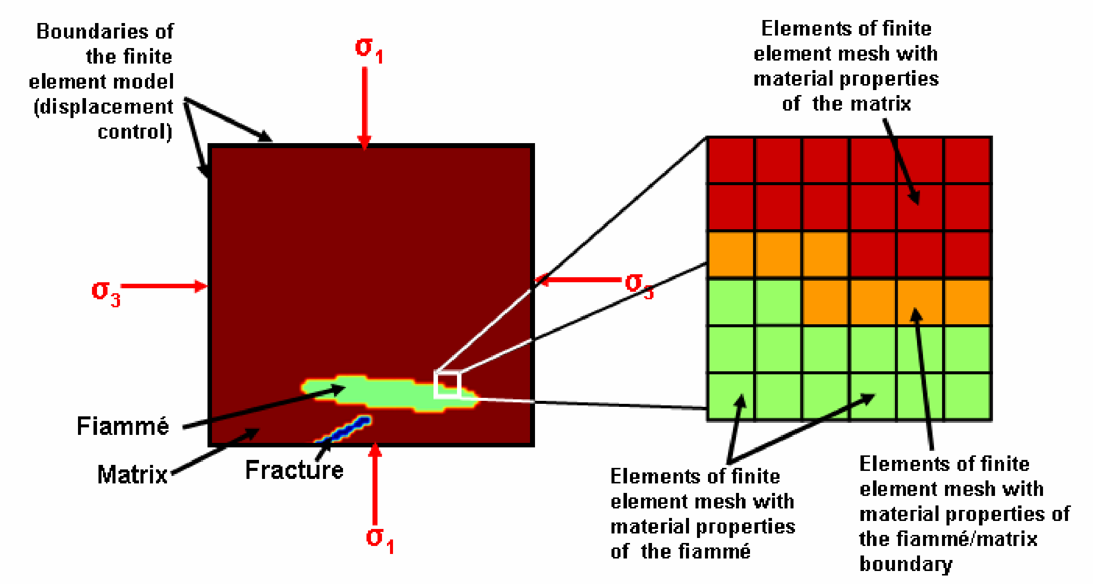

Figure 5.12 – **Initial configuration for MOPEDZ simulations exploring the effect of fiammé on the propagating fracture.**

5.2.3.1 How does changing the relative strengths at the discrete boundary affect the evolving fracture?

The following simulations explore how, by adjusting the relative strength of the matrix and the fiammé, a discrete change in material properties affects an evolving fracture. These initial simulations ignore the effect due to welding at the fiammé boundary (i.e. in Figure 5.2 the orange elements were not present). Figure 5.13 shows the evolution of a fracture (black) as it approaches a fiammé (orange) with a stronger matrix (red). In this case the fiammé was set much weaker than the matrix (ratio of 0.6) multiple fractures developed within the fiammé which eventually shattered (simulation failed in a catastrophic manner), Figure 5.13.

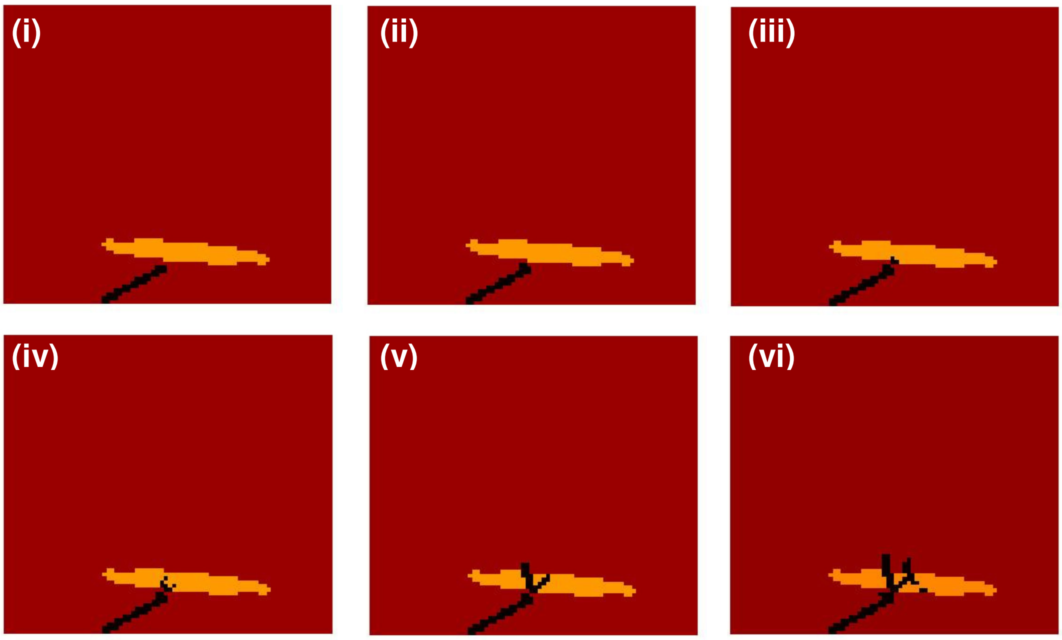

Figure 5.13 – **Fracturing through a single fiammé when fiammé strength is 0.6 of the matrix (fracture-black, fiammé-orange & matrix red).**

Figure 5.14 explores the same fracture evolution scenario, for the situation where the fiammé are stronger than the matrix. In this case, they appear to inhibit fracture propagation.

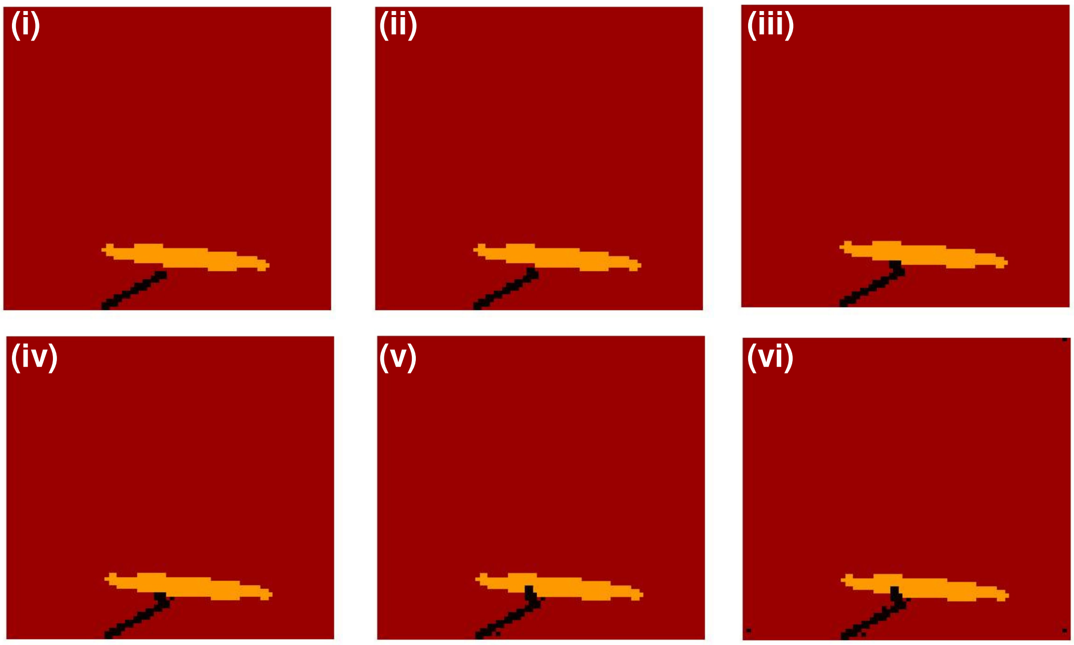

Figure 5.14 – Fracturing through a single fiammé when fiammé strength is 1.3 of the matrix.

A wide range of values for the relative strength of the matrix and fiammé were explored, however, at no point did the fracture propagate along the fiammé boundary; a feature which, as stated above, is often observed in the field.

The matrix of the ignimbrite is formed from volcanic ash and is often observed to have a layered structure, this feature may have an effect on the fracturing of the rock and cause the fracture to follow the fiammé boundary. To explore this possibility the matrix was adjusted to be comprised of alternating layers of material which had properties at the top and bottom of the range of those listed in Table 5.1. Fracturing along the fiammé boundary was still not observed, results for a weak fiammé (ratio of 0.7) are shown by way of example in Figure 5.15.

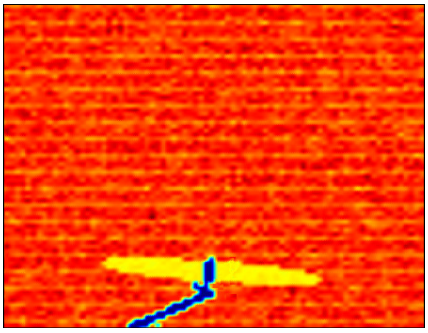

Figure 5.15 – Fiammé (yellow) in a layered matrix (orange). Propagating fracture (blue) is not deflected nor does it follow the fiammé boundary Fiammé is weaker than the host (ratio of 0.7).

5.2.3.2 Degree of welding between the matrix and the fiammé

It has been observed that true glassy welding between the fiammé and matrix is very rare in ignimbrites [*Moon*, 1993a]. To reproduce this observation within the simulations, it is reasonable to reduce the strength of the fiammé/matrix boundary. This was achieved by having a thin layer around the fiammé with reduced material properties as illustrated in Figure 5.12. Results from a simulation that includes these boundary welding effects are shown in Figure 5.16. In this case, both fracturing around fiammé within the ignimbrite and displacement of the fracture across the fiammé are successfully simulated.

The results in Figure 5.16 are consistent with observations by Soden in Gran Canaria. These simulation results are only produced when the fiammé are weaker than the host rock (~75%) but not so weak that they just shatter (>60%), further the fiammé must have a weak boundary (~50% of host rock) between the two distinct rock types.

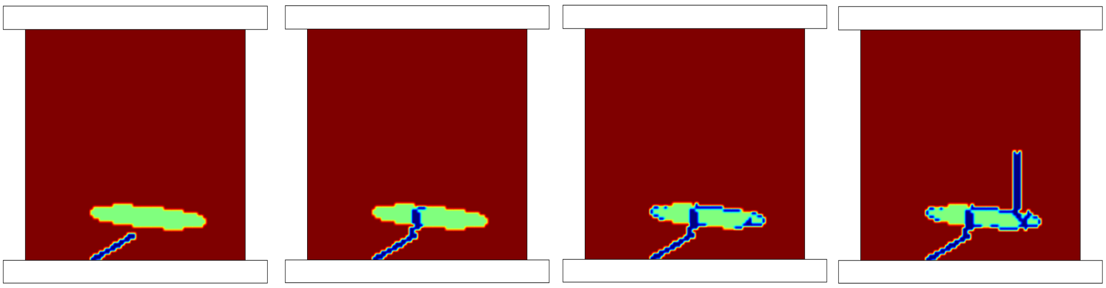

Figure 5.16 – MOPEDZ simulation of a fracture propagating through fiammé in ignimbrite as boundaries are displaced. Red represents ignimbrite matrix, green the fiammé and blue the developing fracture. The boundary between the matrix and the fiammé is 50% weaker than the host rock and has lower coefficient of friction while the fiammé has values of strength, Young's modulus and Poisson's ratio which are set at 75% of the host rock. (fracture-blue, fiammé-green, fiammé/matrix boundary - yellow & matrix red).

5.2.3.3 Inclination of the fiammé

As the orientation of joints to σ_1 has a strong influence on fracture evolution in the simulations presented in Chapter 4, it seemed sensible to explore the effect of fiammé inclination might have on the evolving fracture. The fiammé were not inclined to a high angle as the fiammé present in the field site were all close to being horizontal.

Inclining the fiammé from the horizontal had little effect on the propagating fracture. The fiammé in Figure 5.17(i) is inclined at 10°

and can be compared to the horizontal fiammé in Figure 5.17(ii). It should be noted that any fractures which don't pass directly through the fiammé and instead propagate from the opposite edge of the fiammé, some distance from the initial intersection, always appear to propagate from steps in the fiammé boundary where stress concentrations are slightly higher. This 'stepped' structure of the fiammé boundary (Figure 5.12) is due to the pixelated setup of the finite element mesh but is not unreasonable given that the boundary of the fiammé are rarely perfectly smooth oblate ellipsoids (Figure 5.11).

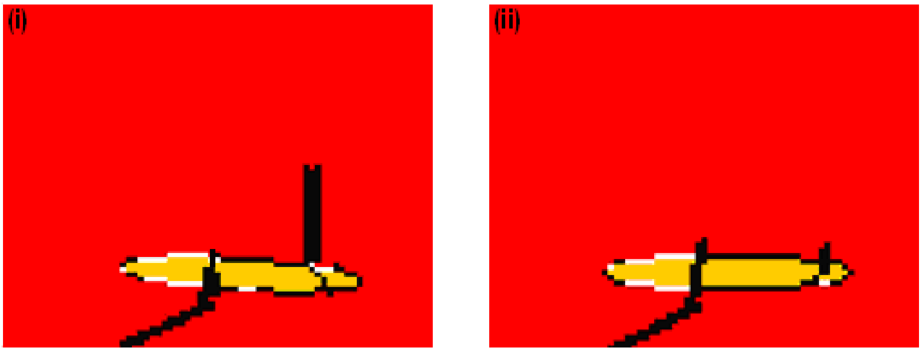

Figure 5.17 – Effect of inclination. Same general structures are observed when the fiammé are inclined from horizontal, (i) 10° from horizontal, (ii) horizontal. In both simulations the strength of the fiammé is 75% of the matrix and the contact between the matrix and the fiammé is 50% of the matrix. (fracture-black, fiammé-orange, fiammé/matrix boundary - white & matrix red).

5.2.3.4 Aspect ratio of the fiammé

Field observations suggest that aspect of the fiammé ratio may have an influence on fracture propagation, this is in agreement with research by *Eshelby* [1957 & 1959] who showed that the strain disturbance around and ellipsoid inclusion depends on its shape.

Consequently, this effect was investigated within MOPEDZ. Figure 5.18 shows that as aspect ratio decreases (fiammé get 'rounder') the deflection of any propagating fracture is reduced (it is more likely to go straight through the fiammé) and it is less likely that new fractures will propagate from the tips of the fiammé.

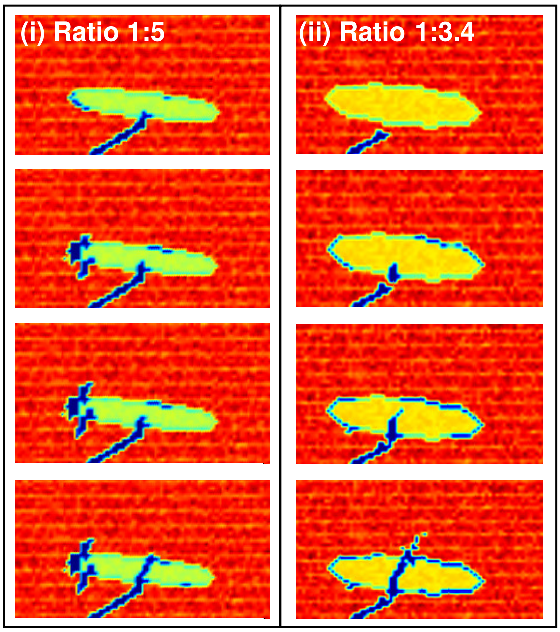

Figure 5.18 – **Effect of the aspect ratio, (i) ratio of 1 : 5, (ii) ratio of 1 : 3.4. As aspect ratio decreases fractures are less likely to be displaced and new fractures don't propagate from the tip of the fiammé. In both simulations the strength of the fiammé is 75% of the matrix and the contact between the matrix and the fiammé is 50% of the matrix. (fracture-blue, fiammé-yellow, fiammé/matrix boundary - green & matrix orange).**

This is consistent with observations made by Soden (Soden, 2008). Figure 5.19 (annotated example of Figure 5.11) shows a fracture which is displaced by a high aspect ratio fiammé but not by low aspect ratio ones.

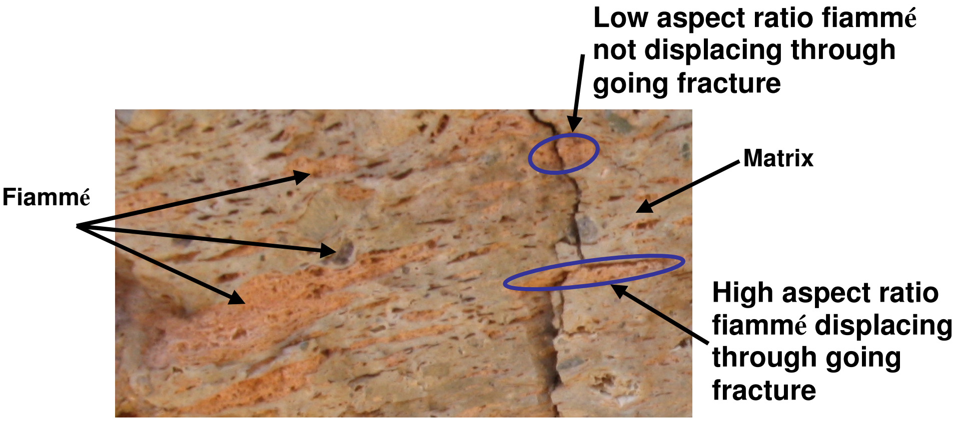

Figure 5.19 – Effect of aspect ratio. Annotated example of Figure 5.11

The evolution of new fractures propagating from the tip of thinner fiammé can be explained by examining the stress field. The shear stress field for a single (weaker) fiammé within a homogeneous matrix is shown in Figure 5.20; both simulations have the same boundary displacements and material properties, there is no weak boundary between the fiammé and matrix in these simulations. The only difference between the simulations shown in Figure 5.20 is the aspect ratio of the fiammé, the thinner fiammé has much higher stress values at the tip which will facilitate the propagation of new fractures.

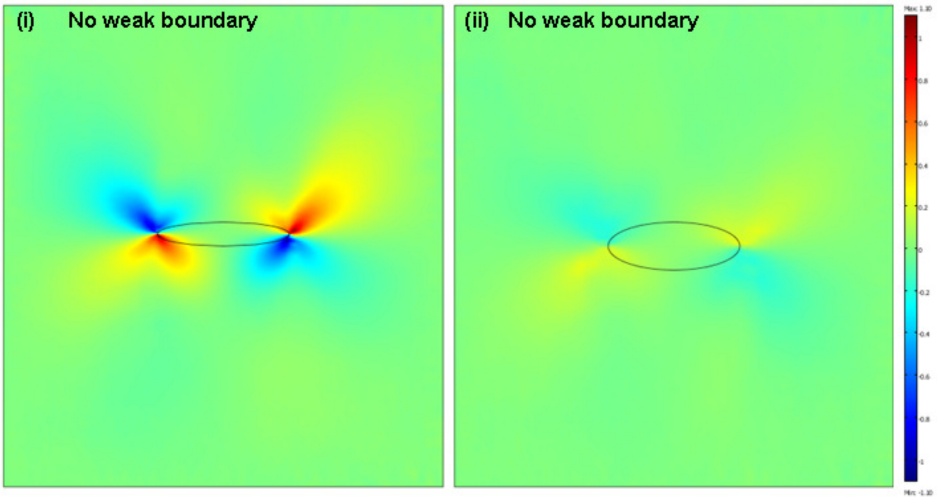

Figure 5.20 - **Shear stress field produced around a weaker fiammé within a homogeneous matrix. Both simulations have same boundary displacements and material properties, the only difference is in the aspect ratio of the fiammé. To allow direct comparison of the different stress fields which evolve because of the different geometries of the fiammé, the same scales are used in both plots.**

The above MOPEDZ simulations show that for a single fiammé, the variability in fracturing observed in the ignimbrite deposits of Gran Canaria can be explained by (1) the existence of a weak contact between the fiammé and the matrix, and (2) variations in the fiammé's aspect ratio. Both of these effect the amount of deflection of a propagating fracture and the likelihood of initiating a new fracture.

5.2.4 Faulting associated with multiple fiammé

Research by Soden [2007], based on field obsesrvations in Gran Canaria, suggested a method of fault core development that was related to the number and shape of the fiammé present in the rock unit. Soden [2007] observed that where there were abundant thin fiammé there were also closely spaced joints. Soden theorised that the fault core developed between these joints as the ignimbrite broke into blocks which rotated and broke down further as one side moved past the other (Figure 5.21). The suggestion was that the alternating thin fiammé and matrix provide layers with sufficiently different mechanical properties that fracturing between adjacent joints allowed the host rock between the two joints to form blocks. By contrast, where the fiammé were less numerous or the fiammé had a low aspect ratio (were rounder) the joints were wider apart and the development of fault core did not appear to be related to the fiammé.

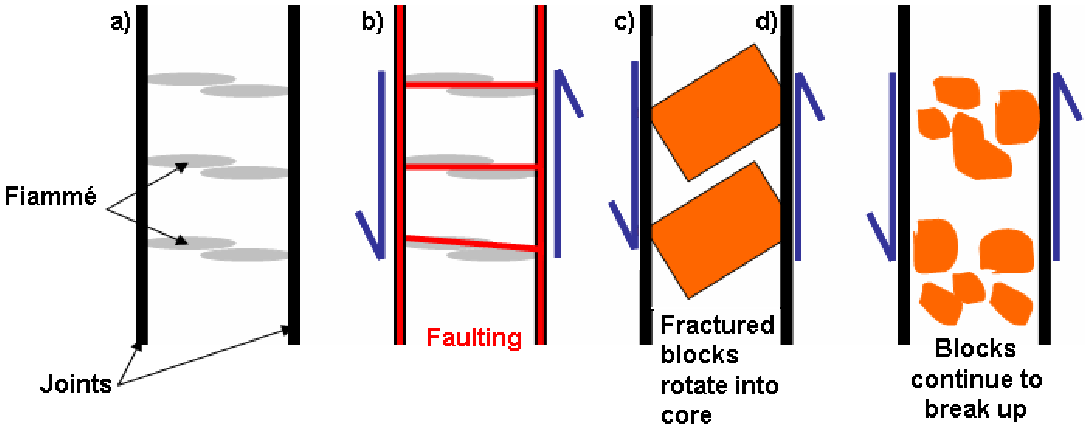

Figure 5.21 – Illustration of the sequence of events relating fault core evolution to the existence of many thin fiammé based on a hypothesis proposed by *Sodden* [2007].

Soden's theory requires two conditions to be met; first there has to be many closely spaced joints and second, the host rock between them must be able to break into blocks. Simulations with individual fiammé show that fiammé with a high aspect ratio generate new fractures from their tips (Figure 5.18), when many fiammé are present if these tips line up it will allow fractures to grow between them (Figure 5.22) which may explain why more vertical joints are observed in the ignimbrite deposits with many thin fiammé than for those deposits with fewer or "rounder" fiammé.

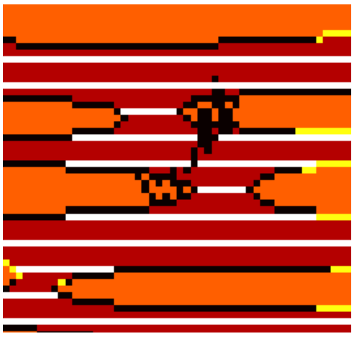

Figure 5.22 - **Fracture developing between the tips of adjacent fiammé, one possible mechanism for the evolution of frequent joints within an ignimbrite deposit. (fracture-black, fiammé-orange (material properties 75% of matrix), fiammé/matrix boundary - yellow (material properties 50% of matrix) & layered matrix red and white).**

For the ignimbrite between joints to break into blocks fracturing needs to occur roughly perpendicular to the joints, the most obvious mechanism for this is the different mechanical layers generated between the matrix and the fiammé. The simulations with single fiammé showed that for this fracturing to occur there must be a weak layer between the fiammé and the matrix (Figure 5.16), this also holds true for simulations with multiple fiammé (Figure 5.23). If there is true glassy welding of the fiammé (no weak layer between the fiammé and the matrix, Figure 5.23b) then no horizontal fracturing occurs. This result suggests that for the second requirement of Sodden's theory to be met there must be a weak contact between fiammé and matrix.

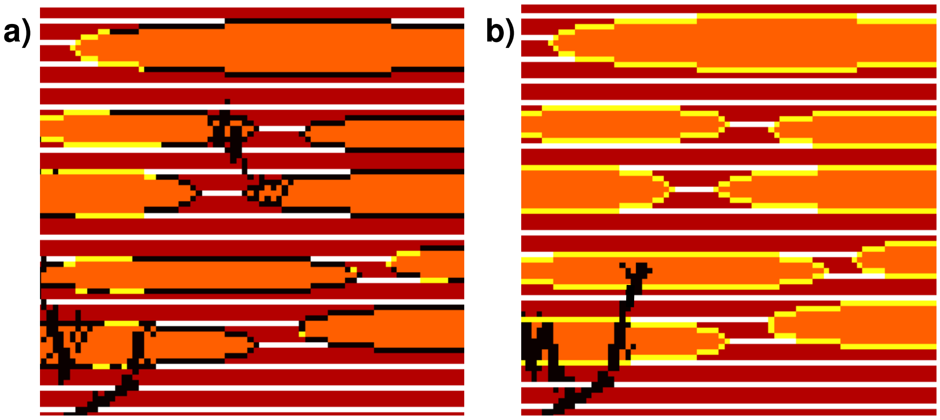

Figure 5.23 - For simulation a) there is a weak boundary between fiammé and matrix, this simulation shows significant horizontal fracturing. In simulation b) the boundary was set with the same value as the matrix and exhibits no horizontal fracturing.

5.2.5 Discussion of faulting in ignimbrite

For the ignimbrite deposit examined in Gran Canaria the simulations seem to hold with the geological observations which have been made and begin to validate Soden's theory of fault core evolution within the ignimbrite deposits which contain many thin fiammé.

More generally, having discrete boundaries between different rock types appears to significantly effect fracture evolution for two scenarios. First, if there is a significant change in the material properties between rock types, and second, if the geometry of the different rock types is such that it allows stress concentrations to build up at a single point e.g. low Vs high aspect ratio of fiammé.

5.3 Increasing the heterogeneity – discrete changes (large scale)

As mentioned in the introduction of this thesis one of the major uncertainties in flow simulation models is in predicting the permeability of faults, principally in the detailed structure of the fault zone. It is hoped that ultimately MOPEDZ can be used to reduce this uncertainty and enhance flow simulation models. For this to occur MOPEDZ will have to be able to model regional as well as small scale faulting.

Faults and fault damage zones are not restricted to one rock type; on a regional scale a fault will cut many lithologies, for example, Figure 5.24 shows a section of the Black Flag Fault in Western Australia which cuts through several different lithologies. Many economically significant mineral deposits such as gold are associated with focused fluid flow through such fault zones.

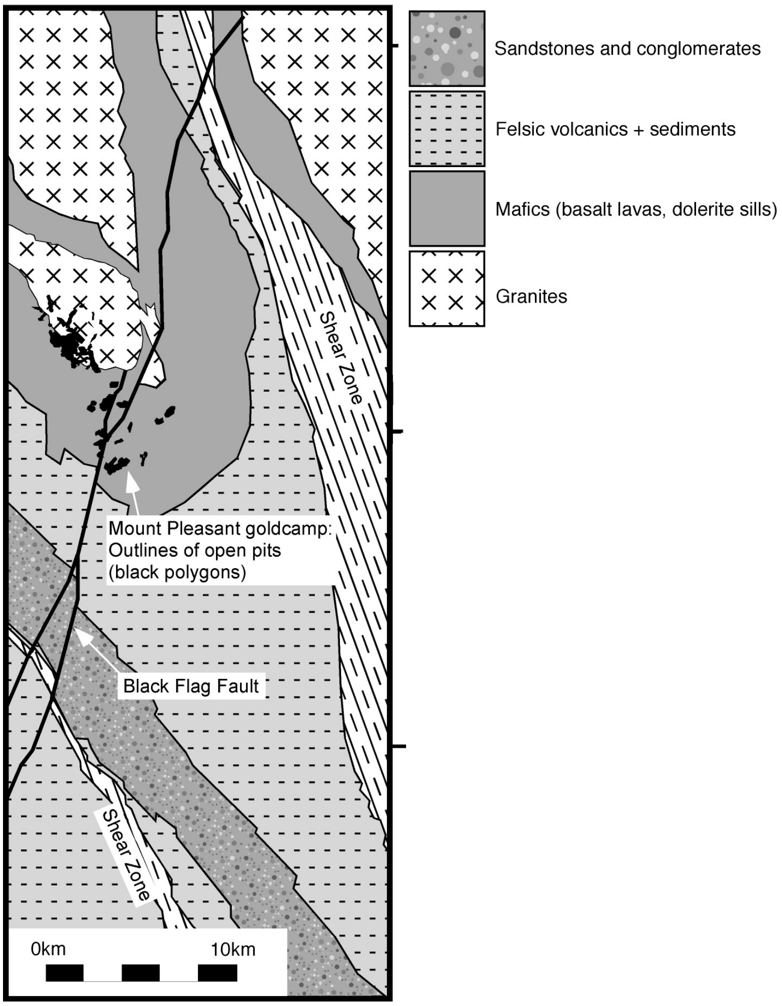

Figure 5.24 – Geological map showing the Black Flag fault in Western Australia cutting several lithologies. Gold mines associated with the fault are also shown.

Gold deposits are the product of focused fluid flow through faulted crust. However, it is small-scale faults that are marginal or peripheral to larger-scale features that are most productive [*Micklethwaite & Cox*, 2004; *Bierlein et al.*, 2006], for example, many of the gold camps indicated in Figure 5.24 are associated with small splay fractures adjacent to the main Black Flag fault, it is these small structures that produce significant gold deposits. The small splay fractures do not appear to be physically connected to the major Black Flag fault [*Micklethwaite & Cox*, 2004].

One theory as to why the gold deposits are associated with these small fractures is related to changes in the local stress field. Following a major slip event aftershocks will occur as the stress field dissipates. Areas of higher stress levels are the likely locations of these aftershocks. The assumption is that these areas become temporarily permeable and exhibit localised fluid flow as a result of aftershocks localised on higher stress levels adjacent to the major fault system [*Micklethwaite & Cox*, 2004].

5.3.1 Large Scale MOPEDZ simulations

The largest simulations presented so far in this thesis have been a few meters in width. Consequently, to simulate faulting at the scale of the linkage structure at the jog in the Black Flag Fault (Figure 5.24) required a significant change in the area represented by an individual element within the finite element mesh. To investigate any effects derived purely from the change in scale, an initial simple linkage structure in a homogeneous rock type was simulated for a model domain of 20km^2 (Figure 5.25). The linkage structure developed in a similar manner to that shown for the smaller simulations, before failing in a catastrophic manner (Figure 5.25(v)).

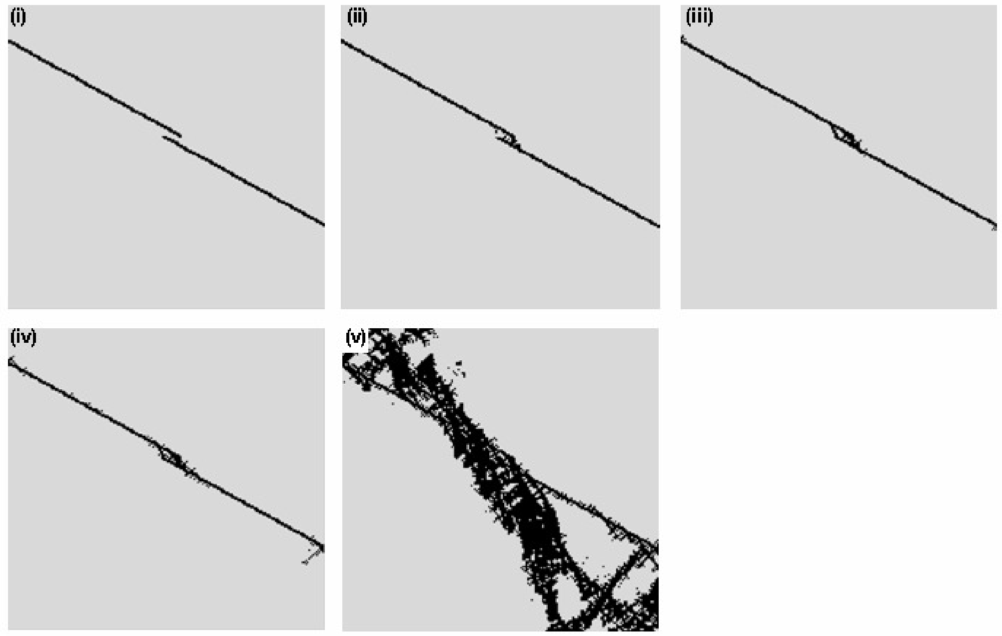

Figure 5.25 – **Linkage of two pre-existing faults in a homogeneous rock type, simulated area is 20km^2. Following development of the linkage structure the simulation fails uncontrollably.**

5.3.2 Implementation of MOPEDZ simulation containing different lithologies

Following the simulation for a single rock type in Figure 5.25, four different lithologies, shown in Figure 5.24, were introduced. The simulations were conducted with the modified MOPEDZ code using a low stress ratio. Dr Micklethwaite provided some data on the range of values for Young's modulus and Poisson's ratio that could be expected from the from the site:

Sandstones	Youngs modulus (E) = 1.0-6.0 x 10^5 bars
	Poissons ratio (dry rock) = *0.2-0.3*
Granite	Youngs modulus (E) = 4.0-7.0 x 10^5 bars
	Poissons ratio (dry rock) = *0.1-0.25*
Mafics	Youngs modulus (E) = 6.0-8.0 x 10^5 bars
	Poissons ratio (dry rock) = *0.25*

The material property values which were chosen for the following simulations were those listed in Table 5.3. The same properties for granite were chosen as those for the simulations presented in Chapter 4 as these lay within the range of values provided. There was a wide range in the material property values provided for the sandstone, a number of simulations were carried out only altering the properties of the sandstone unit and it was found that the material properties for the sandstone had to be at the high end of the range provided by Micklethwaite; as when they dropped towards the low end (<65% of the values for granite) the simulations resulted (following the development of the linkage structure) in catastrophic uncontrolled failure within the sandstone unit. No data was provided on the felsics and they were given a value between the granite and the mafics. During the early development of MOPEDZ it was established that the material property which MOPEDZ was most sensitive to is Young's modulus. Values for Young's modulus were provided for all the rock types, where data on the other material properties of a particular rock type was missing and could not be found in the literature, the value had to be estimated. The estimation was achieved by taking the ratio of the Young's modulus between the particular rock type and the granite and maintaining that ratio when applied to the other material properties.

Table 5.3 – Material properties used during the Black Flag simulations.

Rock Type	Mafics	Sandstone	Felsics	Granite
Young's Modulus (GPa)	80	50	70	60
Poissons's ratio	0.25	0.2	0.2	0.2
Shear strength (MPa)	174	108	152	130
Coefficient of friction	0.6	0.6	0.6	0.6
Tensile strength MPa	13.3	8.3	11.7	10

To investigate the effect of large scale lithological variation on fault linkage, a section of the Black flag fault (Figure 5.24 and 5.26a) was recreated as input to a MOPEDZ simulation, Figure 5.26b. The area chosen had to be rotated such that σ_1 was top to bottom (this is a requirement of the code), the final setup for the MOPEDZ simulation is shown in Figure 5.26c (Note that due to the fact that the shear zone will have anisotropic material characteristics which at present are not simulated in MOPEDZ and that no data were provided for the material properties of the shear zone it has been omitted from this map).

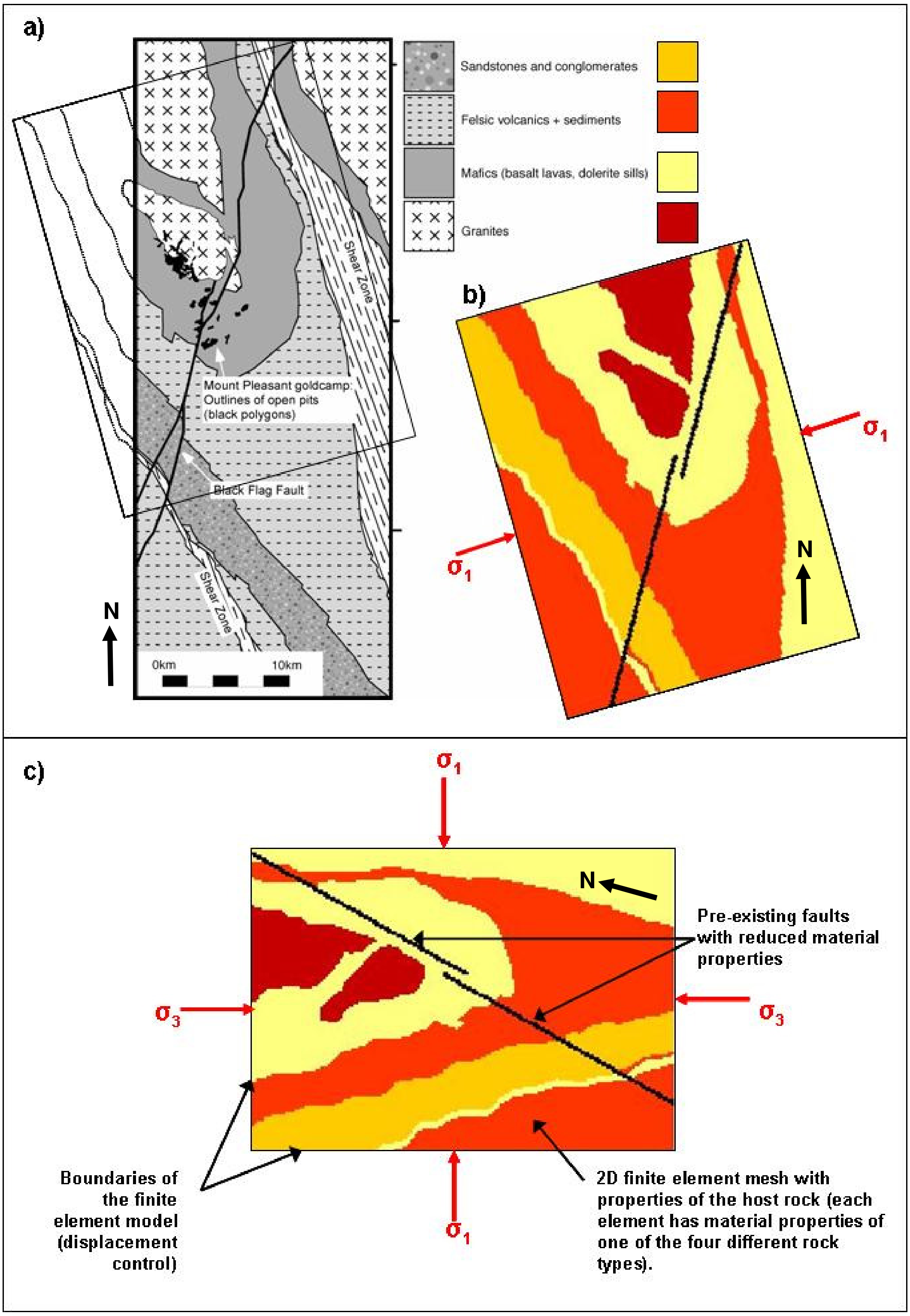

Figure 5.26 - MOPEDZ setup for Black Flag Fault simulation. a) geological map of a section of the Black-Flag Fault (provided by Micklethwaite) with a box marking the area to simulated in MOPEDZ. b) Host rock pattern to be entered into MOPEDZ, shown in the same orientation as the base map. c) MOPEDZ setup with rock pattern rotated such that σ_1 is applied top-to-bottom.

5.3.3 Results of MOPEDZ simulation

The results of the simulation are shown as a strain plot in Figure 5.27, in this simulation the pre-existing faults were input as two long straight features. As the simulation progresses strain increases throughout the simulation and the different rock units can be clearly identified since they accommodate different strains. Initially, the two faults develop a linkage structure, only once this structure has fully formed does faulting start to occur in the nearby granite (Figure 5.27(iv)). As the simulation continues the new fault continues to develop in the granite in a location similar to that which has been mined shown to the ;left of the main fault in Figure 5.24. No fracturing is predicted by MOPEDZ to the west of the fault.

It is worth noting that many of the initial failures adjacent to the linkage structure are in tension, this is of interest as failure in tension will create an ideal scenario for fluid flow and gold deposition. However, at the scale of this simulation each element in the finite element mesh represents an area approximately 150m wide and could contain any number of failures at a scale smaller than this.

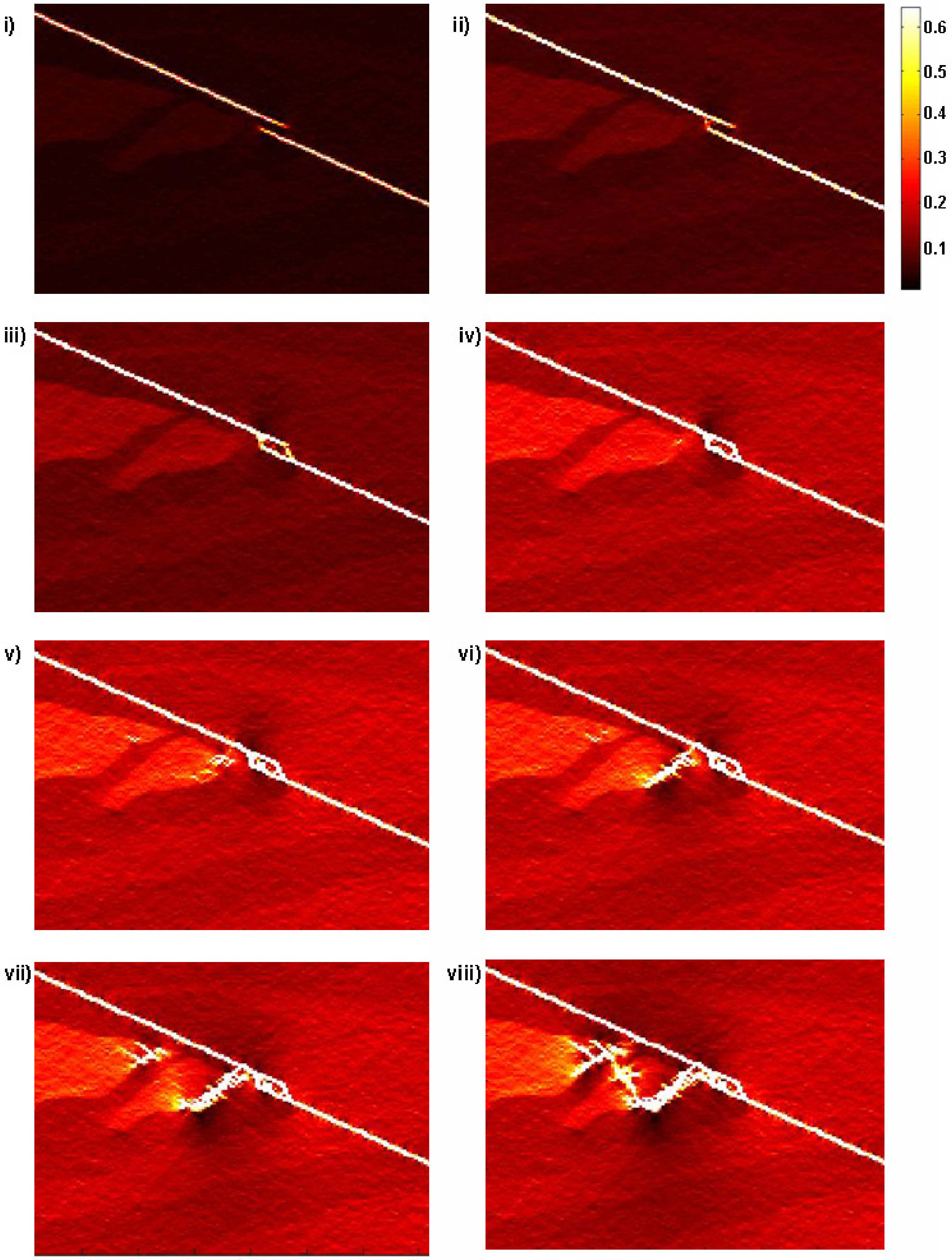

Figure 5.27 - Strain plot showing eight frames from a simulation consisting of 400 steps which illustrate the temporal evolution of the linking fractures (extensional geometry) predicted by MOPEDZ from (i) the initial joints through to (vi) the final structure.

The faults in Figure 5.27 have an extensional relationship. As the relative positions of the initial faults/joints have been shown the have a significant effect on the pattern of fractures in a homogeneous rock type the simulation was repeated but with the initial faults in a compressional relationship, Figure 5.28. In this simulation there is some strain increase in the granite but most failures are associated with the Mafic/Felsic boundary which is quickly followed by uncontrolled failure of the simulation.

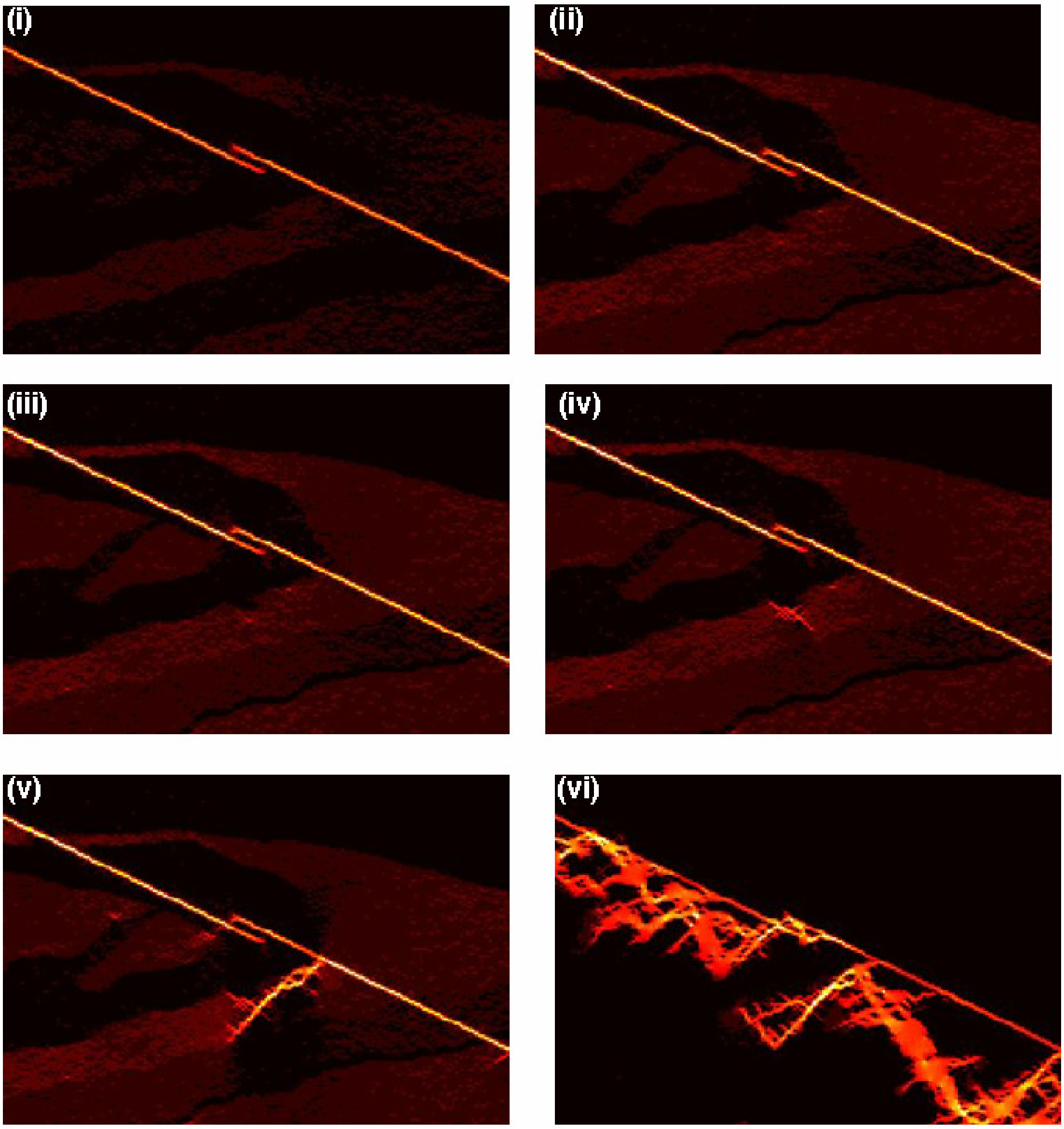

Figure 5.28 - **Strain plot showing six frames from a simulation consisting of 400 steps which illustrate the temporal evolution of the linking fractures (contractional geometry) predicted by MOPEDZ from (i) the initial joints through to (vi) the final uncontrolled failure.**

The development work with the ignimbrite deposits showed that a weak contact between mechanically different materials can have an effect on the pattern of fracturing or faulting which evolves. A weak contact between the mafic and felsic rocks was introduced to the original simulation (in Figure 5.27), the results of which are shown as a damage plot in Figure 5.29. This simulation shows failure on the weak boundary even before the linkage structure is fully developed. The simulation then experiences uncontrolled failure, significantly there is no failure in the granite, which has been shown to produce significant gold deposits.

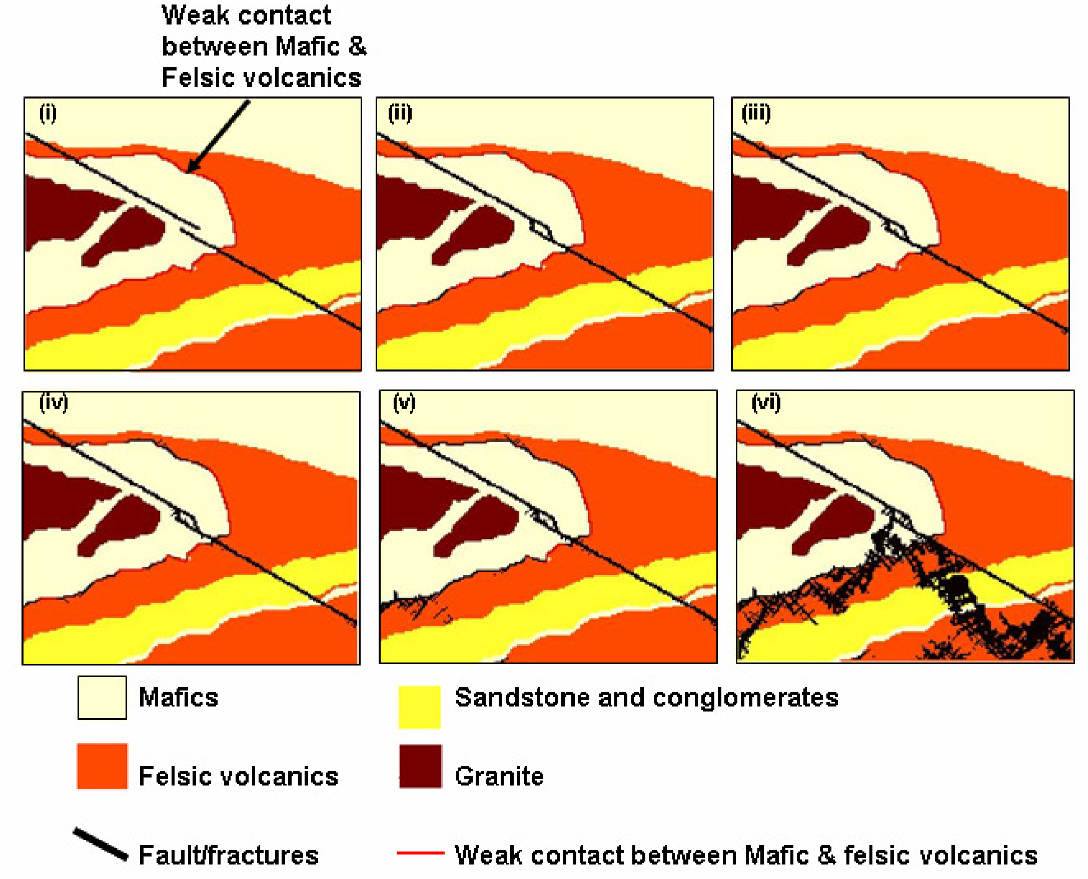

Figure 5.29 - Damage plot showing six frames from a simulation consisting of 400 steps which illustrate the temporal evolution of the linking fractures (extensional geometry) predicted by MOPEDZ from (i) the initial joints through to (vi) the final uncontrolled failure. In this simulation a weak contact between the mafic and felsic rocks has been introduced.

The simulations of the jog in the Black Flag Fault show how essential it is to have good field and laboratory data to input into any numerical model. Data are required not only on the outcrop geometry, the likely locations of any pre-existing features and the strength of the rock, but also on the nature and strength of the contact between different lithologies.

5.4 Summary

Increasing the heterogeneity of the host rock in MOPEDZ on all scales shows that the evolution of fault zones is governed by many of the same factors as those for a homogeneous rock type namely:

- The ratio of σ_1 to σ_3.
- The initial relative positions of the joints, specifically, contractional vs. extensional geometries and overlapping vs. under-lapping joints.
- The orientation of the most compressive principal stress direction (σ_1) relative to the initial pair of joints.

whilst these significant factors remain key, host rock heterogeneity can also have a marked effect on the location and orientation of individual subsidiary linkage features that develop. Of particular importance are:

- The absolute value of the difference between material properties. This was illustrated when exploring the material properties of the sandstone in section 5.3. When the values of the Youngs modulus were towards the low end of the range of values provided the simulations result in all secondary faulting occurring within the sandstone. When this large difference in material properties was not present (i.e. the sandstone had stronger material properties) the faulting occurred at the granite/mafic boundary and was not connected to the main fault system.

The nature of the spatial variation in material properties, in particular different behaviour is predicted for smoothly varying properties (Section 5.1) and discrete changes (Sections 5.2 & 5.3). Increasing the heterogeneity *within* a single rock type by assuming a statistical variation in mineralogy, affects the detail of the fault zone which develops but not the general style of the overall fracture pattern (Section 5.1). Smoothly varying material properties may inhibit, enhance or deflect a propagating fault but it does not facilitate the growth of new faults independent of the pre-existing features. When different lithologies are introduced, the discrete change in material properties strongly influences secondary faulting which evolves (Section 5.3). As with smoothly varying properties, discrete changes may inhibit, enhance or deflect a propagating fault, often this effect is more pronounced (Section 5.2). In addition to this the geometry of the discrete change can create stress concentrations at locations removed from pre-existing or propagating fractures which allows new features to evolve. The influence of the geometry of the discrete change is best illustrated in Section 5.2 when discussing the aspect ratio of the fiammé.

6 Conclusions

This thesis extends on work carried out by *Willson* [2006] who developed a numerical model to simulate the temporal and spatial evolution of damage surrounding geological faults. The motivation for the research carried out by *Willson* [2006] was to ultimately improve flow simulation models, these models are of major interest to many industries including hydrocarbon, nuclear waste, sequestering of carbon dioxide, mining and in the exploitation of hydrothermal fluids and steam. One of the major uncertainties in these models is in predicting the permeability of faults, principally in the detailed structure of the fault zone. This motivation still holds for the research presented in this thesis where larger, more geologically complex simulations were conducted.

The model (MOPEDZ) simulates fault evolution from pre-existing structures; the research presented in this thesis has explored increasing the number and heterogeneity of those pre-existing structures (size, length, orientation) by estimating a starting geometry taken from a mapped field exposure. In addition to increasing the heterogeneity of the pre-existing structures the effect of increasing the heterogeneity of the host rock was also explored.

The introduction to this thesis posed two questions:

3) What are the major influences on the geometry of fault zones formed from the linkage of many pre-existing structures?
4) How is this geometry affected by host-rock heterogeneity?

Much of the research presented in this thesis was focussed on answering the first of these questions, and was presented in Chapter 4 and has been published in a peer review Journal [*Moir et. al.,* 2010]. This research investigated fault-zone evolution from more than 20 pre-existing joints in granite. The fault-zone evolution for maximum compressive far-field stress (σ_1) at a number of different orientations to the pre-existing joints was simulated. Key contributions to the literature are:

a) Local spatial and temporal variations in the stress field arise from interactions between neighbouring joints that have a significant effect on the predicted locations, orientations and timings of wing-crack development.

b) A clear difference in fault-zone geometry is predicted depending on the orientation of σ_1 with respect to the initial joint pattern: for σ_1 at an angle of 30° to the initial joints, co-planar joints progressively link up along strike to form long 'smooth' linear faults with few additional wing cracks; for an orientation of σ_1 of 60° to the initial joints, a more fractured complex 'stepped' fault-zone geometry evolves with multiple wing cracks forming linkage structures at a variety of angles. Existing field data show that both 'smooth' and 'stepped' fault-zone trace geometries are commonly observed in crystalline rocks

c) Local spatial and temporal stress perturbations affect predictions of zones of enhanced fracturing within fault networks at larger scales.

The effect of increasing the heterogeneity of the host rock was explored in Chapter 5 of this thesis. When the change in the material properties is smoothly varying it affects the detail of the fracture zone which develops by inhibiting, enhancing or deflecting propagating faults, but it does not affect the general style of the overall fracture pattern. When different lithologies are introduced, the discrete change in material properties has a stronger influence on the path of a propagating fault. In addition to influencing the evolution or inhibition of a propagating fault, the geometry of the contact between the different rock types, by creating local stress concentrations, may facilitate the evolution of new features.

The simulations presented in this thesis emphasise how essential it is to have good field data; data is required on the outcrop pattern, the likely locations of any pre-existing features, the strength of the rock and on the nature and strength of the contact between different lithologies.

The research presented in this thesis allows us to understand how different styles of fault zones can evolve from pre-existing features. The structure of these fault zones is influenced by the heterogeneity of the host rock particularly when there are discrete changes in the material properties. The geometry of the discrete changes in material properties is particulary important as it can facilitate the growth of new faults not connected to any pre-existing faults.

7 Future work

Although the research presented here has taken a significant step forward in being able to improve the predictions of the permeability of faults there are a number of limitations which need to be addressed before this final goal is achieved:

- The code is 2D and should be expanded to 3D to give a more realistic geological representation of the fracture pathways which may be created or blocked.
- The code can only simulate brittle rock types and if regional scale models are going to be addressed the deformation of more ductile rocks needs to be investigated.
- The third significant feature that needs to be examined is in modelling anisotropic rock types (e.g. metamorphic rocks such as slate and gneiss).

References

d'Alessio, M.A. and Martel, S.J., (2004). Fault terminations and barriers to fault growth, Journal of Structural Geology, 26(10) 1885-1896.

Al-Shayea, N.A., (2005). Crack propagation trajectories for rocks under mixed mode I-II fracture, Engineering Geology 81 84-97.

Amitrano, D., (2006), Rupture by damage accumulation in Rocks, International Journal of Fracture, (139) 369-381.

Aydin, A., (2000). Fractures, faults, and hydrocarbon entrapment, migration and flow, Marine and Petroleum Geology, (17) 797-814.

Benham, P.P., Crawford, R.J. and Armstrong, C.G. (1996). Mechanics of Engineering Materials 2nd edition, Longman Froup Ltd, Essex.

Bergbauer, S. and Martel, S.J., (1999). Formation of joints in cooling plutons, Journal of Structural Geology, 21(7) 821-835.

Bierlein, F.P., Murphy, F.C., Weinberg, R.F. and Lees, T., (2006). Distribution of orogenic gold deposits in relation to fault zones and gravity gradients: targeting tools applied to the Eastern Goldfields, Yilgarn Craton, Western Australia, Mineralium Deposita, 41(2) 107-126.

Billi, A., Salvini, F., and Storti, F., (2003). The damage zone-fault core transition in carbonate rocks: implications for fault growth, structure and permeability, Journal of Structural Geology, 25(11) 1779-1794.

Blenkinsop, T.G. (2008) Relationships between faults, extension fractures and veins, and stress, Journal of Structural Geology, 30 622-632.

Bobet, A., (2000). The initiation of secondary cracks in compression, Engineering Fracture Mechanics, 66 187-219

Bremaecker, D.J.C., Ferris, M.C., (2004). Numerical models of shear fracture propagation, Engineering Fracture Mechanics, 71 2161-2178.

Brister, B.S. and Ulmer-Scholle, D.S., (2004). Interpretation of depositional environments of upper Seven Rivers Formation from core and well logs, Grayburg Jackson Pool, Eddy County, New Mexico, Search and Discovery Article #20023 (http://www.searchanddiscovery.com/documents/2004/brister/index.htm).

Brogli, A., (2008). Fault zone architecture and permeability features in siliceous sedimentary rocks: Insights from the Rapolano geothermal area (North Apennines, Italy) Journal of Structural Geology, 30(2) 237-256.

Bruderer-Weng, C., Cowie, P., Bernabé, Y., Main, I., (2004). Relating flow channelling to tracer dispersion in heterogeneous networks. Advances in Water Resources 27 843–855

Bürgmann, R., Pollard, D.D., Martel S.J., (1994). Slip distributions on faults: effects of stress gradients, inelastic deformation, heterogeneous host-rock stiffness, and fault interaction. Journal of Structural Geology 16, 1675-1690.

Byerlee, J. D., 1967. Frictional characteristics of granite under high confining pressure. Journal of Geophysical Research 72, 3639-3648.

Caine, J.S., Evans, J. P. and Forster, C.B., (1996). Fault zone architecture and permeability structure, Geology, (24) 1025-1028.

Chambon, G., Schmittbuhl, J. Corfdir, A., Orellana, N., Diraison, M. and Géraud, Y. (2006). The thickness of faults: From laboratory experiments to field scale observations, Tectonophysics, (426) 77-94.

Chester, F.M., Evans, J.P., Biegel, R.L. (1993). Internal structure and weakening mechanisms of the San Andreas fault. Journal of Geophysical Research, 98(B1) 771–786.

Cowie, P.A. and Scholz, C.H. (1992), Physical explanation for the displacement-length relationship of faults using a post-yield fracture mechanics model, *Journal of Structural Geology*, 14(10) 1133-1148.

Craig, R.R. (1999). Mechanics of Materials, John Wiley & Sons, New York, 2nd Edition.

Crider, J.G. and Peacock, D.C.P., (2004). Initiation of brittle faults in the upper crust: a review of field observations, Journal of Structural Geology, 26(4) 691-707.

Cruikshank, K.M., Aydin, A., (1994). Role of fracture localization in arch formation at Arches National Park, Utah. Geological Society of America Bulletin, 106, 879-891.

Davatzes, N. C., Aydin, A. and Eichhubl, P., (2003). Overprinting faulting mechanisms during the development of multiple fault sets in sandstone, Chimney Rock fault array, Utah, USA, Tectonophysics, 363(1-2) 1-18.

Douglas, M., Clark, I.D., Raven, K., Bottomley, D., (2000). Groundwater mixing dynamics at a Canadian shield mine, Journal of Hydrology, (235) 88 – 103.

Du, Y., and Aydin, A., (1993). The Maximum Distortional Strain Energy Density Criterion for Shear Fracture Propagation With Applications to the Growth Paths of En Échelon Faults, Geophysical Research Letters, 20(11), 1091-1094.

Du, Y. J., and Aydin, A., (1995). Shear fracture patterns and connectivity at geometric complexities along strike-slip faults. Journal of Geophysical Research-Solid Earth,100(B9), 18093-18102.

Eshelby, J. D. (1957). The determination of the elastic field of an ellipsoidal inclusion, and related problems. Proceedings of the Royal Society, London, 241 376-396

Eshelby, J. D. (1959). The Elastic Field Outside an Ellipsoidal Inclusion. Proceedings of the Royal Society, London, 252 561-569.

Evans, J. P., Shipton, Z. K., Pachell, M. A., Lim, S. J., Robeson, K. R., (2000). The structure and composition of exhumed faults, and their implications for seismic processes. In: Bokelmann, G., Kovach, R.L. (Eds.) Proceedings of the 3rd Conference on Tectonic Problems of the San Andreas Fault System., Stanford University Publications, Geological Sciences 21, 67-81.

Evans, K. F., Genter, A., Sausse, J., (2005). Permeability creation and damage due to massive fluid injections into granite at 3.5km at Soultz: 1. Borehole observations. Journal of Geophysical Research, 110(B04203).

Faulkner D.R., Mitchel, T.M., Healy, D., Heap, M.J., (2006). Slip on 'weak' faults by the rotation of regional stress in the fracture damage zone, Nature, 31/10/06

Flodin, E. and Aydin. A., (2004). Faults with asymmetric damage zones in sandstone, Valley of Fire State Park, southern Nevada, Journal of Structural Geology, 26(5) 983-988.

Galli, G., Grimaldi, A., Leonardi, A., (2004). Three-dimensional modelling of tunnel excavation and lining. Computers and Geotechniques, 31(3) 171- 183.

Glazner, A. F., Bartley, J. M., Coleman, D.S., Gray, W., Taylor, R.Z., (2004). Are plutons assembled over millions of years by amalgamations of small magma chambers? GSA Today 14, 4/5

Golshani, A., Okui, Y., Oda, M., Takemura, T., (2006), A micromechanical model for brittle failure of rock and its relation to crack growth observed in triaxial compression tests of granite, Mechanics of Materials, 38 287 - 303

Granier, T., (1985). Origin, damping and pattern of development of faults in granite, Tectonics 4,721-737.

Granne, P., Vervoot, A., Wevers, M., (2007). Quantification of pre-peak brittle damage: Correlation between acoustic emission and observed micro-fracturing, International Journal of Rock Mechanics and Mining Science, 44 720-729.

Gudmundsson, A., (2004). Effects of Young's modulus on fault displacement. Comptes Rendus Geosciences, 336(1) 85-92.

Guo, J., McCaffrey, K., Jones R., Holdsworth, R., (2009). The spatial heterogeneity of structures in high porosity sandstones:Variations and granularity effects in orientation data Journal of Structural Geology 31 (2009) 628–636

Haimson, B. and Chang, C., (2000). A new true triaxial cell for testing mechanical properties of rock, and its use to determine rock strength and deformability of Westerly granite. International Journal of Rock Mechanics and Mining Sciences, 37 285-296.

Hamiel, Y., Katz, O., Lyakhovsky, V., Reches, Z., Fialko, Y., (2006). Stable and unstable damage evolution in rocks with implications to fracturing granite, International Journal of Geophysics, 167 1005-1016.

Healy, D., Jones, R.R., Holdsworth, R. E., (2006). New insights into development of brittle shear fractures from a 3-D numerical model of microcrack interaction, Earth and Planetary Science Letters, 249 14-28.

Heap, M.J. and Faulkner, D.R., (2008). Quantifying the evolution of static elastic properties as crystalline rock approaches failure, International Journal of Rock Mechanics and Mining Sciences, 45 564-573.

Jing, L., (2003). A review of techniques, advances and outstanding issues in numerical modelling for rock mechanics and rock engineering.

International Journal of Rock Mechanics & Mining Sciences, 40, 283-353.

de Joussineau, G. and Aydin, A., (2007). The evolution of the damage zone with fault growth in sandstone and its multiscale characteristics, Journal of Geophysical Research, 112 , B12401, doi:10.1029/2006JB004711.

de Joussineau, G., Mutlu, O., Aydin, A., Pollard, D.D., (2007). Characterization of strike-slip fault–splay relationships in sandstone. Journal of Structural Geology, 29(11) 1831-1842.

Kattenhorn, S.A., Aydin, A.A., Pollard, D.D., (2000). Joints at high angles to normal fault strike: an explanation using 3-D numerical models of fault-perturbed stress fields. Journal of structural Geology, 22, 1-23.

Kattenhorn. S. A., and Marshall, S. T., (2006). Fault-induced perturbed stress fields and associated tensile and compressive deformation at fault tips in the ice shell of Europa: implications for fault mechanics, Journal of Structural Geology, 28(12) 2204-2221.

Kim, Y. J., Peacock, D.C.P., Sanderson, D.J., (2004). Fault damage zones. Journal of Structural Geology, 26, 503-517.

Kim, Y.S. and Sanderson, D. J., (2005).The relationship between displacement and length of faults: a review, Earth-Science Reviews, 68 317-334.

Kirkpatrick, J. D., Shipton, Z. K., Evans, J. P., Micklethwaite, S., Lim, S. J., McKillop, P., (2008). Strike-slip fault terminations at seismogenic depths: The structure and kinematics of the Glacier Lakes fault, Sierra Nevada United States. Journal of Geophysical Research, B04304, doi: 10.1029/2007jb005311.

Li, L., Lee, P.K.K., Tsui, Y., Tham, L.G., Tang, C.A., (2003). Failure Process of Granite, International Journal of Geomechanics, 84 – 98.

Li, Y.P., Chen, L.Z., Wang, Y.H., (2005). Experimental research on pre-cracked marble under compression, International Journal of Solids and structures, 42 2505-2516.

Lim, S.J., (1998). Small strike slip faults in granitic rock:implications for three-dimensional models. Logan, Utah, Utah State University.

Lockner, D. A., Byerlee, J. D., Kuksenko, V., Ponomarev, A. & Sidorin, A., (1991). Quasi-static fault growth and shear fracture energy in granite, Nature, 350, 39 – 42.

Lunn, R. J., Willson, J. P. Shipton, Z. K., Moir, H., (2008). Simulating brittle fault growth from linkage of preexisting structures. Journal of Geophysical Research 113, B07403, doi:10.1029/2007JB005388.

Maerten, L., Gillespie, P., Pollard, D. D., (2002). Effects of local stress perturbation on secondary fault development, Journal of Structural Geology, 24, 145-153

Martel, S.J., (1990). Formation of compound strike-slip fault zones, Mount Abbot quadrangle, California, Journal of Structural Geology, 12(7) 869-877.

Martel, S.J., (1997). Effects of cohesive zones on small faults and implications for secondary fracturing and fault trace geometry. Journal of Structural Geology, 19, 835-847.

Martel, S.J., (1999). Mechanical controls on fault geometry, Journal of Structural Geology, (21) 585-596.

Martin, C. D., (1997). Seventeenth Canadian geotechnical colloquium: the effect of cohesion loss and stress path on brittle rock strength. Canadian Geotechnical Journal, 34, 698-725.

Mathews, J.H., Fink, K.D., (2004). Numerical Methods using Matlab, 4th Ed., Pearson Prentice Hall, New Jersey.

Micarelli, L., Moretti, I., Jaubert, M., Moulouel, H., (2006). Fracture analysis in the south-western Corinth rift(Greece) and implications on fault hydraulic behaviour, Tectonophysics, 426 31-59.

Micklethwaite, S. and Cox, S. F., (2004). Fault-segment rupture, aftershock-zone fluid flow and mineralization, Geology 32, 813-816.

Misra, S., Mandal, N., Dhar, R., Chakraborty, C., (2009). Mechanisms of deformation localization at the tips of shear fractures: Findings from analogue experiments and field evidence, Journal of Geophysical Research 114, B04204, doi:10.1029/2008JB005737.

Mitchell, T.M. and Faulkner, D.R. (2009). The nature and origin of off-fault damage surrounding strike-slip fault zones with a wide range of displacements: A field study from the Atacama fault system, northern Chile, Journal of Structural Geology 31, 802–816

Moir, H., Lunn, R.J., Shipton, Z.K., Kirkpatrick, J.D., (2010). Simulating Brittle Fault Evolution From Networks of Pre-existing Joints Within Crystalline Rock, Journal of Structural Geology, In Press, Accepted Manuscript.

Moon, V.G., (1993a). Microstructural controls on the geomechanical behaviour of ignimbrite, Engineering Geology, 35(1-2) 19-31.

Moon, V.G., (1993b). Geotechnical characteristics of ignimbrite: A soft pyroclastic rock type, Engineering Geology, Volume 35(1-2) 33-48.

Moore, D. E. and Lockner, D. A., (1995). The role of microcracking in shear-fracture propagation in granite. Journal of Structural Geology, 17(1) 95-111

Myers, R., and Aydin, A., (2004). The evolution of faults formed by shearing across joint zones in sandstone, Journal of Structural Geology, 26(5), 947-966.

Nixon, W.A., (1996). Wing crack models of the brittle compressive failure of ice. Cold Regions Science and Technology, 24(1) 41-55.

Orbert, L., Windes, S.L., Duvall, W.I. (1946). Standardized tests for determining the physical properties of mine rocks. U.S. Bureau of Mines, Rept Invest., 3891.

Pachell, M. A. and Evans, J. P. (2002). Growth, linkage, and termination processes of a 10-km-long strike-slip fault in jointed granite: the Gemini fault zone, Sierra Nevada, California, Journal of Structural Geology, 24(12) 1903-1924.

Pachell, M. A., Evans, J. P., Taylor, W. L., (2003). Kilometer-scale kinking of crystalline rocks in a transpressive convergent setting, Central sierra Nevada, California, GSA Bulletin, 115(7) 817-831.

Peacock, D.C.P. and Sanderson, D.J., (1995). Strike-slip relay ramps. Journal of Structural Geology, 17, 1351-1360.

Pennacchioni, G. and Mancktelow, N.S., (2007). Nucleation and initial growth of a shear zone network within compositionally and structurally heterogeneous granitoids under amphibolite facies conditions. Journal of Structural Geology, 29 1757 – 1780.

Pollard, D.D. and Segall, P., (1987). Theoretical displacements and stresses near fractures in rock: with applications to faults, joints, veins, dikes, and solution surfaces, In: B. Atkinson (eds) Fracture Mechanics of Rock, Academic Press London 277-349.

Reches, Z. & Lockner, D.A. (1994). Nucleation and Growth of Faults in Brittle Rocks. Journal of Geophysical Research-Solid Earth 99(B9): 18159-18173.

Renshaw C.E. and Pollard, D.D., (1994). Are large differential stresses required for straight fracture propagation paths?, Journal of Structural Geology, 16, 817-822

Scholz, C.H., (2002). The mechanics of earthquakes and faulting. Cambridge University Press.

Segall, P., Pollard, D. D., (1980). Mechanics of Discontinuous Faults. Journal of Geophysical Research 85, 4337-4350.

Segall, P. and Pollard, D. D., (1983). Nucleation and growth of strike slip faults in granite. Journal of Geophysical Research, 88, 555-568.

Shen, B., (1993). Mechanics of fractures and intervening bridges in hard rocks. Engineering Geology, Stockholm, Royal Institute of Technology.

Shen, B. and Stephansson, O., (1993). Numerical-analysis of mixed mode-I and mMode-II fracture propagation. International Journal of Rock Mechanics and Mining Sciences, 30, 861-867.

Shipton, Z.K. and Cowie, P.A., (2003). A conceptual model for the origin of fault damage zone structures in high porosity sandstone, Journal of Structural Geology, 25 333-344.

Singhal, B.B.S. & Gupta, R.P., (1999). Applied hydrogeology of fractured rocks. Kluwer Academic Publishers, Dordrecht.

Soden, A.M., (2008). The initiation and Evolution of ignibrite faults, Gran Canaria, Spain, PhD Thesis, University of Glasgow, Scotland.

Tang, C. (1997) Numerical simulation of progressive rock failure and associated seismicity, International Journal of Rock Mechanics and Mining Sciences, (34) 249-261.

Tang, C.A., Tham, L.G., Wang, S.H., Liu H. and Li, W.H., (2007). A numerical study of the influence of heterogeneity on the strength characterization of rock under uniaxial tension, Mechanics of Materials, 39(4) 326-339.

Timoshenko, S.P. & Goodier, J.N. (1970). Theory of Elasticity. McGraw-Hill Book Company, Auckland.

Turcotte, D. and Schubert, J., (2002). Geodynamics, 2nd Edition ed., Cambridge University Press, Cambridge.

Uehara, S. and Shimamoto, T., (2004). Gas permeability evolution of cataclasite and fault gouge in triaxial compression and implications for changes in fault-zone permeability structure through the earthquake cycle, Tectonophysics, (378) 183-195.

Vermilye, J.M. and Scholz, C.H., (1998). The process zone: A microstructural view of fault growth. Journal of Geophysical Research,103, 12223-12237.

Willemse, E.J.M., Peacock, D.C.P., Aydin, A., (1997). Nucleation and growth of strike-slip faults in limestones from Somerset, U.K., Journal of Structural Geology, 19(12) 1461-1477.

Walker, G.P.L. (1983). Ignimbrite types and ignimbrite problems, Journal of Volcanology and Geothermal Research, 17(1-4) 65-88.

Willson, J. P., (2006). Modelling the evolution of damage surrounding geological faults. PhD thesis, Heriot-Watt University, Edinburgh.

Willson, J. P., Lunn, R. J., Shipton, Z. K., (2007). Simulating spatial and temporal evolution of multiple wing cracks around faults in crystalline basement rocks. Journal of Geophysical Research-Solid Earth 113, B07403, doi:10.1029/2007JB005388.

Xu, X.H., Ma, S.P., Xia, M.F., Ke, F.J., Bai, Y.L., (2005). Synchronous multi-scale observations on rock damage and rupture. Theoretical and Applied Fracture Mechanics, 44(2) 146-156

Yang, S.Q., Jiang, Y.Z., Xu, W.Y., Chen, X.Q., (2008). Experimental investigation on strength and failure behaviour of pre-cracked marble under conventional triaxial compression, International Journal of Solids and Structures, 45 2796-4819.

Appendix A

Video files held on CD-ROM

Contents of Appendix A include

Disk	File name	Description	Relevant Figure in Thesis
1	2518_full	Video of damage plot illustrating the spatial and temporal evolution of the linking fractures predicted by MOPEDZ . The joints are oriented at approximately 60° to σ_1.	Figure 4.4
1	2498_full	Video of damage plot illustrating the spatial and temporal evolution of the linking fractures predicted by MOPEDZ . The joints are oriented at approximately 30° to σ_1.	Figure 4.14
1	Run2720	Video of damage plot illustrating the spatial and temporal evolution of the linking fractures predicted by MOPEDZ when the host rock has a smoothly varying heterogeneity. The joints are oriented at approximately 60° to σ_1.	Figure 5.7
1	Run2725	Video of damage plot illustrating the spatial and temporal evolution of the linking fractures predicted by MOPEDZ when the host rock has a smoothly varying heterogeneity. The joints are oriented at approximately 30° to σ_1.	Figure 5.9
2	Strain_1_300	Similar simulation to that shown in 2518_full. This plot shows the evolution of strain in the simulation. First 300 frames	N/A
2	Strain_301_600	... the simulation continues	N/A